The Pennsylvania State University

The Graduate School

Department of Engineering Science and Mechanics

GUIDED WAVE PROPAGATION AND FOCUSING IN VISCOELASTIC MULTILAYERED HOLLOW CYLINDERS

A Dissertation in

Engineering Science and Mechanics

by

Jing Mu

Submitted in Partial Fulfillment
of the Requirements
for the Degree of

Doctor of Philosophy

August 2008

The dissertation of Jing Mu was reviewed and approved* by the following:

Joseph L. Rose
Paul Morrow Professor of Engineering Science and Mechanics
Dissertation Advisor
Chair of Committee

Bernhard R. Tittmann
Schell Professor of Engineering Science and Mechanics

Clifford J. Lissenden
Associate Professor of Engineering Science and Mechanics

Virendra M. Puri
Distinguished Professor of Agricultural and Biological Engineering

Samia A. Suliman
Assistant Professor of Engineering Science and Mechanics
Special Member

Judith A. Todd
Professor of Engineering Science and Mechanics
P. B. Breneman Department Head Chair
Head of the Department of Engineering Science and Mechanics

*Signatures are on file in the Graduate School

ABSTRACT

The understanding of guided wave propagation characteristics, source influence, and mode control in hollow cylindrical structures is crucial for guided wave nondestructive evaluation of pipelines. This thesis reviews the previous guided wave theories on single elastic hollow cylinders and develops their application in pipe imaging and defect circumferential sizing. Motivated by the fact that most pipelines are coated with viscoelastic materials, the thesis establishes a systematic procedure targeting on solving the problem of guided wave propagation, source influence, as well as focusing in multilayered hollow cylindrical structures containing viscoelastic materials.

A suitable Semi-Analytical Finite Element (SAFE) formulation is first developed to solve the dispersion curves (including axisymmetric and non-axisymmetric guided wave modes) and wave structures in viscoelastic multilayered hollow cylinders. Stress distributions across pipe thickness and the cross sectional deformations for different guided wave modes are illustrated to help interpret modal behavior.

A general orthogonality relation applicable for both single-layered and multilayered, elastic and viscoelastic hollow cylindrical structures is then derived. This orthogonality relation is subsequently implemented to sort guided wave modes obtained from the SAFE calculation. Numerical results show that all the guided wave modes are successfully sorted. The mode sorting enables us to trace the modal behavior evolving with frequency for any guided wave mode. It also provides the basis for solving source influence in viscoelastic multilayered hollow cylinders.

The guided wave field generated by a specific source loading on a viscoelastic multilayered hollow cylinder is tackled by the employment of the Normal Mode Expansion (NME) technique. Different from the source influence in an elastic single-layered hollow cylinder, the displacement and stress continuity condition must be incorporated in deriving the amplitude factors of the generated normal modes. The displacement angular profiles of a certain loading are consequently obtained by the superposition of all the excited modes with appropriate amplitudes. After the angular profiles are obtained, the focusing deconvolution algorithm is incorporated to provide the amplitude factors and time delays for guided wave phased array focusing in viscoelastic multilayered hollow cylinders.

To visualize the focusing in a viscoelastic multilayered hollow cylinder, a viscoelastic coated pipe is taken as an example to build in ABAQUS. Finite Element Modeling (FEM) of guided wave focusing in the coated pipe is conducted. The FEM results agree well (5% difference in focal amplitudes) with the theoretical calculations.

Finally, guided wave synthetic focusing experiments are designed to verify the theories. The guided wave synthetic focusing methodology and experiment procedure are introduced in detail. Data are taken on a steel pipe coated with 0.4-mm bitumastic 50. Four channel guided wave synthetic focusing is performed in post processing. Both the theoretical predictions and the experimental results show that the focal amplitudes under such a relatively thin coating are of less than 10% difference for the bare pipe focusing parameters and the coated pipe focusing parameters at the designed focal location.

TABLE OF CONTENTS

LIST OF FIGURES

LIST OF TABLES

ACKNOWLEDGEMENTS

I would like to express my sincere gratitude to my Ph.D. advisor, Dr. Joseph L. Rose. The thesis could not have been accomplished without his guidance and support. I would also like to thank my committee members for their kind help and suggestions to make the thesis better. Thanks are given to Dr. Mike J. Avioli and Dr. Li Zhang of FBS. Inc. for the valuable experience they have shared with me. I also appreciate the generous help provided by my colleague Jia Hua during the thesis work. Finally, I would like to dedicate this thesis to my husband, Fei Yan, who has also been my colleague for more than ten years. My appreciation to him is beyond what I can express.

Chapter 1

Introduction

1.1 Problem Statement

Millions of miles of pipes are used in the US for the transportation of gas, chemicals, and other products. Most of these pipes and pressure vessels have been used for a very long time and are encountering the problem of aging. The steam pipe explosion on July 18, 2007 in Jolts Midtown resulted in one person's death and more than 30 hurt. Total replacement of these pipes and pressure vessels are too expensive. Therefore, regular inspection and monitoring using Non-Destructive Evaluation (NDE) methods are needed to guarantee the integrity and safety of these pipelines.

Bulk waves are commonly used in conventional ultrasonic NDE because they are easy to implement. Other methods such as X-ray [Ong 1994], eddy current [Sun 1992], and magnetic flux [Plotnikov 2002] are also used in NDE. The disadvantage of using these methods is that inspections are usually done on a point-by-point basis, which takes a long time to finish an inspection of the entire structure.

The pig method [Cordell 1994] [Williamson 1994] is a fast, long distance pipe inspection technique utilizing ultrasonic bulk waves. The equipment needs to move inside the pipe in order to test it. This technique is expensive. Moreover, once the equipment gets stuck inside the pipe, it is fairly costly to cut the pipe and to remove the equipment. Also, this technique is not suitable for smaller pipes, pipes carrying chemicals, and those

having complex structures, such as elbows. The so called “unpiggable lines” represents forty percent of the pipelines that should be inspected.

Guided waves are ultrasonic waves traveling in bounded waveguides, such as plates, rods, and pipes. Compared to bulk waves, guided waves propagate long distances and have the potential to go beyond complicated structures, for example, elbows. Therefore, it is excellent for long-range nondestructive evaluation (NDE). The utilization of guided waves in NDE and structural health monitoring (SHM) makes it possible to inspect the entire structure from a single probe position without the removal of soil or insulation. Due to these advantages, guided wave techniques can provide us with a faster and more economical way for structure inspections and defect screening.

In applications, most pipelines are covered by various viscoelastic coatings for protection purposes. The existence of coatings alters the boundary conditions and the wave propagation characteristics in pipes. As a result, previous theories on bare elastic pipes [Gazis 1959; Ditri et al. 1992] may not be valid in viscoelastic coated pipes. This makes guided wave mode control and mode selection difficult in coated pipe testings. Therefore, the understanding of coating influence and the full exploration of guided wave modes in viscoelastic multilayered structures is crucial for providing the guidance for pipeline maintenance.

1.2 Literature Review

1.2.1 Guided wave propagation theories

Guided wave theories have been studied extensively for decades. As early as the beginning of last century, [Rayleigh 1945] described the free waves traveling on the surface of a semi-infinite solid. [Stoneley 1924] studied free waves that occur at an interface between two media. [Lamb 1917] investigated the wave propagation in an elastic isotropic plate with traction free boundary conditions. [Viktorov 1970] also gave a remarkable contribution to the understanding of guided waves in plates.

Wave propagation in multiple layers was first studied in [Thomson 1950]. In this study, a transfer matrix was introduced to describe the displacements and stresses at the bottom of a layer with respect to those at the top of the layer. In this way, the displacements and stresses at the bottom of a multi-layered system could be related to those at the top of the system through interface conditions. Then, the transfer matrix of the system could be solved by applying appropriate boundary conditions of the system. A problem of the transfer matrix approach was that the matrix became ill-conditioned at high frequencies and therefore, solutions are difficult to obtain.

The global matrix method was developed by [Knopoff 1964]. Knopoff provided an alternative way to tackle wave propagation problems. In his method, the determinant of a global matrix must equal zero by satisfying all of the interface and boundary conditions, which therefore became the characteristic equation of an eigenvalue problem. The roots of the characteristic equation were the eigenvalues of the system, which gave

the modes that could exist in the system. The eigenvectors of the system associate with the wave structures of the modes.

The problem of ultrasonic wave propagation through a hollow cylinder can also be solved using the above techniques. Ghosh got the first mathematical solution for the longitudinal, axisymmetric wave modes in a rod with co-axial annulus [Ghosh 1923]. Gazis [Gazis 1959] obtained the first complete solution to harmonic guided wave modes propagating in an infinite hollow cylinder. His solution treated both longitudinal and torsional axisymmetric wave modes as well as non-axisymmetric wave modes. Based on Gazis' work, Ditri and Rose [Ditri et al., 1992] showed that the double infinite number of wave modes in the infinite hollow cylinder were all normal modes, whose orthogonality relation could be derived from the complex reciprocity relation [Auld 1990]. Subsequently, a Normal Mode Expansion (NME) technique was used to determine the amplitude of each normal mode generated by the source loading on an infinite hollow cylinder. Li and Rose [2001] did numerical computations for the wave propagation of the partial loading case according to the analytical results given by Gazis and Ditri. They found that the non-axisymmetric circumferential energy distribution varied as a function of the axial distance and they verified the energy distribution by experiments.

1.2.2 Phased array focusing techniques

Althoug the phased array focusing technique has been widely used in such fields as electromagnetic waves, for example, radar and conventional ultrasonic bulk waves, it was rarely seen in guided wave applications due to the complexity of guided waves. In

2002, Li and Rose reported that if the angular profile for a single channel loading is known, the total guided wave angular profile can be controlled and thus focused at any predetermined circumferential location by a circumferentially placed phased array with appropriate voltage amplitude and time-delay inputs. With the guided wave phased-array focusing technique in pipes, a strong and narrow focused beam could be achieved. It was proven to provide better circumferential resolution and higher penetration power than axisymmetric waves in defect detection. As a result, the circumferential location of a defect can be determined. It also provided better potential in defect sizing. Sun et al. [2003] extended the guided wave phased-array focusing technique further by utilizing torsional waves.

Another focusing technique that is receiving more and more attention is the time-reversal focusing technique [Ing et al., 1998]. This technique reverses the received signals in time domain and utilizes these time-reversed signals as transmitting signals to focus at the largest reflector. The advantage of this technique is that there is no computation complexity. Only hardware with an arbitrary function generator is needed. Another advantage is that this technique is applicable in various media, such as inhomogenous material, for example, human body, and complex wave guide structures, for instance, pipe elbows.

The above focusing techniques are usually referred to as real time focusing, where the wave energy is actually tuned to focus at a predetermined location by sending signals from the phased-array transducers with different amplitude factors and time delays. In applications, the hardware that is capable of accurately controlling time delays are often expensive. In addition, a phased array with a large number of channels or transducers can

be costly too. These are the cases where synthetic focusing techniques are employed instead of real time focusing. In synthetic focusing, signals are sent and received by different transducer pairs and the focal waveforms are obtained by signal processing in post processing procedure. Several ways of achieving synthetic focusing in bulk waves are commonly used: the Common Source Method (CSM), the Synthetic Aperture Focusing Technique (SAFT), and the Total Focusing Method (TFM). A brief review can be found in [Davies et al., 2005]. Synthetic focusing is also used in guided waves. Some excellent work can be found in [Wilcox 2003], [Giurgiutiu et al., 2004] and [Hayashi et al., 2005]. Different from the synthetic focusing using bulk waves, dispersion associated with multiple mode propagation has to be taken into account in guided wave synthetic focusing. Compared to real-time focusing, synthetic focusing may offer less penetration power because of the existence of noise, but it is more cost effective in some cases.

1.2.3 Numerical methods used in wave propagation analysis

With the development of modern computers that are capable of handling enormous computational tasks, numerical methods become more and more prevalent in solving problems dealing with complex structures. Especially, for the problems associated with wave propagation, reflection and scattering in wave guides with complex geometries, such as elbows and bare or multilayered pipes, analytical solutions are often difficult to find. Therefore, various numerical methods have been developed to provide information on wave propagation characteristics in these complicated situations. Numerical methods that are commonly used in solving problems related to guided waves

include Boundary Element Method (BEM), Finite Difference Method (FDM), Finite Element Method (FEM), and Semi-Analytical FEM (SAFEM).

BEM simplifies volume integrals to surface integrals by applying Green's function. Thus, a 3-dimensional problem is reduced to a 2-dimentional problem. However, BEM is not as flexible as FEM in that the surface integrals are intricate and have to be derived according to a particular geometry for a problem. In addition, solving the surface integrals do not necessarily save much time in a 3-dimensional problem with complex geometries compared to FEM. Some studies of wave propagation using BEM can be found in [Achenbach 1992] and [Cho 1996].

FDM is a simple and efficient method for solving ordinary differential equations (ODEs) in simple geometries. The differential equations are simplified to finite difference equations by discretizing the region. FDM is easy to be implemented in numerical calculations but a disadvantage of FDM is that it requires the velocity distribution at boundaries.

In FEM, a structure is divided into a finite number of elements with finite size and boundaries. Elements satisfy the same governing equation and their own boundary conditions. The FEM is a good choice for solving partial differential equations over complex domains (like bridges and pipelines) or when the desired precision varies over the entire domain. Both implicit and explicit time integration analyses can be used to obtain the nodal displacements in FEM. Explicit analysis obtains a kinematical state by direct calculation from a previous state, while implicit analysis employs iteration to get a convergent solution for each state. Explicit analysis is a simple and clear choice for linear

wave propagation problems, whereas implicit analysis may be more suitable for nonlinear problems.

FEM modeling of wave propagation problems have been widely investigated by many researchers, [Koshiba 1987], [Moser 1999], [Demma 2003], [Luo 2005], and [Li 2005]. In order to guarantee convergent solutions in time domain and adequately accurate solutions in spatial domain during wave propagation simulations, two important criteria must be pointed out

1) The maximum length of each element $\Delta L_{\max}$ should be smaller than a tenth of the smallest wave length, i.e. $\Delta L_{\max} \le \frac{\lambda_{\min}}{10}$.

2) The time step Δt has to be selected according to $\Delta t < \frac{\Delta L_{\min}}{C_{\max}}$, where $\Delta L_{\min}$ is the smallest element length and $C_{\max}$ is the fastest wave velocity that exists in the problem.

The Semi-Analytical Finite Element (SAFE) method is a technique that combines analytical and finite element methods in solving problems. In the SAFE method, the wave guides are discretized in their cross sections, but analytical solutions are employed in the wave propagation direction. In this way, harmonic waves can be easily represented in the analytical solution, while complex cross section geometries can be meshed into finite elements. This technique has the advantage of handling wave guides with complex geometries as FEM does. In the mean time, it also reduces the dimensions in finite element computation by incorporating analytical solutions in one or more dimensions. Therefore, compared to FEM, less computation time and space are needed for SAFEM.

In some literature, the SAFE method is also referred to as the Strip Element method (SEM) [Cheung 1976]. In recent years, SAFE has been widely adopted in solving wave propagation problems in waveguides with complex cross sections, for instance, rail [Hayashi 2003] and laminates with complex material properties [Shorter 2004]. The criteria in SAFE discretization are the same as those used in FEM. Due to these benefits, the SAFE method is adopted in this thesis to tackle the wave propagation problem in viscoelastic multilayered hollow cylindrical structures. The SAFE method will be discussed further in Chapter 5.

1.2.4 Guided wave propagation in multilayered cylindrical structures

Some researchers have studied plate or plate-like structures with viscoelastic properties, for example, [Simonetti 2004] and [Predoi et al., 2007]. These plate solutions may be safely used to approximate hollow cylinders with thickness to radius ratio less than 10% [Luo, et al., 2005]. Beard and Lowe [2003] used guided waves to inspect the integrity of rock bolts. They provided the dispersion curve of rock bolts with aixsymmetric modes and 3 lower order (circumferential order equals 1) flexural modes in their study at a relatively low frequency range. Ma, et al. [2006] investigated the fundamental torsional mode scattering from an axisymmetric sludge layer inside a pipe. In his study, the sludge layer is considered to be an elastic epoxy layer. Elvira-Segura [2000] investigated the axisymmetric mode propagation in a cylindrical elastic tube filled with viscous liquid. Pavlakovic et al. [2001] analyzed the axisymmetric longitudinal modes in embedded bars and experimentally verified the theories. The axisymmetric

guided wave mode solutions in viscoelastic coated pipes have been obtained by Barshinger and Rose [2004] using the analytical global matrix method. However, due to the fact that the matrix is ill-conditioned and gets bigger for solving non-axisymmetric modes, the root searching becomes more computationally costly and the non-axisymmetric mode solutions remain unexplored.

1.3 Objectives

Based on the pipe inspection problem statement and literature review, guided waves modes have been well investigated and successfully focused in bare elastic pipes. Nevertheless, many critical subjects still remain largely unexplored, such as guided wave pipe imaging and defect sizing capabilities, guided wave propagation characteristics and focusing possibility in pipes with viscoelastic coatings. The objectives of the thesis are to solve guided wave propagation and to achieve guided wave focusing in viscoelastic multilayered hollow cylinders. To realize these objectives, the following major tasks are taken:

1. To investigate the long range guided wave imaging potential in pipe inspections based on the guided wave focusing technique in elastic bare pipes.
2. To overcome the difficulty in guided wave computation and testing caused by the existence of viscoelastic coatings, SAFEM can be adopted to analyze the non-axisymmetric mode propagation characteristics including dispersion curves and wave structures in viscoelastic multilayered hollow cylinders.

3. To accomplish guided wave mode control, the dispersion curves should be sorted. This enables us to trace the modal behavior of a specific guided wave mode with frequency.
4. To develop a suitable orthogonality relation applicable for viscoelastic multilayered hollow cylinders is necessary for further analysis of source influence in viscoelastic multilayered hollow cylinders.
5. To analyze the source influence in viscoelastic multilayered hollow cylinders on the basis of Normal Mode Expansion (NME). However, the interfacial conditions between different layers have to be taken care of.
6. Based on source influence analysis, a focusing algorithm, as those used for the bare pipes, can be implemented to obtain the time delays and amplitude factors customized for a viscoelastic coated pipe.
7. To carry out finite element modeling in Abaqus to visualize the focusing effect in viscoelastic multilayered hollow cylinders and confirm the theories.
8. To design experiments to focus guided waves in coated pipe and validate the theoretical derivations and numerical computations.

Chapter 2

Guided Wave Propagation in Bare Pipes

2.1 Dispersion Curves

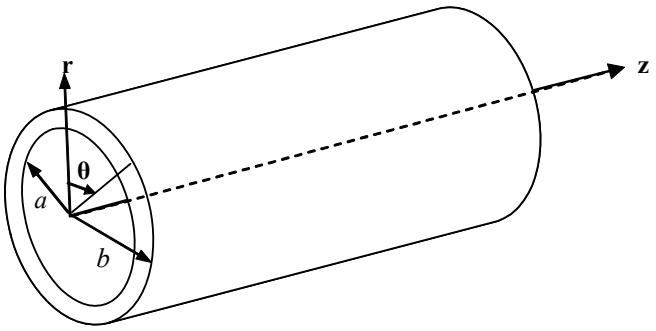

Figure 2-1: Cylindrical coordinates

The guided waves that can propagate in a free elastic single-layered hollow cylinder are represented by the dispersion curves for such a structure. The dispersion curves can be obtained by solving the governing equations together with the boundary conditions. The governing equations of motion in an isotropic, homogeneous, elastic solid are the Navier governing equations [Kolsky 1963, Pollard 1977, Gazis 1959].

$$\mu\nabla^2\mathbf{u} + (\lambda + \mu)\nabla\nabla\cdot\mathbf{u} = \rho\left(\partial^2\mathbf{u}/\partial t^2\right) \qquad 2.1$$

where $\mathbf{u}$ is the displacement vector, ρ represents the density, t is the time, μ and λ are Lamé constants, and ∇^2 is the three-dimensional Laplace operator.

The basic computational process for dispersion curves can be found in [Rose 1999]. A conventional way of presenting the solutions in vector form is to use the

Helmholtz method [Malvern 1969], in which longitudinal waves are described by a scalar potential function ϕ and shear waves by a vector potential function **H** whose direction is normal to both the direction of wave propagation and the direction of particle motion:

$$\mathbf{u} = \nabla\phi + \nabla \times \mathbf{H}. \tag{2.2}$$

An additional constraint is added by satisfying the gauge invariance

$$\nabla \cdot \mathbf{H} = 0 \tag{2.3}$$

Substituting Eq. 2.2 into Eq. 2.1 yields

$$v_1^2 \nabla^2 \phi = \partial^2 \phi / \partial^2 t \tag{2.4}$$

and

$$v_2^2 \nabla^2 \mathbf{H} = \partial^2 \mathbf{H} / \partial^2 t, \tag{2.5}$$

where v_1 is the longitudinal wave velocity and v_2 is the transverse wave velocity in the medium.

By applying the method of separation of variables in cylindrical coordinates (Figure 2-1), the solutions to the above two equations can be assumed as

$$\begin{aligned} \phi &= f(r)\cos n\theta \exp[i(kz - wt)], \\ H_r &= g_r(r)\sin n\theta \exp[i(kz - wt)], \\ H_\theta &= g_\theta(r)\cos n\theta \exp[i(kz - wt)], \\ H_z &= g_3(r)\sin n\theta \exp[i(kz - wt)]. \end{aligned} \tag{2.6}$$

where k denotes the wave number and n is the circumferential order of the wave mode. $f(r)$ and $g_\xi(r)$ (ξ = r, θ, 3) are unknown functions with respect to r. Substituting Eq. 2.6 into Eq. 2.4 and Eq. 2.5, the unknown function in Eq. 2.6 can be solved. They have the following forms

$$\begin{aligned} f &= AZ_n(\alpha_1 r) + BW_n(\alpha_1 r), \\ g_3 &= A_3 Z_n(\beta_1 r) + B_3 W_n(\beta_1 r), \\ 2g_1 &= g_r - g_\theta = 2A_1 Z_{n+1}(\beta_1 r) + 2B_1 W_{n+1}(\beta_1 r), \\ 2g_2 &= g_r + g_\theta = 2A_2 Z_{n-1}(\beta_1 r) + 2B_2 W_{n-1}(\beta_1 r). \end{aligned} \qquad 2.7$$

Where $\alpha_1 r = |\alpha r|$, $\beta_1 r = |\beta r|$, $\alpha^2 = \frac{\omega^2}{v_1^2} - k^2$, $\beta^2 = \frac{\omega^2}{v_2^2} - k^2$, A, B, A_1, B_1, A_2, B_2, A_3, and B_3 are unknown coefficients, Z denotes a Bessel function J or modified Bessel function I function, and W denotes a Bessel function Y or modified Bessel function K function, according to Table 2-1 .

Table 2-1: Parameters and functions.

Interval	Functions used
$\frac{\omega}{v_1} > k$ i.e. $v > v_1$, $\alpha^2 > 0, \beta^2 > 0$	$J(\alpha r), Y(\alpha r), J(\beta r), Y(\beta r)$
$\frac{\omega}{v_2} > k > \frac{\omega}{v_1}$ i.e. $v_1 > v > v_2, \alpha^2 < 0, \beta^2 > 0$	$I(\alpha_1 r), K(\alpha_1 r), J(\beta r), Y(\beta r)$
$k > \frac{\omega}{v_2}$ i.e. $v_2 > v, \alpha^2 < 0, \beta^2 < 0$	$I(\alpha_1 r), K(\alpha_1 r), I(\beta_1 r), K(\beta_1 r)$

Substituting the general solution Eq. 2.7 back into Eq. 2.2, one obtains the displacement expression in terms of Z and W

$$
\begin{aligned}
u_r &= [f' + \frac{n}{r} g_3 - ikg_\theta] \cos n\theta \exp[i(kz - \omega t)], \\
u_\theta &= [-\frac{n}{r} f + ikg_r - g_3'] \sin n\theta \exp[i(kz - \omega t)], \\
u_z &= [ikf + \frac{1}{r} g_\theta + g_\theta' - \frac{n}{r} g_r] \cos n\theta \exp[i(kz - \omega t)].
\end{aligned} \tag{2.8}
$$

From the strain-displacement relations and the constitutive equations, the stress field can be obtained

$$
\begin{aligned}
\sigma_{rr} &= \{-\lambda(\alpha^2 + k^2) f + 2\mu[f'' - \frac{n}{r^2} g_3 + \frac{n}{r} g_3' - ikg_\theta']\} \cos n\theta \exp[i(kz - \omega t)], \\
\sigma_{rz} &= \mu\{ik\frac{n}{r} g_3(r) + i2kf' + (k^2 - \frac{1}{r^2}) g_\theta \\
&+ \frac{1}{r} g_\theta' + g_\theta'' + \frac{n}{r^2} g_r - \frac{n}{r} g_r'\} \cos n\theta \exp[i(kz - \omega t)], \\
\sigma_{r\theta} &= \mu\{-\frac{1}{r}[ikg_r - g_3'] + [\frac{2n}{r^2} f - \frac{2n}{r} f' + ikg_r' - g_3'']] \\
&- \frac{n}{r}[\frac{n}{r} g_3(r) - ikg_\theta(r)]\} \sin n\theta \exp[i(kz - \omega t)]
\end{aligned} \tag{2.9}
$$

The traction free boundary conditions for a hollow cylinder can be expressed as $\sigma_{rr} = \sigma_{rz} = \sigma_{r\theta} = 0$ at inner surface $r = a$ and outer surface $r = b$. Thus, the Navier governing equations with unknown wave number k (or frequency ω and phase velocity c) and the homogeneous boundary conditions as well as the gauge invariance form an eigenvalue problem [Gazis 1959]. The boundary conditions and gauge invariance can be written in the following matrix form:

$$
\begin{bmatrix}
C_{11} & C_{12} & \cdots & C_{18} \\
C_{21} & C_{22} & \cdots & C_{28} \\
\vdots & \vdots & \ddots & \vdots \\
C_{81} & C_{82} & \cdots & C_{88}
\end{bmatrix}
\begin{bmatrix}
A \\ B \\ \vdots \\ B_3
\end{bmatrix}
=
\begin{bmatrix}
0 \\ 0 \\ \vdots \\ 0
\end{bmatrix}. \tag{2.10}
$$

In order to get a non-trivial solution of this problem, the determinant of the matrix [C] must equal to zero, which gives the characteristic equation of the eigenvalue problem.

$$\left|C(\omega,c)\right|_{8\times 8} = 0 \qquad 2.11$$

The roots of the characteristic equation are the eigenvalues, which give the possible wave modes (shown as dispersion curves) that exist in an infinite hollow cylinder.

The process of the derivation of the dispersion curves is summarized in Figure 2-2. As an illustrative example, the phase velocity dispersion curves for a 16 in. schedule 30 pipe for both longitudinal and torsional wave groups are shown in Figures 2-3 to 2-4. The corresponding group velocity dispersion curves are shown in Figures 2-5 and 2-6.

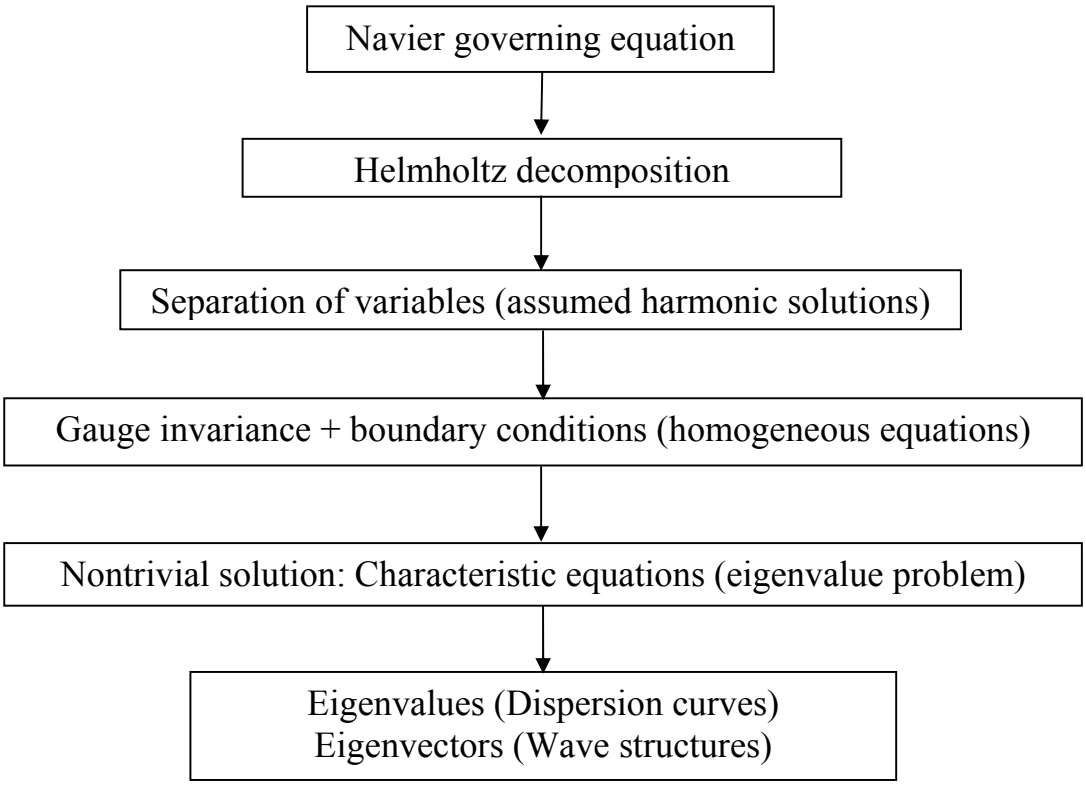

Figure 2-2: The derivation of dispersion curves and wave structures.

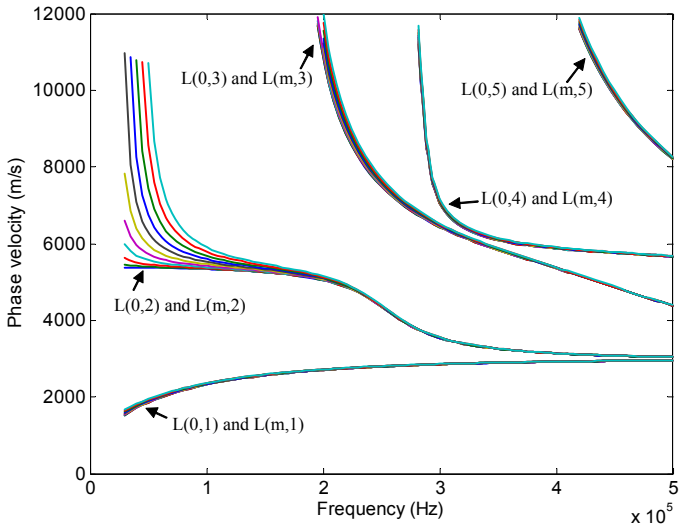

Figure 2-3: The phase velocity dispersion curve of longitudinal groups in a 16 in. schedule 30 steel pipe including axisymmetric modes L(0,n) and flexural modes L(m,n) (m=1,2,3,…).

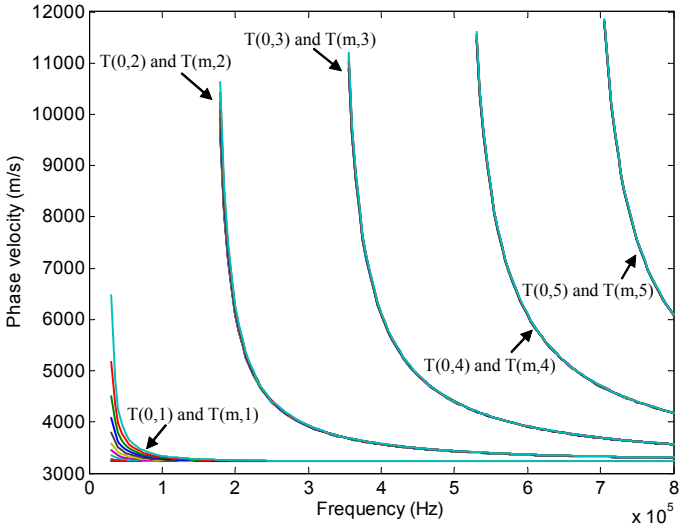

Figure 2-4: The phase velocity dispersion curve of torsional groups in a 16 in. schedule 30 steel pipe including axisymmetric modes T(0,n) and flexural modes T(m,n) (m=1,2,3,…).

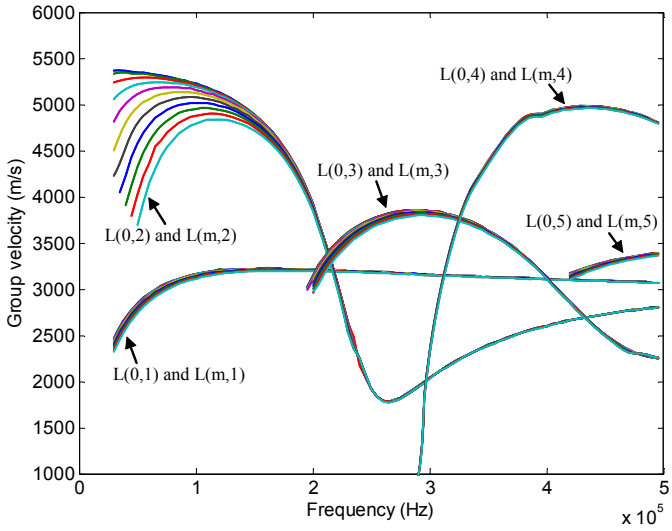

Figure 2-5: The group velocity dispersion curve of longitudinal groups in a 16 in. schedule 30 steel pipe including axisymmetric modes L(0,n) and flexural modes L(m,n) (m=1,2,3,…).

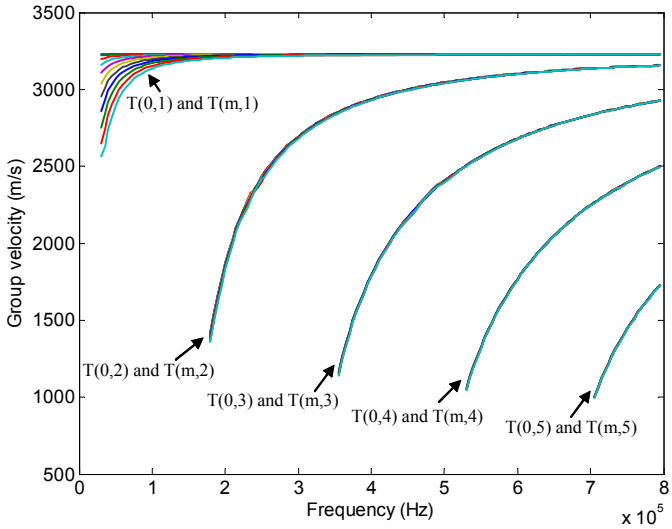

Figure 2-6: The group velocity dispersion curve of torsional groups in a 16 in. schedule 30 steel pipe including axisymmetric modes T(0,n) and flexural modes T(m,n) (m=1,2,3,…).

2.2 Wave Structures

As can be seen from the dispersion curves shown above, guided wave modes are much more complicated than bulk wave modes. There are an infinite number of mode groups in either the longitudinal or torsional type of guided wave modes. There are also an infinite number of modes in each mode group. They form the so called doubly infinite number of guided wave modes in a pipe [Ditri, et al., 1992] and they can be classified into different categories according to different criteria as shown in Figure 2-7.

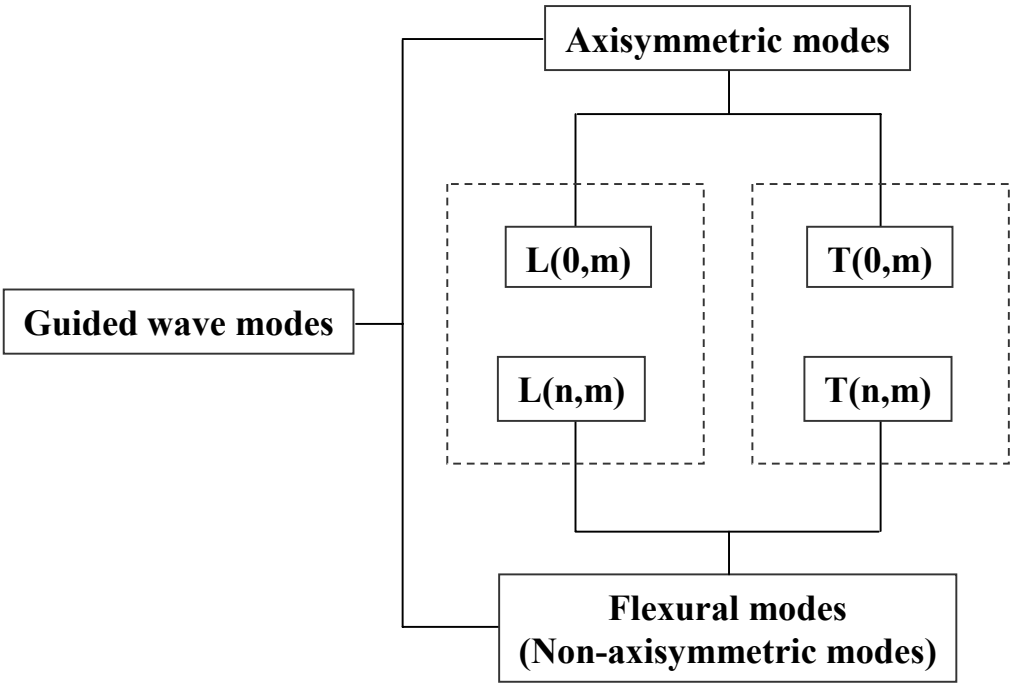

Figure 2-7: Guided wave mode category in a pipe [Sun et al., 2005]

Guided wave modes in a cylindrical wave guide can be represented by two indices, for example T(n,m) or L(n,m), where $n \in \{0,1,2,\cdots\}$ is the index of circumferential order, $m \in \{1,2,\cdots\}$ is the m^{th} root of the characteristic equation of circumferential order m for torsional type (denoted by T) and longitudinal type (denoted by L) of mode respectively.

Conventionally, modes with the same circumferential order n are often called a mode group or a mode family. In this thesis, a mode group or family refers to longitudinal or torsional type of modes of the same m but with different circumferential orders. The reason to do this lies in the fact that an L or T type of modes with the same m but different circumferential orders bear similar modal characteristics, such as phase velocities, attenuation and wave structures.

According to symmetry, these guided wave modes can be separated into axisymmetric (n=0) and flexural modes ($n \neq 0$). Based on the characteristics of wave structure, they are classified into longitudinal type of modes, which have dominant displacement in radial and axial directions, and torsional type of modes, whose dominant displacement is in circumferential direction.

In order to understand the behavior of guided wave modes, it is quite indispensable to study the wave structures. Some sample wave structures are shown in Figure 2-8 to Figure 2-11. Figure 2-8 and Figure 2-9 illustrate the wave structures in the second longitudinal mode group L(n,2) with circumferential order n varying from 0 to 10 at a frequency of 50 kHz in a 16 *in*. schedule 30 steel pipe. As can be seen in Figure 2-8**,** the axisymmetric mode L(0,2) has no displacement in circumferential direction. L(0,2) has almost uniform displacement distribution in axial direction and nearly antisymmetric displacement distribution in thickness direction. Such a displacement distribution characteristic is very similar that of the S0 mode in an elastic, homogeneous plate. The flexural modes L(n,2) where $n \neq 0$ share similar characteristics for the displacement distributions in the thickness and axial directions as L(0,2). However, they all have nonzero displacement in the circumferential direction. Most importantly, their

circumferential displacement increases with the increase of circumferential order. Notice that in the last two plots in Figure 2-9 the circumferential displacement is even larger than the axial displacement for L(9,2) and L(10,2).

The wave structures of the modes in the first torsional mode group T(n,1) are shown in Figures 2-10 and 2-11. As can be observed from the previous phase velocity and group velocity dispersion curves, the axisymmetric mode T(0,1) is nondispersive over the whole frequency range. In addition, its nonzero displacement is only in the circumferential direction. These characteristics are also found in the model behavior of the SH mode in a plate. The higher order flexural modes in this mode group have very similar circumferential displacement distribution as that of the T(0,1) mode, while their displacement in the axial and thickness direction increases with the increase of circumferential order n.

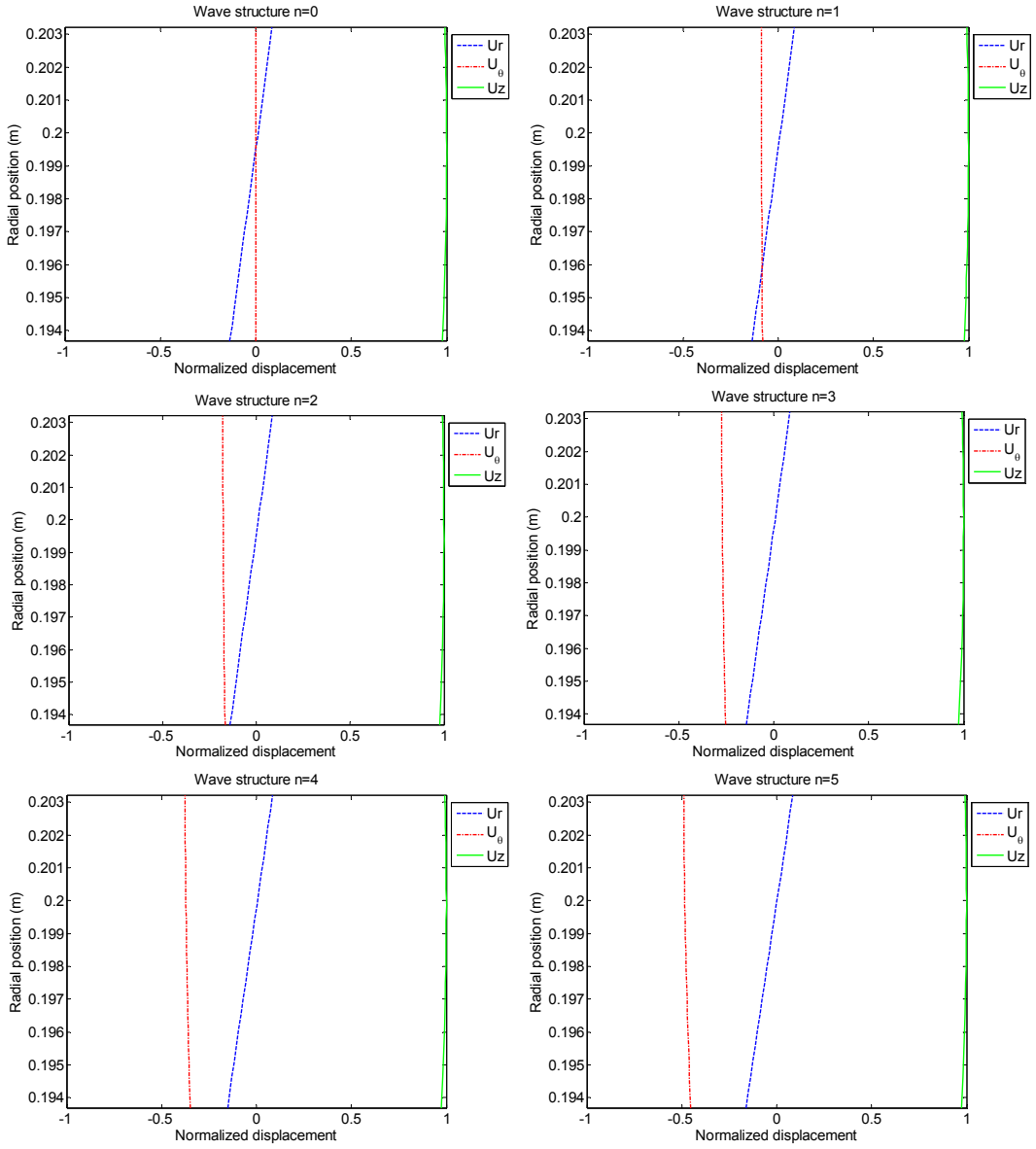

Figure 2-8: Wave structures of guided wave modes L(*n*,2) in a 16 *in*. schedule 30 steel pipe. Circumferential order *n* varies from 0 to 5.

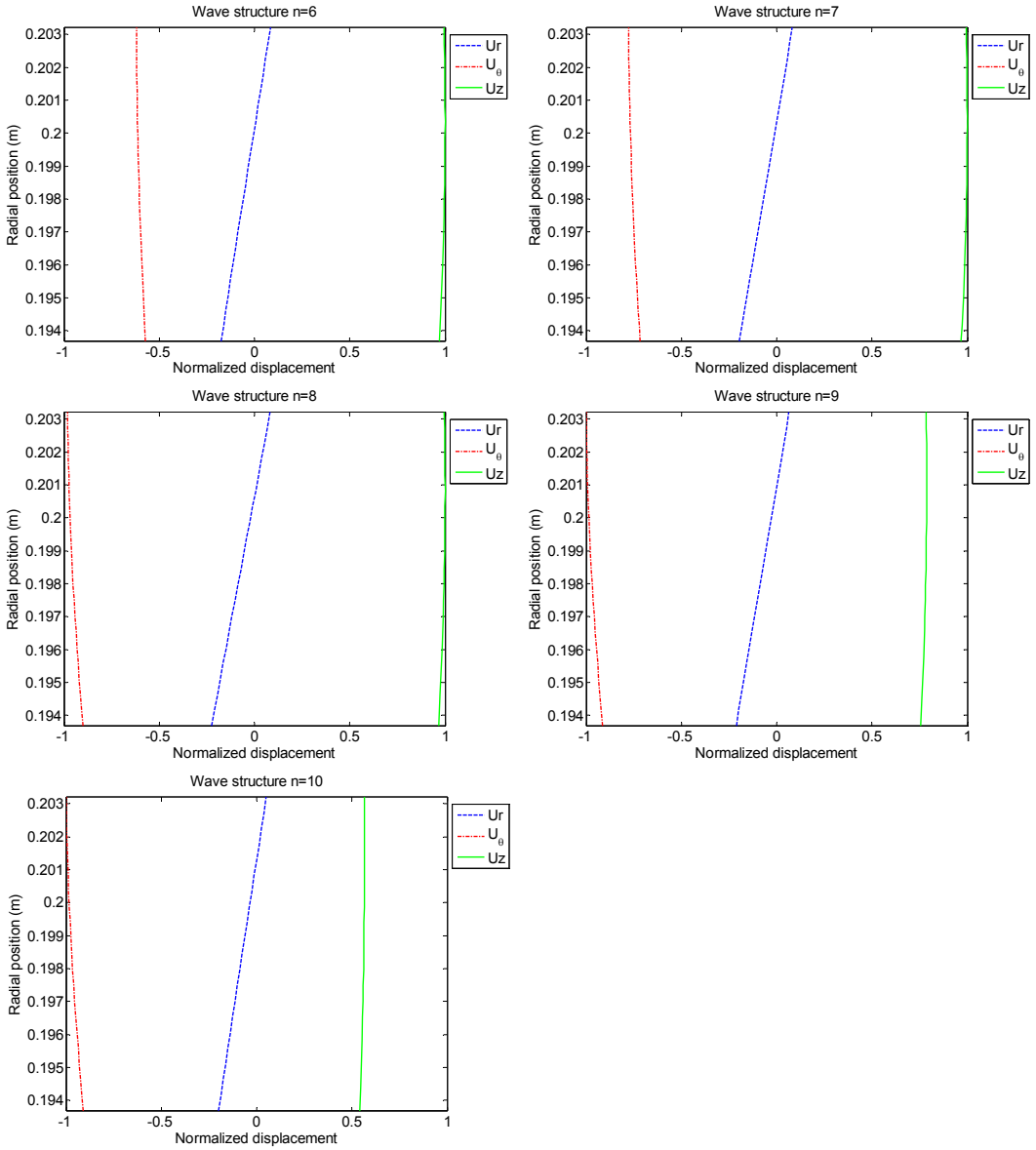

Figure 2-9: Wave structures of guided wave modes L(*n*,2) in a 16 *in*. schedule 30 steel pipe. Circumferential order *n* varies from 6 to 10

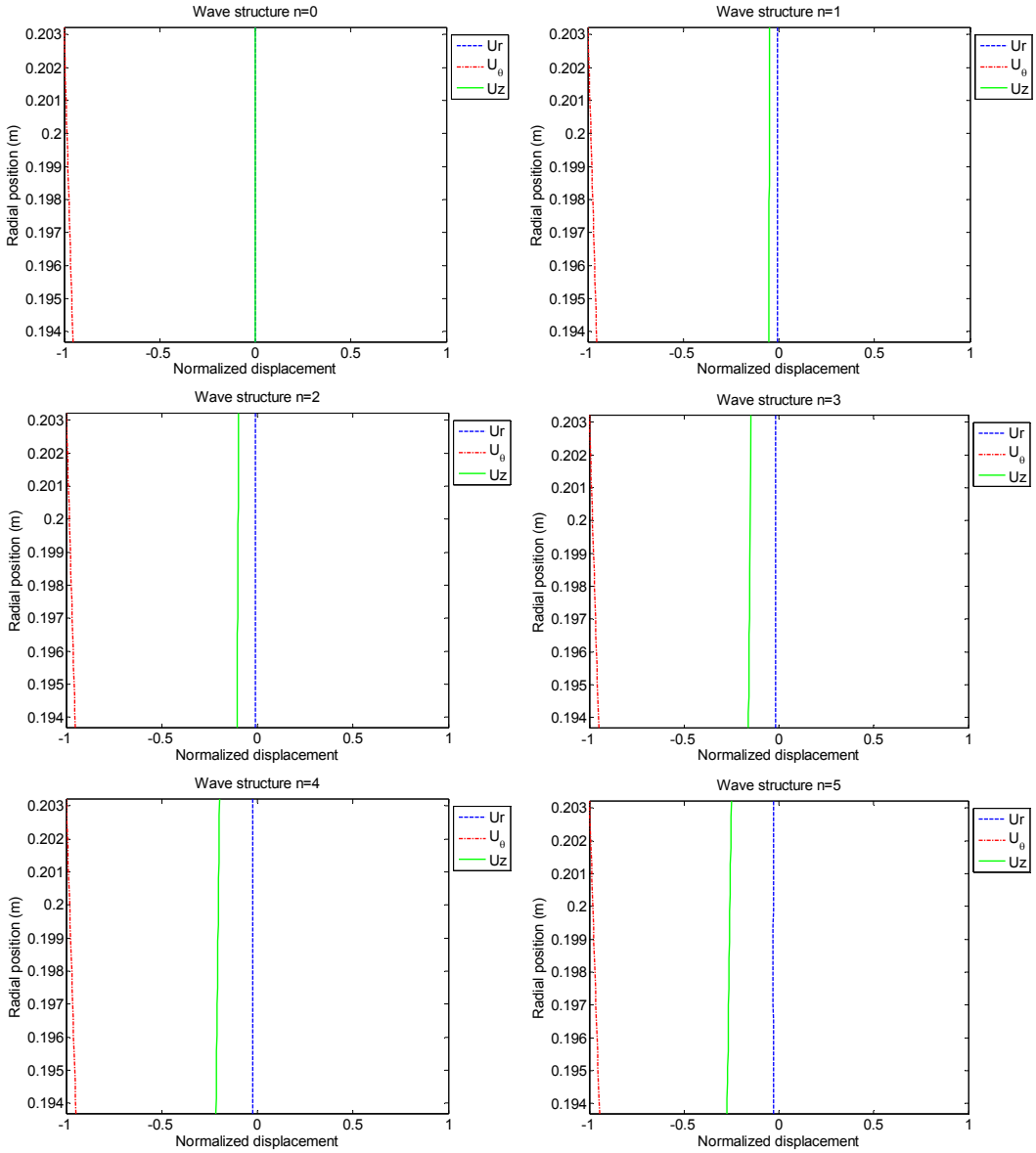

Figure 2-10: Wave structures of guided wave modes T(*n*,1) in a 16 *in*. schedule 30 steel pipe. Circumferential order *n* varies from 0 to 5.

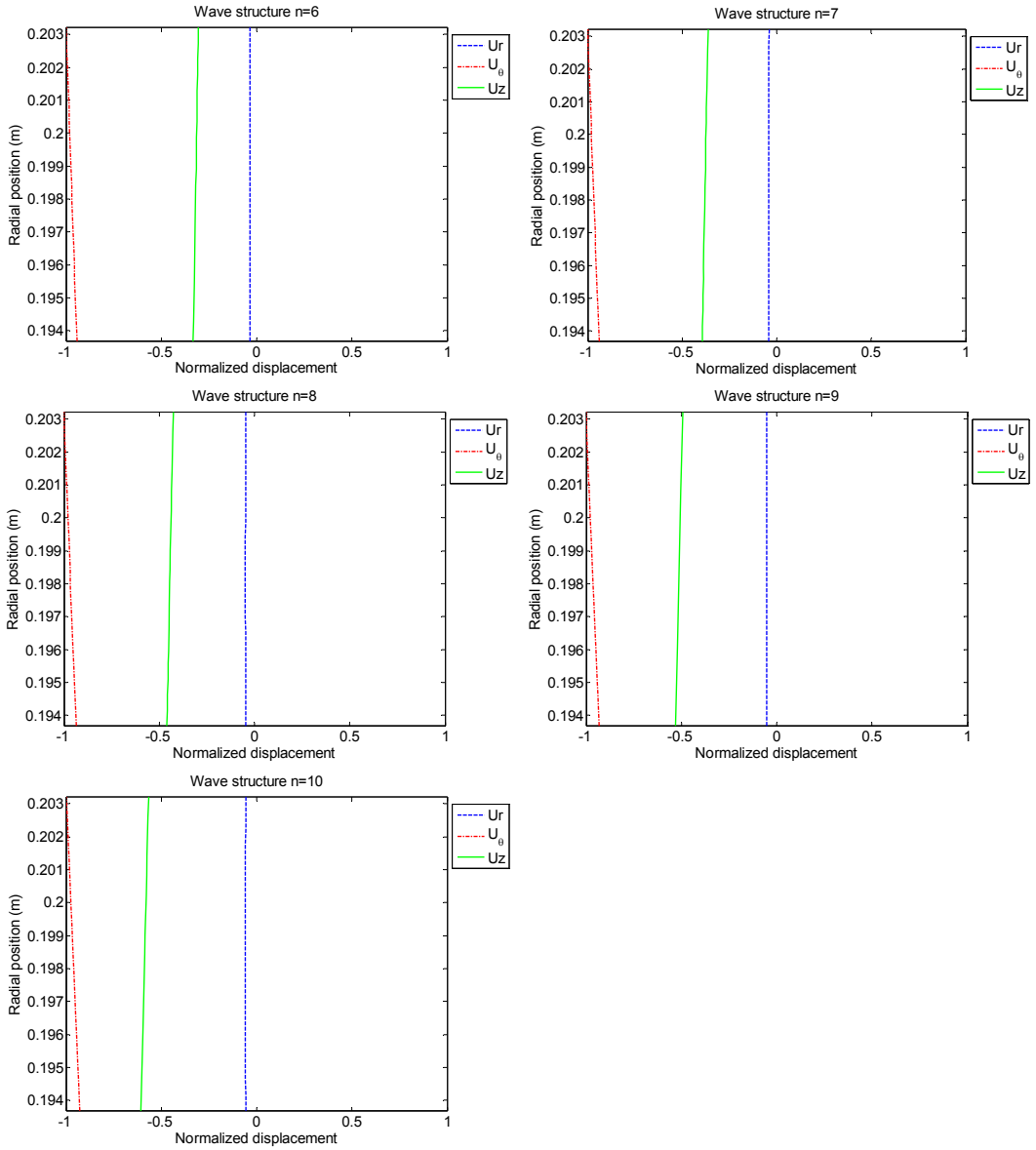

Figure 2-11: Wave structures of guided wave modes T(*n*,1) in a 16 *in*. schedule 30 steel pipe. Circumferential order *n* varies from 6 to 10.

It is easily seen that guided wave modes are much more complex than bulk wave modes. This complexity makes it difficult to study and utilize guided waves. However, there are also benefits. Since different modes have different characteristics, they can be used for different inspection purposes. For example, wave modes that have dominant in-

plane displacements are suitable for water loaded pipe inspection because energy leakage into water can be effectively avoided. The key point is how to control all of these modes. The utilization of guided waves in pipe inspection is basically an issue of mode control. How well guided wave modes can be used depends on how well we are able to control them. This is an inverse problem and it will be discussed in details in the following sections and chapters.

2.3 Normal Mode Expansion and Source Influence

The first step in mode control is to study source influence. That is to say, if a certain type of transducer with its size known is applied to the pipe surface (as shown in Figure 2-12), what kind of wave field distribution is produced in the pipe. There are many ways to tackle this problem, such as using the virtual work principle, variational method, integral transform method, normal mode expansion technique, and finite element method. Among all of these, the one that is the most straightforward and the easiest to interpret a physical meaning is the normal mode expansion technique. The normal mode expansion is used on the basis of guided wave mode orthogonality. Therefore, it is essential to find the orthogonality relation between the wave modes in order to solve the source influence problem.

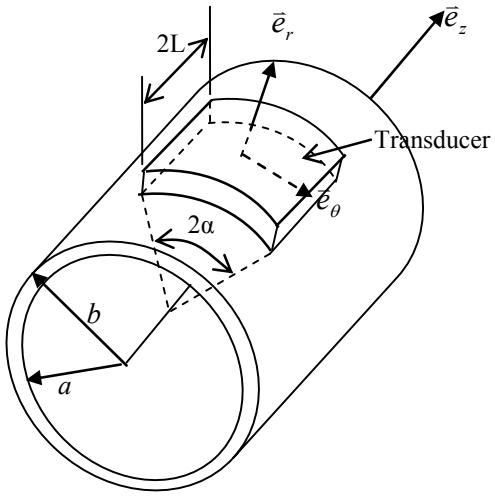

Figure 2-12: An elastic isotropic hollow cylinder loaded by an ultrasonic transducer

The orthogonality of the modes in a typical dispersion curve of an elastic, isotropic, homogeneous pipe was first proved by Ditri and Rose [1992]. The orthogonality relation is given by

$$P_{nm}^{MN} = 0, \text{ unless } m = n \text{ and } k_m^N = k_n^M, \qquad 2.12$$

where $\mathrm{P}_{nm}^{MN} = -\frac{1}{4}\int\int_D (\mathbf{v}_n^{M*} \cdot \mathbf{T}_m^N + \mathbf{v}_m^N \cdot \mathbf{T}_n^{M*}) \cdot \vec{e}_z dV$ and where **v** and **T** are the particle velocity vector and stress tensor of the nth or mth circumferential order, i.e. the order of the Bessel functions, and the Mth or Nth root of the corresponding Bessel functions, i.e. the Mth or Nth mode group.

This orthogonality relationship shows that the guided wave modes in an infinite elastic, isotropic hollow cylinder are all orthogonal to each other. On the basis of this orthogonality relation, the Normal Mode Expansion (NME) can be carried out to determine how much amplitude of each normal mode must be generated by a known

partial loading. For a source loading shown in Figure 2-12, the loading condition can be described as

$$\mathbf{T}\cdot\mathbf{n}=\begin{cases}-p_1(\theta)p_2(z)\vec{e}_r, & |z|\le L, |\theta|\le\alpha, r=b\\ 0, & |z|>L, or \quad |\theta|>\alpha, or \quad r\ne b\end{cases} \tag{2.13}$$

where n is the normal vector of the loading surface.

The amplitude of the L(n, M) mode generated by the above source is then given by

$$A_{+n}^{M}=-\frac{R_{nr}^{M*}(r)e^{-ik_n^M z}}{4\mathrm{P}_{nn}^{MM}}\int_{-\alpha}^{-\alpha+2\pi}\Theta_r^n(n\theta)p_1(\theta)d\theta \int_{-\infty}^{\infty}p_2(z)e^{ik_n^M z}dz, \tag{2.14}$$

where $R_{nr}^{M}(r)$ is the wave structure in the r direction for mode L(n, M). $\Theta_r^n(n\theta)$ is the circumferential displacement distribution, which is basically a sinusoidal function. As can be observed from Eq. 2.14, when the source loading is axisymmetric, which can be represented by $p_1(\theta)=1$ for $0\le\theta<2\pi$, the first integral in Eq. 2.14 vanishes except for n=0. This explains quite well the fact that only axisymmetric modes will be generated in the case of axisymmetric source loading.

Typical amplitude factor distributions for 45° and 60° shear source loading is shown in Figure 2-13 and Figure 2-14. The amplitude factors for the first 16 modes generated in a 16 *in*. schedule 30 steel pipe at a frequency of 50 kHz are calculated and displayed. Notice that the first several modes are generated with significant amplitude factors and the other higher order modes have significantly less amplitudes.

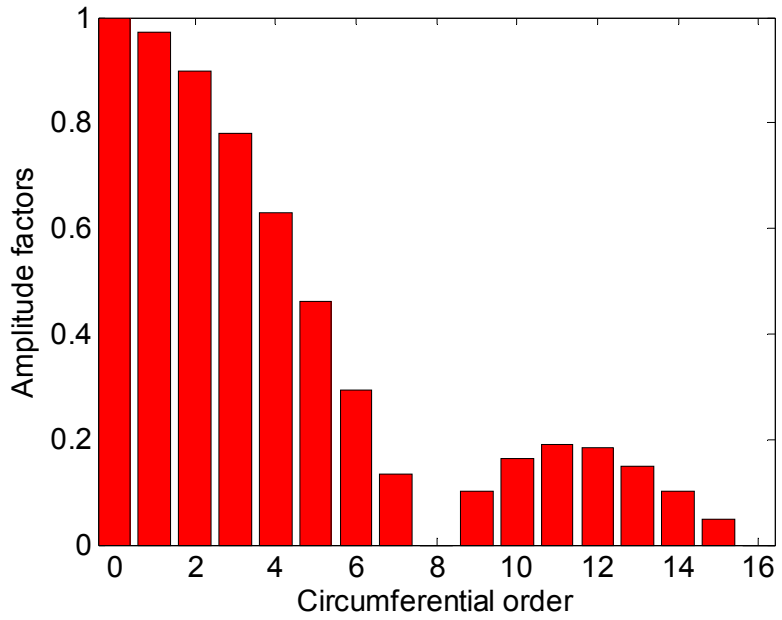

Figure 2-13: Normalized amplitude factors of the T(n,1) mode group when 45° normal loading is applied to a 16 *in*. schedule 30 steel pipe at a frequency of 50 kHz.

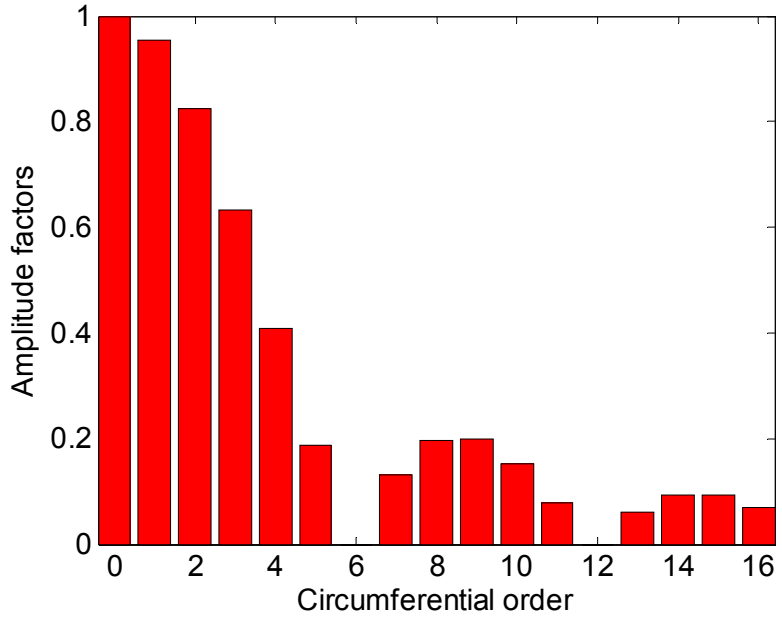

Figure 2-14: Normalized amplitude factors of the T(n,1) mode group when 60° normal loading is applied to a 16 *in*. schedule 30 steel pipe at a frequency of 50 kHz.

Summing up the above generated modes weighted by their corresponding amplitude factors and phases yields the guided wave displacement distribution or interference pattern in the specific pipe. A polar plot illustrates the displacement distribution around the pipe circumference at a certain axial distance from the transducer location; this distribution is called an angular profile. The angular profiles of the L(n,2) mode group at different axial distances for the 45° source loading on the 16 *in*. schedule 30 steel pipe at 50 kHz are demonstrated in Figure 2-15. It can be clearly seen from Figure 2-15 that the energy is concentrated on the top of the pipe when the axial distance is close to the transducer (Figure 2-15(a)). Then, the energy spreads out as the axial distance increases (Figure 2-15(b)-(f)).

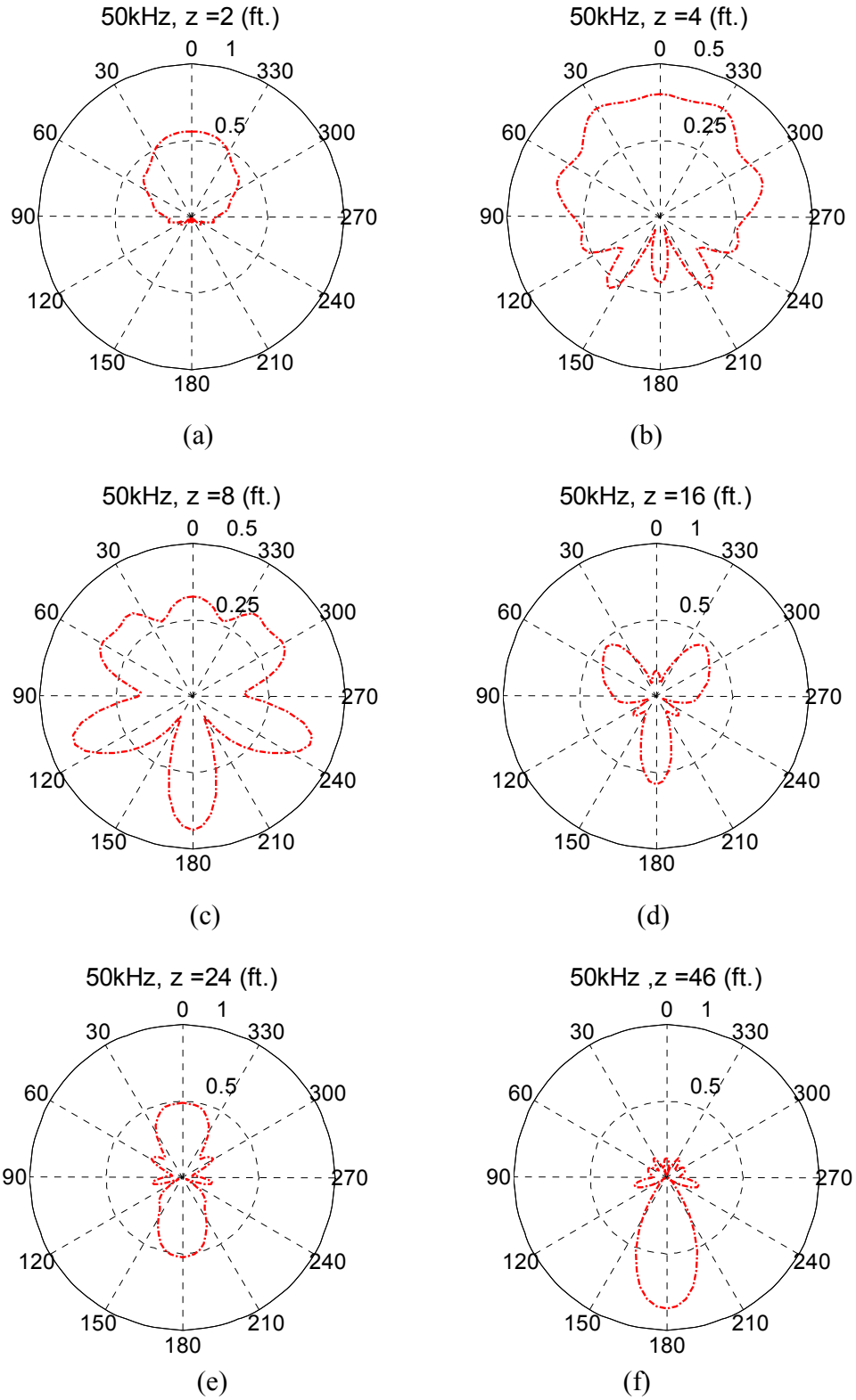

Figure 2-15: The angular profiles of the L(n,2) mode group at different axial distances for 45° source loading on a 16 *in*. schedule 30 steel pipe at a frequency of 50 kHz.

Figure 2-16 illustrates the guided wave interference pattern (unwrapped) of the L(n,2) mode group by 45° source loading on a 16 *in*. schedule 30 steel pipe at a frequency of 50 kHz. The horizontal axis represents the axial distance and the vertical axis is the circumferential angle. The source loading is centered at 0° as can be seen in Figure 2-16. The propagation distances used in the angular profile calculation in Figure 2-15 are also marked in Figure 2-16 by vertical magenta lines. It can be clearly seen that Figures 2-15 and 2-16 agree quite well. The interesting phenomenon of guided wave natural focusing is clearly shown in Figure 2-16 at about 46 *ft*. in axial distance. The first natural focusing happens at angle 180°, opposite to the source loading position in the circumference. It agrees very well with the angular profile shown in Figure 2-15(f).

Two more examples of partial loading source influence of the unwrapped pipe for 60 and 70 kHz are shown in Figures 2-17 and 2-18 respectively. As can be observed from Figure 2-16 to Figure 2-18, the 45° source influence of the pipe shares similar constructive and destructive interference patterns at different frequencies. The constructive and destructive interference pattern moves toward $z = +\infty$ with the increase of frequency. This agrees with Li and Rose [2006], who pointed out that the distance of the first natural focal point increases with the decrease of wavelength and the increase of pipe diameter.

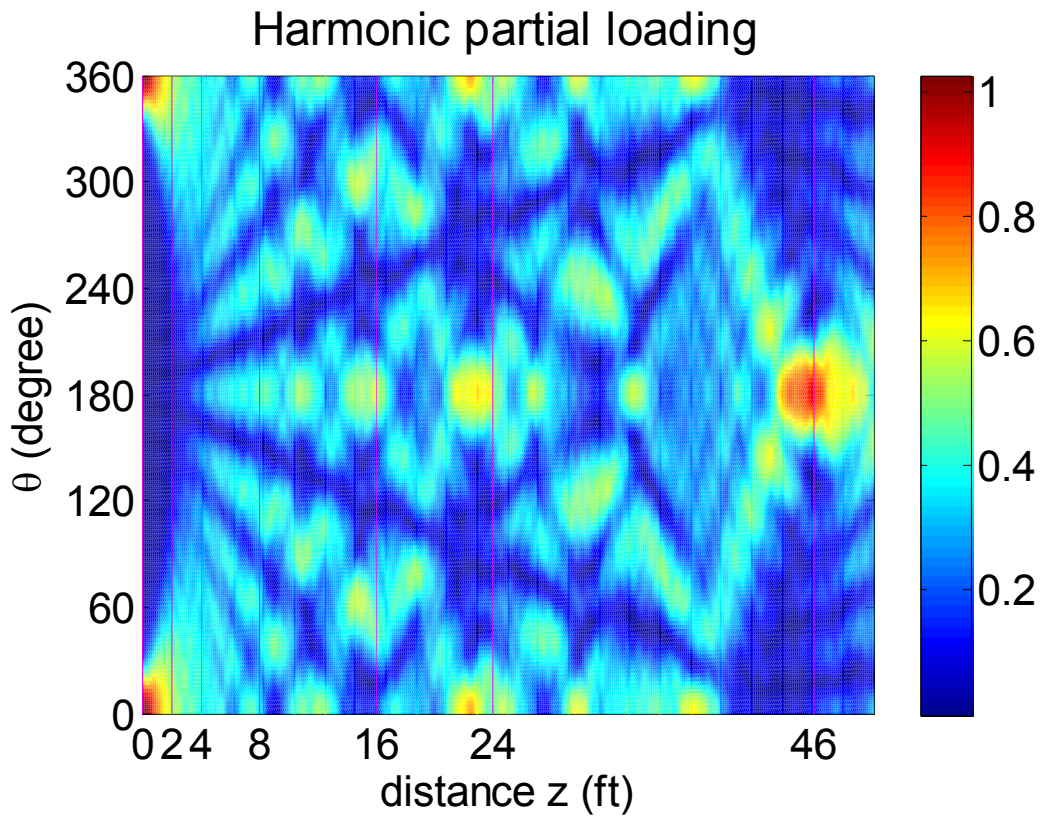

Figure 2-16: Guided wave interference pattern of the L(n,2) mode group by 45° source loading on a 16 *in*. schedule 30 steel pipe at a frequency of **50** kHz.

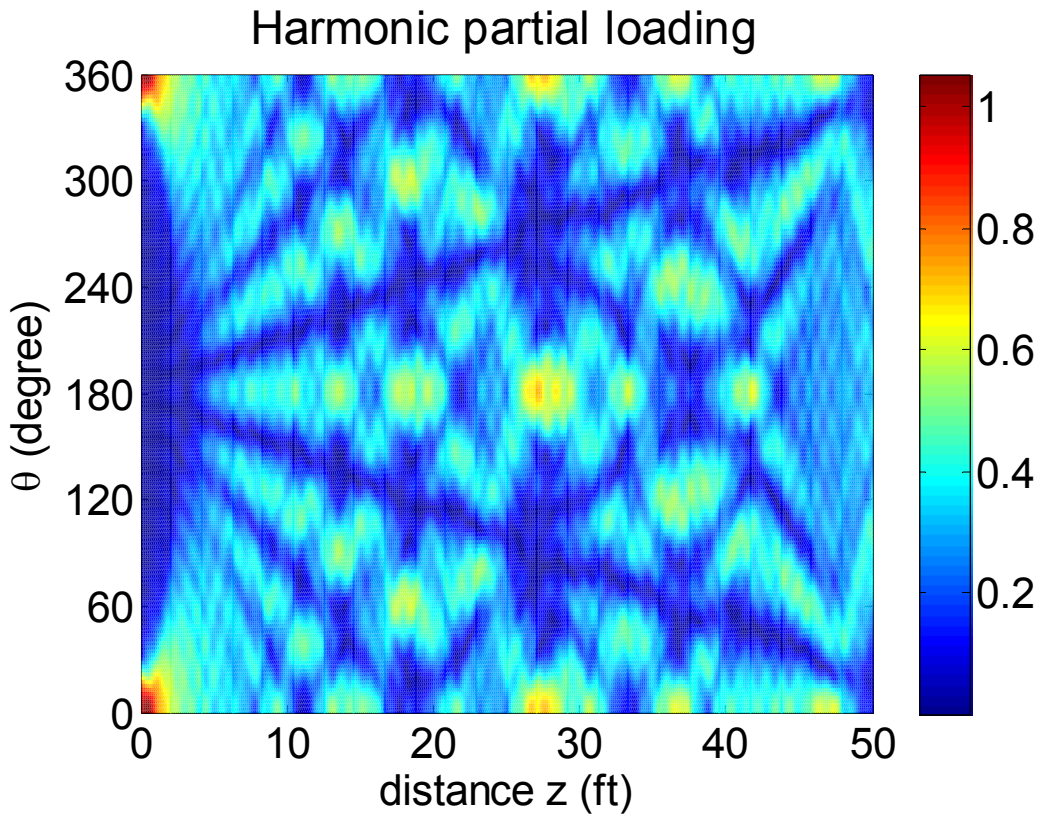

Figure 2-17: Guided wave interference pattern of the L(n,2) mode group by 45° source loading on a 16 *in*. schedule 30 steel pipe at a frequency of **60** kHz.

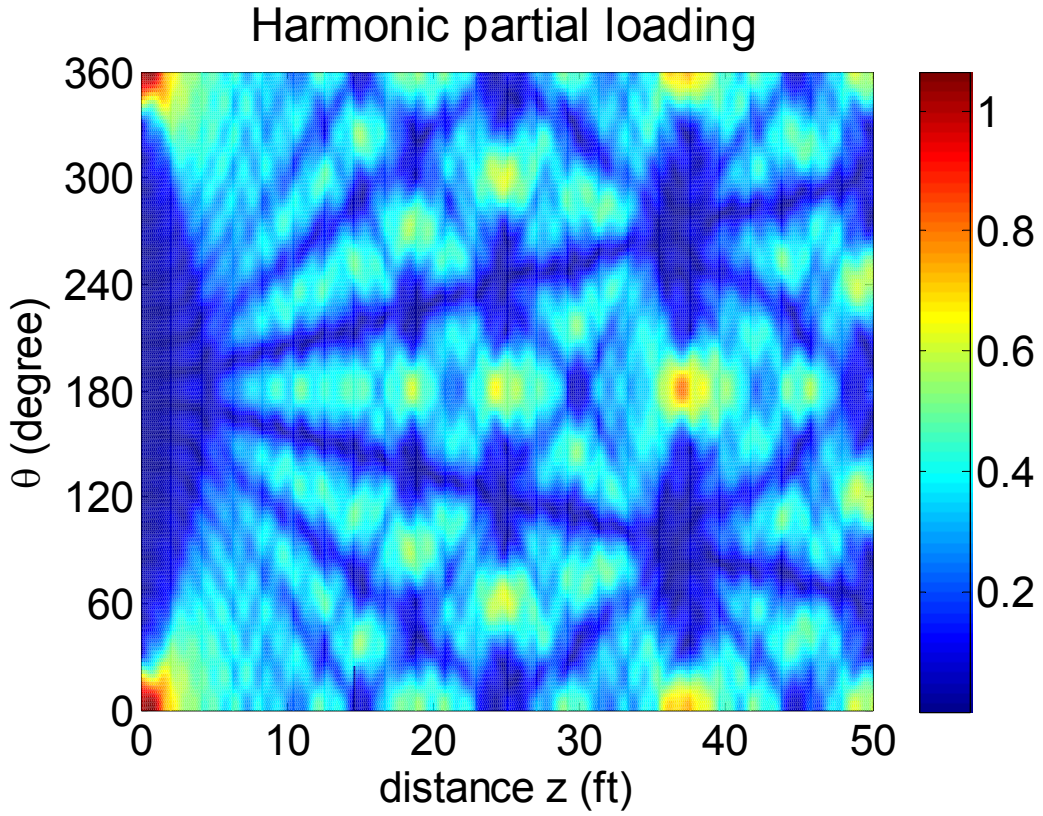

Figure 2-18: Guided wave interference pattern of the L(n,2) mode group by 45° source loading on a 16 *in*. schedule 30 steel pipe at a frequency of **70** kHz.

Chapter 3

Phased array focusing techniques and its application to defect imaging in pipes

3.1 Guided wave focusing theories

Angular profiles from sensors around the circumference of a pipe can be used to produce focusing with appropriate amplitudes and time delays. By summing up the appropriate amount of each mode that can be generated by a certain type of source loading, Li and Rose [2001] numerically calculated the particle displacement distribution around the circumferential direction (angular profile) at any given axial distance for waves propagating in a hollow cylinder under source influence. They also verified their numerical calculations by experimental measurement of angular profiles. As a partial loading element generates non-axisymmetric angular profiles along the axial distance in a pipe, the angular profiles resulting from a number of sensors can be tuned with a circumferentially distributed phased array with different amplitude and time-delay inputs to each channel. In 2002, Li and Rose utilized a deconvolution algorithm to generate the appropriate amplitudes and time-delays that are needed for the phased-array to focus on a predetermined position in a pipe.

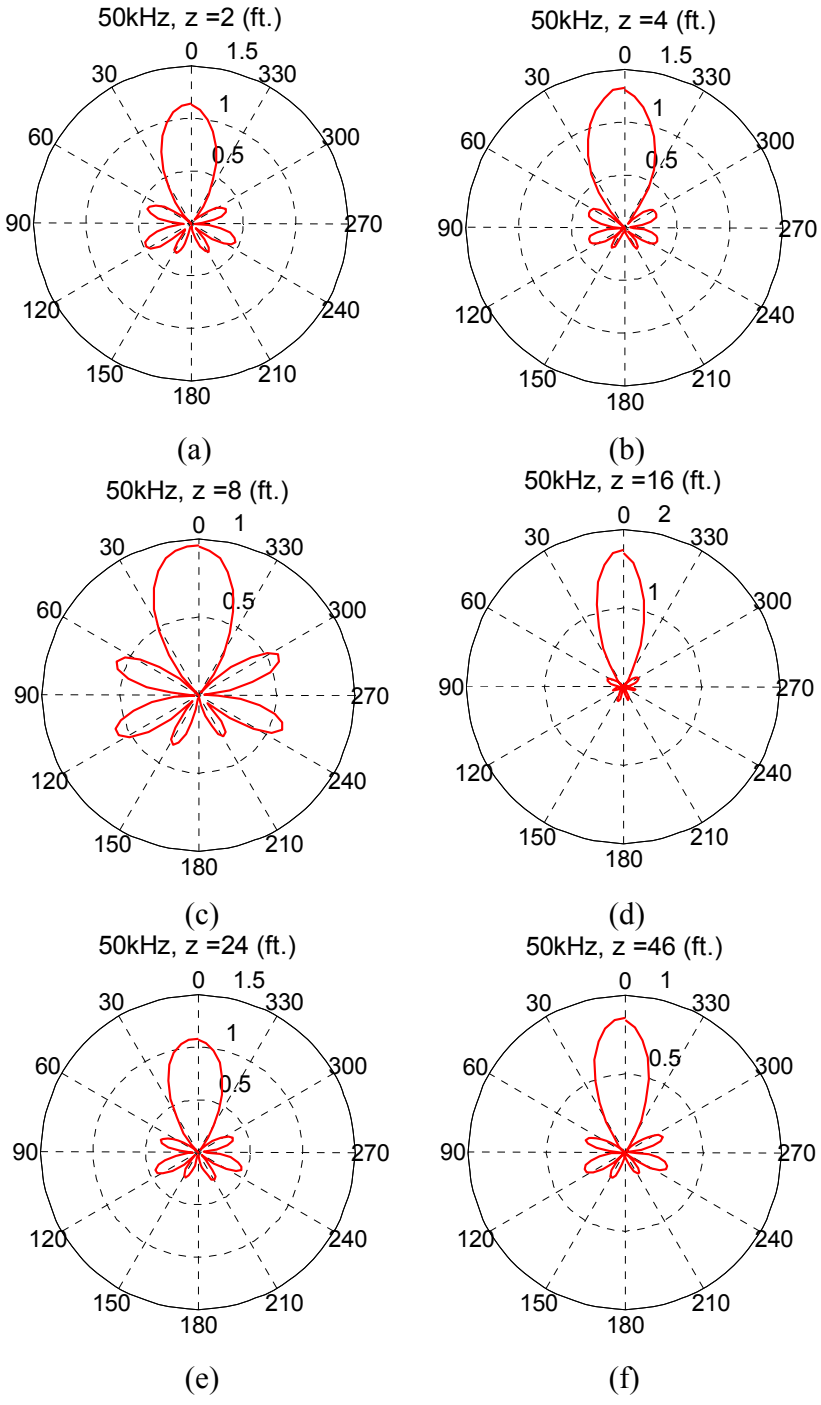

Figure 3-1: The resulting focused angular profiles of the L(n,2) mode group at different axial distances for 45° source loading on a 16 *in*. schedule 30 steel pipe at a frequency of 50 kHz, when using appropriate time delays and amplitudes to the channels around the circumference of the pipe.

The focused angular profiles corresponding to the partial loading angular profiles in Figure 2-15 are shown in Figure 3-1. Table 3-1 lists the amplitude factors and time delays used to achieving the focused profiles in Figure 3-1 (e) and (f). The amplitude factors and time delays are usually different for focusing at different axial distances. At some focal distances, for example 16 *ft*., the guided waves are more focused than others. Figure 3-2 shows two focused profiles for the same pipe at frequencies 50 and 65 kHz. It can be seen that the focused profile at 65 kHz provides better penetration power with relatively smaller side lobes. In general, the frequency can be tuned to achieve a better focused profile with smaller side lobes.

Table 3-1: Amplitude factors and time delays for obtaining the focused profiles in Figure 3-1 (e) and (f).

Channel no.		1	2	3	4	5	6	7	8
Figure 3-1 (e)	Amplitude factor	0.72	0.40	0.16	0.28	1.00	0.28	0.16	0.40
	Time delay (μs)	4.1	19.2	6.9	11.9	17.9	11.9	6.9	19.2
Figure 3-1 (f)	Amplitude factor	0.20	0.11	0.09	0.11	1.00	0.11	0.09	0.11
	Time delay (μs)	4.8	14.0	17.5	5.4	12.5	5.4	17.5	14.0

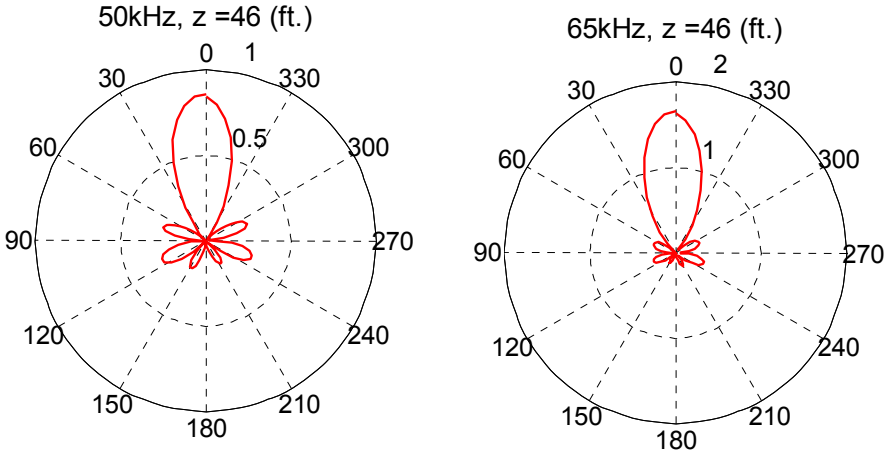

(a) (b)

Figure 3-2: The focused angular profiles of the L(n,2) mode group at different axial distances for 45° source loading on a 16 *in*. schedule 30 steel pipe at a frequency of 50 kHz for two different frequencies 50 and 65 kHz, showing that focused profile changes with frequency.

As an illustrative example, the focused angular profiles for different number of channels are shown in Figure 3-3. It can be seen that the size of a focused beam is reduced with an increase in the number of channels. A narrower focused beam width is good because it will give higher circumferential resolution in defect sizing. However, the cost also increases with an increase in channel numbers because scanning completely around the circumference becomes more difficult.

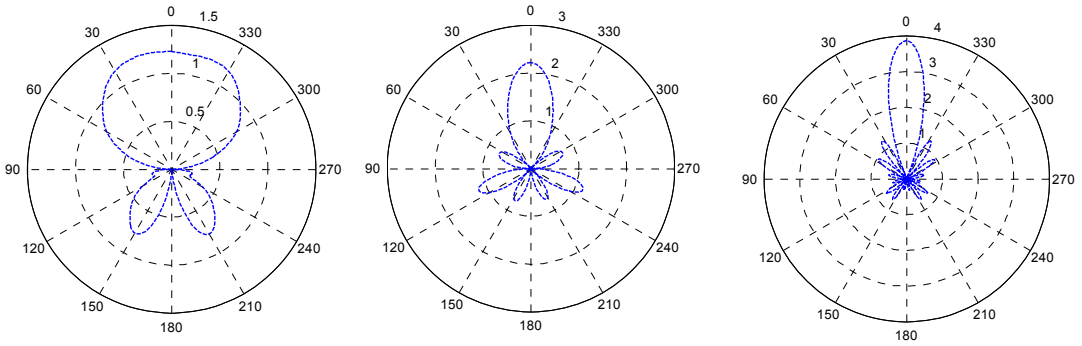

(a) 4-channel (b) 8-channel (c) 16-channel

Figure 3-3: Focused angular profiles by using phased-array focusing techniques for different number of channels. Torsional modes T(n,1) at 40 kHz are used to focus at 11 ft. axial distance in a 16 in. schedule 30 steel pipe.

The computational process of achieving phased-array focusing in pipes is summarized in Figure 3-4. The problem starts from a separation of variables in the governing equations. The normal modes in the dispersion curves are obtained by applying gauge invariance and boundary conditions. The waves generated by a certain source loading are represented in terms of these normal modes. A deconvolution algorithm is then involved to calculate the time delays and amplitude factors to focus at a specific location in a pipe.

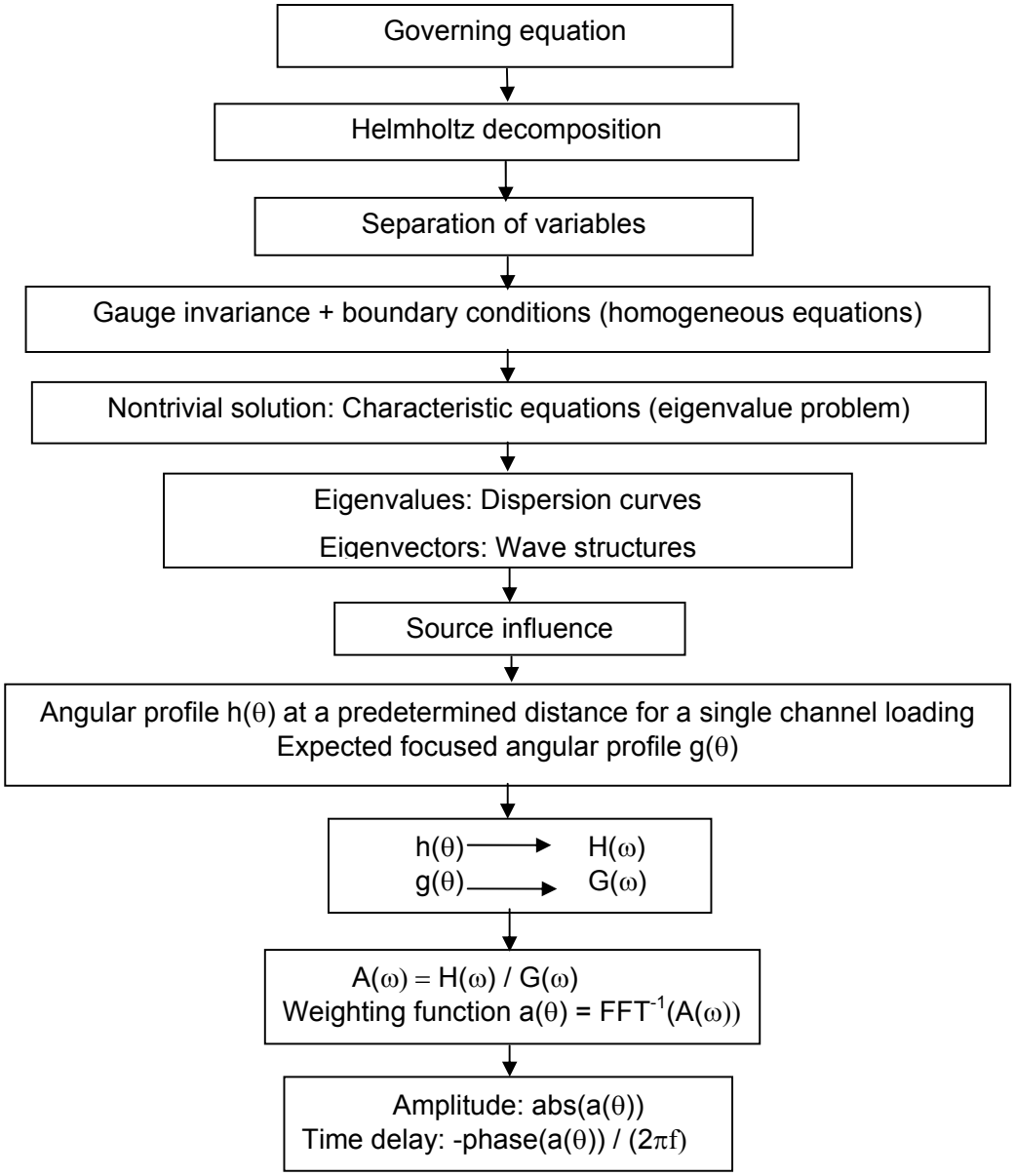

Figure 3-4: The Phased-array focusing technique in pipes

3.2 Finite element simulation of guided wave focusing

FE modeling is increasingly used in various fields because of its flexibility. It is suitable for problems with complex structures and can also be used as a tool to verify

theories and to visualize physical phenomenon. Many commercial software codes are currently available in the market place that are easy to use. In this study, Abaqus is adopted to simulate wave propagation in pipes. The maximum length of the elements is chosen to be no more than one-eighth of a wavelength. The time steps in calculation are automatically decided by Abaqus. If chosen manually, the time steps should be at least several times less than the period of the input signal and less than the time ultrasonic wave propagates from one end of the element to the other end.

For comparison purposes, axisymmetric wave propagation in a pipe is also computed and given in Figure 3-5 to compare with the focusing case. Axisymmetric waves are generated by an axisymmetric source loading at one end of the pipe. In Abaqus, it can be simulated by using axisymmetric boundary conditions at one end of the pipe. As can be seen from Figure 3-5, the generated waves stay axisymmetric as they propagate along the pipe.

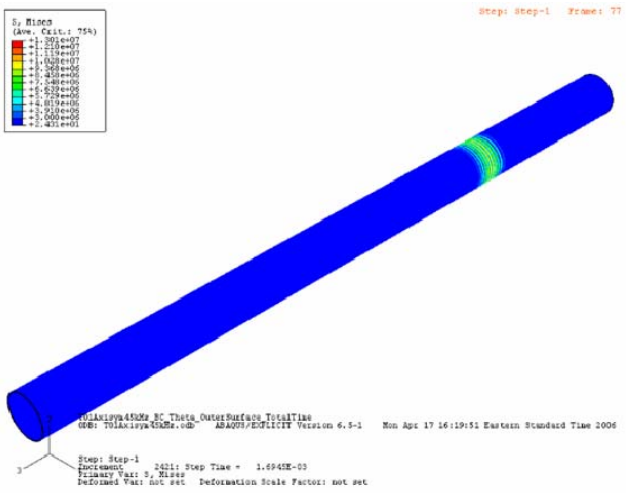

Figure 3-5: T(0,1) axisymmetric wave at a frequency of 45kHz propagating in a 16 in. schedule 30 steel pipe. The transducers are located at the left end of the pipe.

Guided wave focusing by using 4 and 8 channels is also simulated and shown in Figure 3-6(a) and Figure 3-7(a). Figure 3-6(b) and Figure 3-7(b) are their corresponding focused profiles obtained from both theoretical calculation and FEM simulation. It can been seen that compared to the axisymmetric wave in Figure 3-5, the guided waves in Figure 3-6 and Figure 3-7 are effectively focused. It is also clear from both the focusing simulations and focused angular profiles that 8-channel focusing provides a much narrower focal beam than 4-channel focusing. The focal beam width is usually about the same as the circumferential length of each channel in the phased array. Therefore, the greater the number of channels one uses, the narrower the focal beam that one can obtain.

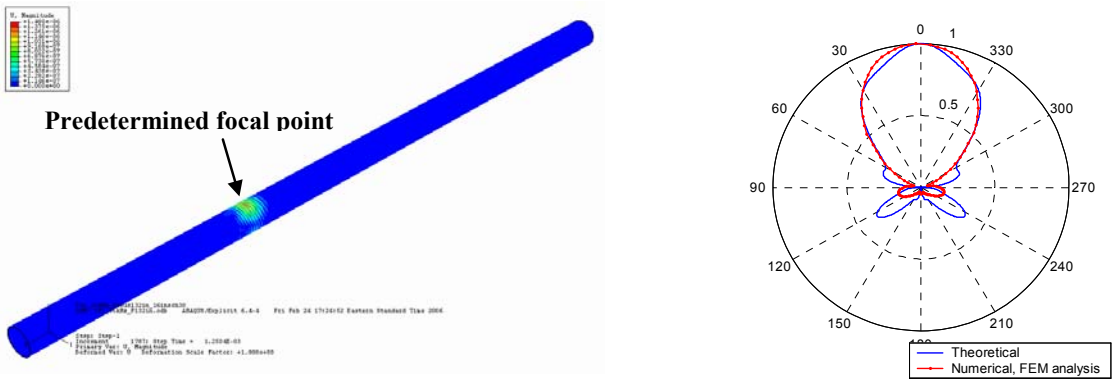

(a) (b)

Figure 3-6: Torsional waves at 35kHz are focused at 3.35 m. axial distance in a 16 in. schedule 30 steel pipe. 4 channels are used to achieve focusing.

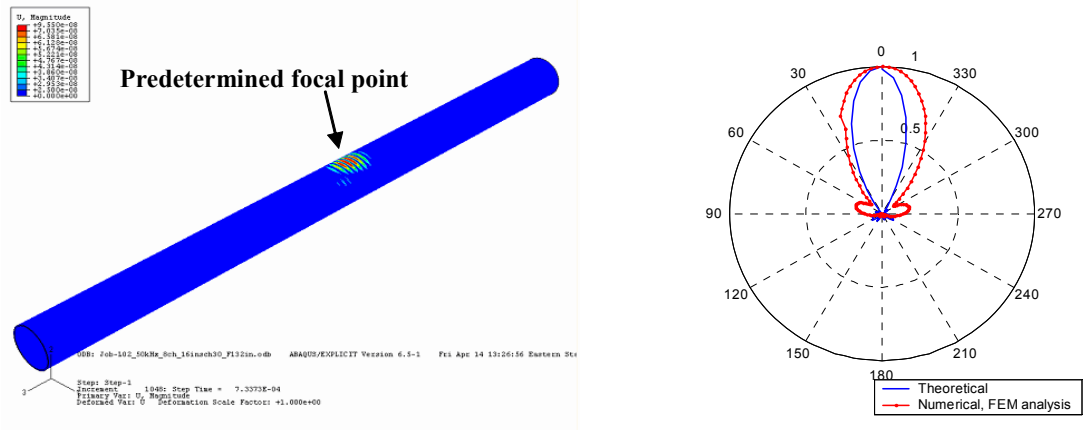

(a) (b)

Figure 3-7: Longitudinal waves L(m,2) at 50kHz are focused at 3.35 m. axial distance in a 16 in. schedule 30 steel pipe. 8 channels are used to achieve focusing.

3.3 Focusing application in defect detection and pipe imaging

The multi-channel commercial system TeleTest®, as shown in Figure 3-8, was used to apply the phased array focusing technique. The system has 44 modules that can be segmented over four quadrants or eight octants as indicated in Figure 3-8. Different time delays and amplitude factors can be input to the system in order to tune the guided wave energy to focus at different positions in a pipe. In each module, 3 piezoelectric transducers are mounted in the axial direction. With 44 modules mounted on the circumference of the pipe, three rings of transducers are obtained. In experiments, these three rings are input with different time delays, so that the ultrasonic energy can be sent to only one direction (either forward or backward) from the transducer array only.

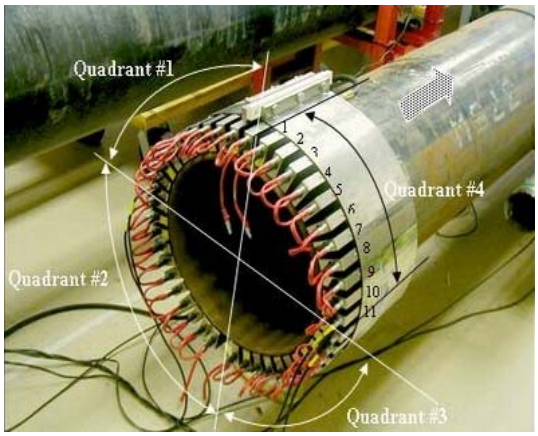

Figure 3-8: TeleTest® tool mounted on a pipe.

In a circumferential scan, the time delays and amplitude factors are calculated for multiple focal positions around the circumference in order to spin the focal beam around the pipe at each focal distance. A full scan of the pipe is achieved by carrying out circumferential scans at different distances. On the receiving side, a time gate is set for each received waveform and the maximum amplitude within the time gate is recorded according to the axial length of the focal zone. These maximum amplitude values can be plotted with respect to the focal positions in displaying the final image of the pipe by a focal scan. They can also be plotted according to the focal angles in the circumference at each distance in obtaining a circumferential profile. The circumferential profiles illustrate the circumferential distribution of the anomaly located inside the focal zone. When an anomaly is located in the focal zone, a large reflection can be expected. For an anomaly with a non-axisymmetric feature, for example, a defect, the circumferential profile will be nonaxisymmetric. However, if the anomaly has an axisymmetric feature, such as a weld, the circumferential profile is approximately axisymmetric. In this way, defects can be differentiated from welds quite easily. In the following, field test results are provided to

illustrate defect detection as well as pipe imaging using the real-time phased array focusing technique.

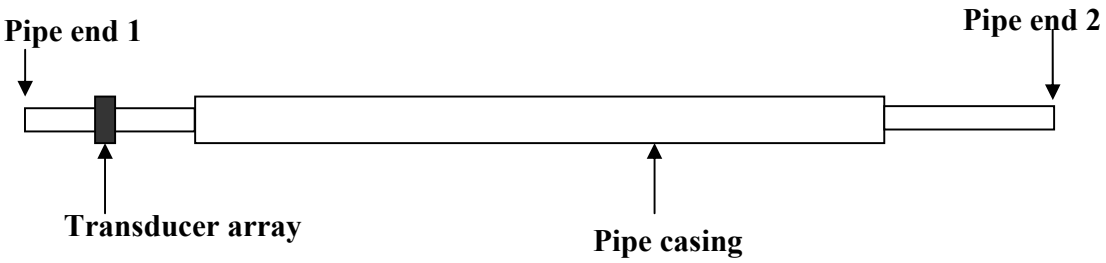

Figure 3-9: Schematic of the field test on a 20 *in*. schedule 40s steel cased pipe.

A guided wave focal scan field test was conducted on a 20 *in*. schedule 40s 80 ft. long steel cased pipe as shown in Figure 3-9. In the test, the phased array was segmented into 4 channels. Theoretically, the 4 channel focused profile in general covers about 90° and scanning 4 equally spaced positions around the pipe circumference for each focal distance should be enough to cover the whole circumference. However, in order to make sure the full coverage of energy on the circumference, 8 equally spaced positions are scanned at each focal distance with the 4 channel focusing to achieve overlap focusing. Longitudinal L(m,2) and torsional T(m,1) wave modes are sent from both sides of the pipe with the transducer array being placed 4’ 9” from either pipe end. Some sample waveforms from the test and their corresponding circumferential reflection profiles are provided and discussed next. Figure 3-10 shows the waveforms received by the phased array when torsional waves T(m,1) were focused at 20’ 9’’ from pipe end 1. The waveforms are displayed in such a way that the zero distance in each plot represents pipe end 1. The focal zone is the region indicated between the two red vertical lines in each

waveform. It can be clearly seen from these waveforms that the biggest reflection inside the focal zone is received when focused at 270°. The axial location can also be precisely determined by the arrival time of the biggest reflection. Notice that there is an echo in front of the gate in the 0° focused waveform. This echo is caused by a defect and it is picked up in the 0° focused waveform because the focal zone is actually longer than the distance indicated by the two red vertical lines in the waveform.

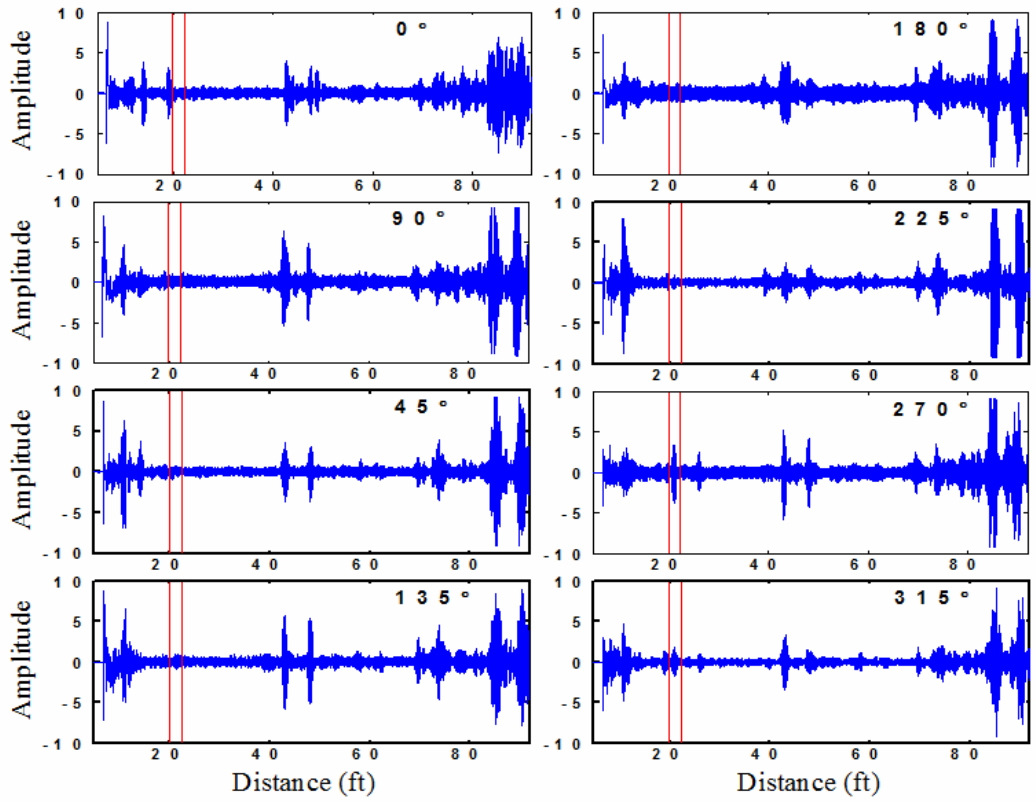

Figure 3-10: Waveforms received by torsional waves T(m,1) focusing at 8 different angles around the circumference at a focal distance of 20 ft. 9 in. from pipe end 1. The red vertical lines gate the effective focal range. Note a defect echo is located at 270°.

The maximum amplitude inside each focal zone is then recorded and plotted with respect to the focal angle in constructing a circumferential plot as shown in Figure 3-11. The profile clearly shows a defect located at about 270°. Note that the smaller reflection

at 315° is likely caused by the focal beam width being twice as large as our circumferentially scanning step.

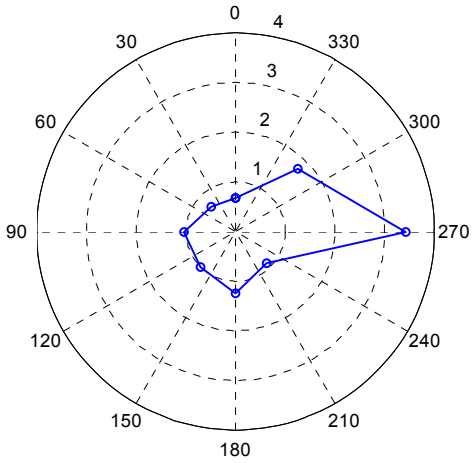

Figure 3-11: The circumferential profile of the defect located at 20 ft. and 270° in the pipe. The unit of the amplitude is mV.

To illustrate the difference in reflection from different anomalies, Figure 3-12 provide the waveforms from spacers located at 11 ft. from pipe end 1. Spacers are distributed around the pipe circumference to support the casing. The waveforms are also taken from torsional wave focus inspection from pipe end 1. Different from defects, spacers are distributed around the pipe circumference. Therefore, evident reflections may be expected at multiple focal angles when the focal beam moves around the pipe. This is well demonstrated in Figure 3-12. The corresponding circumferential profile is shown in Figure 3-13. It can be observed from Figure 3-13 that the amplitudes of the echoes reflected by the spacers are in general larger than the amplitudes of defect reflections. Possible explanations are as follows: first, multiple spacers may be located within the focal beam width; secondly, the spacers are located closer to the transducer array, thus

less attenuation of the focal beam, when focusing at the spacers compared to focusing at the defect shown in Figure 3-11.

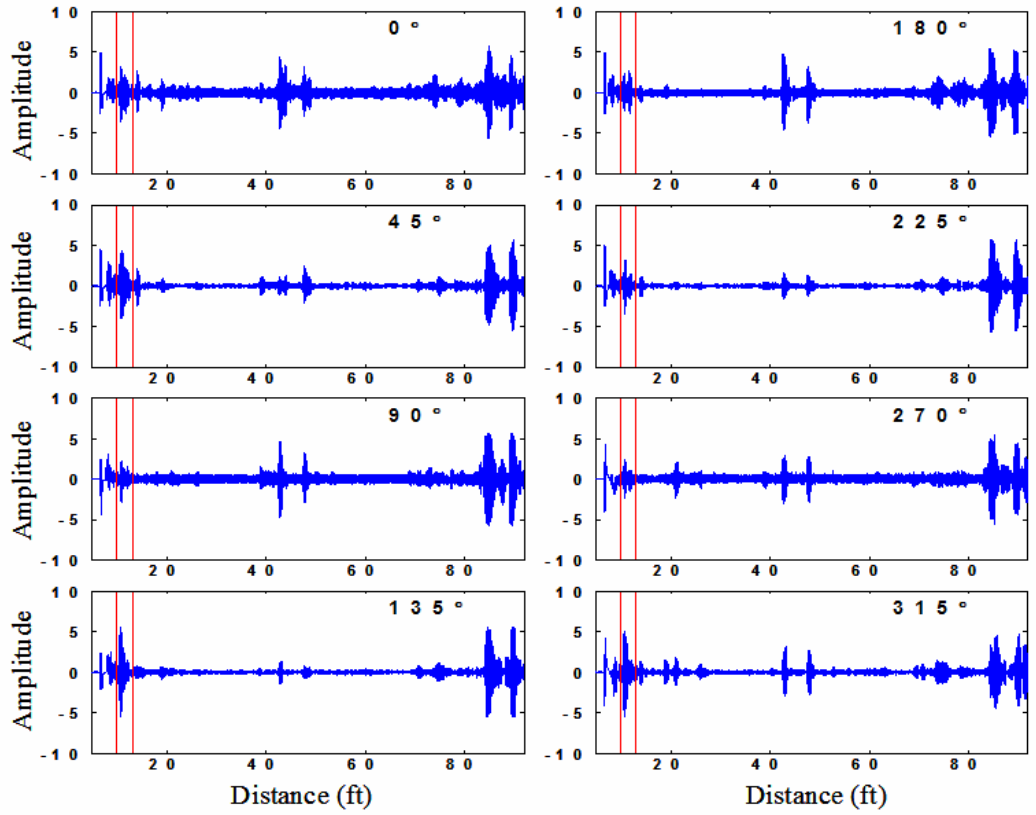

Figure 3-12: Waveforms received by focusing at 8 different angles around the circumference at a focal distance of 12.75 ft. from the pipe end.

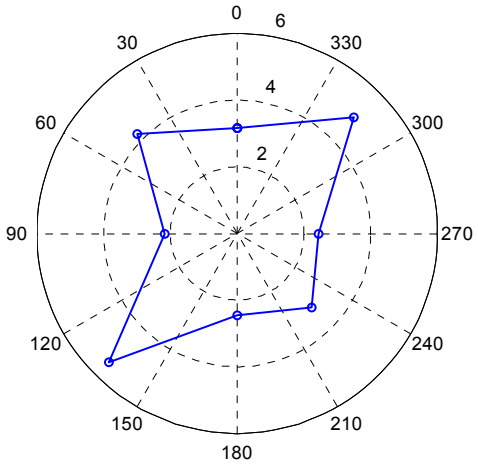

Figure 3-13: The circumferential profile of spacers in the cased pipe located at 11 ft.

Another interesting anomaly to investigate is a weld. A good weld can demonstrate fairly axisymmetric feature in reflecting ultrasonic waves. Figure 3-14 shows the circumferential profile reflected by a weld located at 41ft.11in. inspected by a longitudinal wave L(m,2) focusing from pipe end 2. It can be seen that the circumferential profile is almost axisymmetric in this case. The defect can be well separated from spacers and welds by the circumferential plots of their reflections in a focal scan.

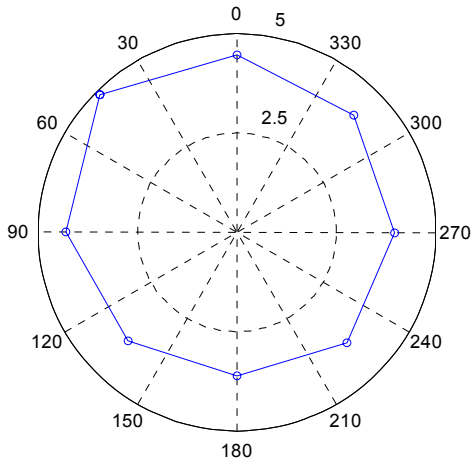

Figure 3-14: The circumferential profile of the weld located at 41ft.11in.

An image of the pipe can be obtained by combining the circumferential plots with focal distance. Figure 3-15 displays the image of the unwrapped pipe. The vertical axis in Figure 3-15 represents the circumferential direction of the pipe and horizontal axis denotes focal distance. The reflection amplitude is displayed in color as a third dimension. Interpolation is conducted in both the circumferential and axial directions to smooth the image. Since the pipe is inspected from both ends, the image is formed by superposition in combining torsional wave inspection from pipe end 1 and longitudinal wave inspection from pipe end 2. Thus, the image has a higher signal to noise ratio than that of using the inspection results from a single pipe end. Also, due to the fact that guided waves attenuate as they propagate along the pipe, the guided wave attenuation along the pipe is compensated by $e^{2\alpha z}$, where α is the attenuation factor and z is the focal distance. The attenuation factor can be measured experimentally from pipe end reflection or from the reflections of multiple welds. In this study, α is estimated empirically to magnify the signal in the axial direction in the pipe image.

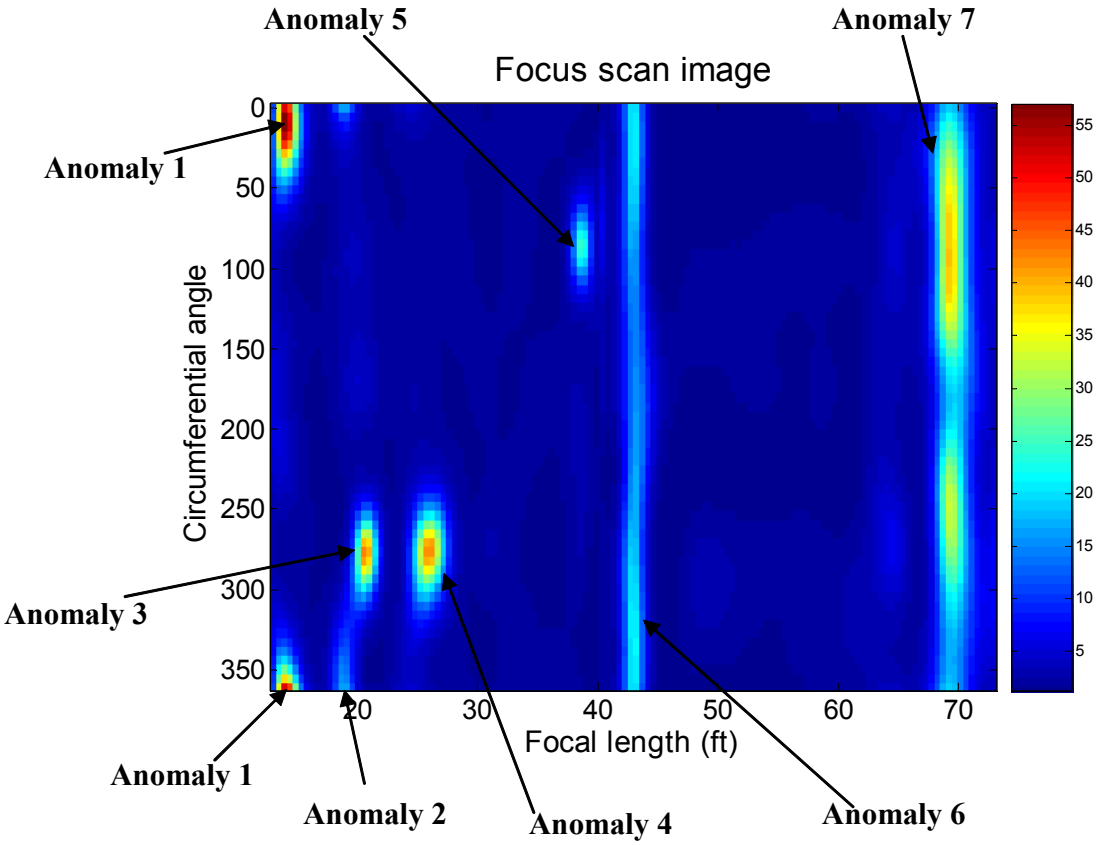

Figure 3-15: Pipe focus scan image. (See Table 3-2.)

The focus scan image of the pipe is quite clear as shown in Figure 3-15. Several anomalies are shown and marked in the pipe image. A summary of the axial and circumferential locations of these anomalies, as well as their types, are given in Table 3-2. From the focus scan image, it is clear that anomalies 1, 2, and 5 are defects. Notice that anomalies 3 and 4 are actually one single defect. The reason is that after the transducer array receives the echo from a defect, the echo will continue to propagate till the end of the pipe, where the echo is reflected and received by the transducer array again. Sometimes this reverberation can be very large, as in this case, therefore, there appear to

be two defects instead of one. This reverberation is difficult to eliminate completely. However, by inspecting the pipe from the other end, the echo caused by reverberation will change its axial location accordingly. In this way, the real location of the defect is revealed. Anomaly 6 is a weld due to its relatively uniform distribution in the circumferential direction as we discussed earlier. Anomaly 7 are spacers because of their large and nonuniform reflections around the circumference.

Table 3-2: Anomaly location summary

Anomaly index	**Axial position from pipe end 1**	**Circumferential position**	**Anomaly type**
1	13’ 2”	0° (360°)	Defect
2	18’ 4’’	0° (360°)	Defect
3	20’ 2”	270°	Defect
4	N/A	N/A	Reverberation from defect 3
5	38’ 3”	90°	Defect
6	41’ 11”	All angles	Weld
7	71’ 8”	Multiple angles	Spacers

Chapter 4

Focusing application in defect circumferential sizing

4.1 Introduction

Guided waves for pipe inspection have been widely used for over ten years. Guided waves can propagate long distances and are excellent in screening and defect location analysis. The state-of-the-art of guided wave utilization on defect sizing is limited. An excellent result for 2D defects in a plate has already been obtained [Zhao 2003]. Similar results are also expected in pipes. However, defect sizing in pipes is more complicated due to the complicity of guided waves in pipe. The focusing technique developed by Li and Rose [2002] is used to increase the detection potential and to achieve a sizing possibility.

In this section, guided wave experiments are carried out to analyze defect circumferential length. It is shown that three differently shaped defects (planar saw cuts, a volumetric through-wall hole, and a volumetric elliptical corrosion) can be effectively detected by using guided wave focusing techniques in pipe. The axial locations of the different defects are accurately measured by calculating the arrival time of the defect echoes in the A-scan results. In order to estimate defect circumferential length, the phased array focusing system [Li 2001, 2002] is utilized to focus on 44 circumferential positions (instead of 4 or 8 positions) around the pipe at a specific axial distance (defect location). This is called a circumferential scan. The pulse echo waveform for each

focused position in one circumferential scan is then recorded. Since there is a focal zone in axial direction, it is shown that multiple defects lying within this focal zone can be detected in one circumferential scan.

Consequently, a time gate is set according to the focal zone in each circumferential scan. The maximum amplitude in the gate in each of these waveforms is plotted with respect to the circumferential focused position in producing an angular profile of the reflected wave. This produced an experimental circumferential profile. The maximum amplitude of this experimental circumferential profile occurs at the angle of the defect circumferential location. The profile, which contains the amplitudes of reflections from 44 circumferential positions, was further used to study the defect's circumferential length.

The reflected energy from a defect was considered to be proportional to the energy impinged onto that defect, although this really depends on defect shape and characterization, a subject for another day. For each focused position, the energy impinged onto and reflected from defects of different circumferential lengths was calculated through the focused angular profile, which was obtained through the Normal Mode Expansion (NME) computational technique [Ditri 1992]. In this way, the reflected energy was able to be plotted with respect to the circumferential focused position. This gave us a theoretical energy reflection profile. The theoretical profiles for defects of different circumferential lengths were then compared with the experimental pulse echo profiles. Thus, the circumferential size of the defect could be measured.

The defects are listed in Table 4-1. Their shapes and corresponding circumferential locations are also illustrated in Figure 4-1. Ultrasonic energy was focused

at z1=10’-11’’, z2=15’-5’’ and z3=19’-3’’ by controlling input time delays and amplitudes for the 4 excitation channels, where z1, z2, and z3 are distances from the phased array transducer. The frequency of the ultrasonic guided waves considered in the study varied over 30 kHz to 45 kHz.

Table 4-1: Descriptions of the defects used in the study

Defect Type	Position from transducer	Circumferential position (CW)	Depth	Circumferential length	Axial length	Defect Type
Corrosion 1	131in. (10’11’’)	0°	90%	2.51in. (18°)	3.66in.	Corrosion 1
Through-wall hole	185in. (15’5’’)	220°	100%	0.5in.	0.5in.	Through-wall hole
Saw cut 1	231in. (19’3’’)	90°	73% (7mm)	119mm, 4.69in. (33.6°)	0.1in.	Saw cut 1
Saw cut 2	231in. (19’3’’)	90°	73% (7mm)	239mm, 9.4in. (66°)	0.1in.	Saw cut 2
Saw cut 3	231in. (19’3’’)	90°	73% (7mm)	(93°)	0.1in.	Saw cut 3
Saw cut 4	231in. (19’3’’)	90°	73% (7mm)	(123°)	0.1in.	Saw cut 4

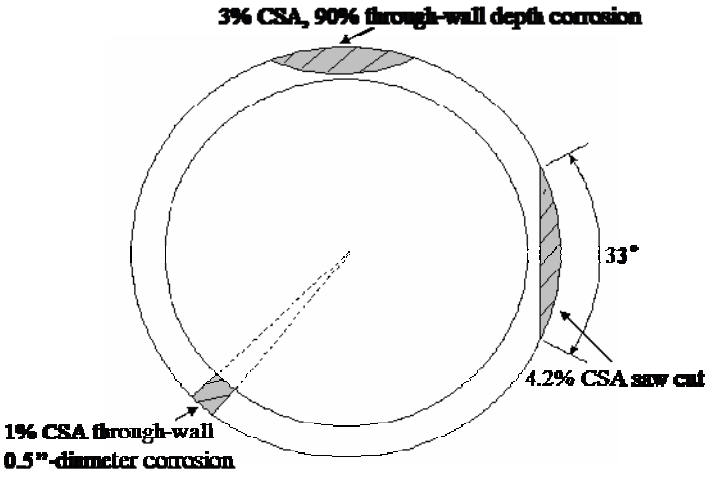

Figure 4-1: The circumferential distributions of the defects in a 16 in. schedule 30 steel pipe.

4.2 Defect detection and axial location

An A-scan pulse echo waveform for corrosion detection is shown in Figure 4-2(a). The torsional wave group T(n,1) at a frequency of 30 kHz was used to achieve focusing at 131in. axial distance. The maximum defect echo as marked in Figure 4-2(a) is obtained when the phased array was focused at 0˚. The arrival time of the echo is about t=2100 μs and the velocity of the torsional wave group can be estimated as c=3.23 mm/μs in steel pipe. So the axial distance of the defect can be calculated by $t \times c / 2 \approx 133$ in. According to Table 4-1, this is where the corrosion is located. The corrosion was introduced by spherical indentation with randomly distributed machine simulated pits. A photo of the corrosion is given in Figure 4-2(b). The axial locations of the through-wall hole and the saw cuts were obtained similarly as shown in Figure 4-4. It was revealed that the axial distance of the different defects in the pipe could be measured quite accurately by using the guided wave focusing technique.

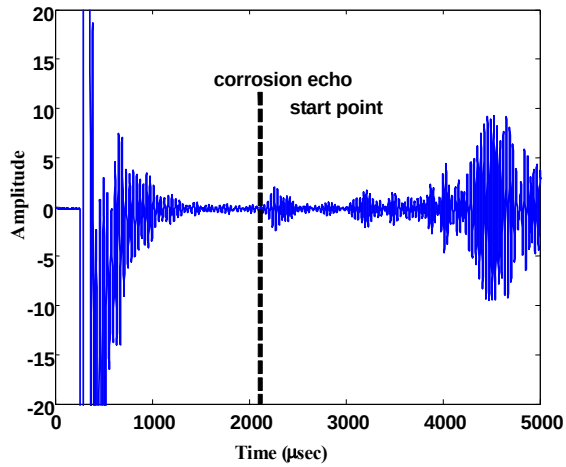

(a) (b)

Figure 4-2: (a). Sample waveform response when focusing with a 30 kHz T(m,1) wave group at the corrosion defect location of 131 in. 0˚ with a 4-channel phased array. (b). Photo of corrosion simulation

4.3 Locating Multiple Defects in One Circumferential Scan

When ultrasonic guided wave energy is focused at a particular axial position, there is a focal zone, over which the energy is always focused at a predetermined circumferential location. For example, when we focus at 220˚ at the distance z=15'-5'' using the T(m,1) wave group at 35 kHz, the ultrasonic energy is focused at 220˚ over the axial range: 11'-2''~19'-6''. If there are multiple defects located in this axial region, they can be detected in one circumferential scan. The axial distance between the through-wall hole (Figure 4-3(a)) and saw cut 1 (Figure 4-3(b)) is less than the length of the focal zone in a 16 in. pipe. In Figure 4-4, the torsional wave group T(M,1) at 40 kHz was used to focus at the saw cut distance over 44 circumferential locations. It can be seen that the

through-wall hole echo and the saw cut echo show up when guided waves focus on their corresponding circumferential locations. A time gate was set for the received signals and the maximum amplitude within this gate was recorded for each focused circumferential angle. The variation of the maximum signal amplitude in the circumferential direction gives the circumferential locations of the defects located within the focal zone. In this multiple location study, a gate including signals arriving from the 12'-5''~20'-8'' range is set in the circumferential scan. By sweeping the focal point along the circumferential direction, the experimental data obtained clearly showed that two defects are located over this distance range (the simulated corrosion was introduced later): as shown in Figure 4-5 and Figure 4-6 for two different frequencies focusing at the through-wall hole and the saw cut distances respectively. As can be verified in Table 4-1, the through-wall hole and the saw cut circumferential locations were measured very accurately. Hence, by sweeping the circumferential focal position, all defects within the focal zone were correctly located.

(a) (b)

Figure 4-3: (a). Through-wall hole in Table 3-1. (b). Saw cut 1 in Table 3-1.

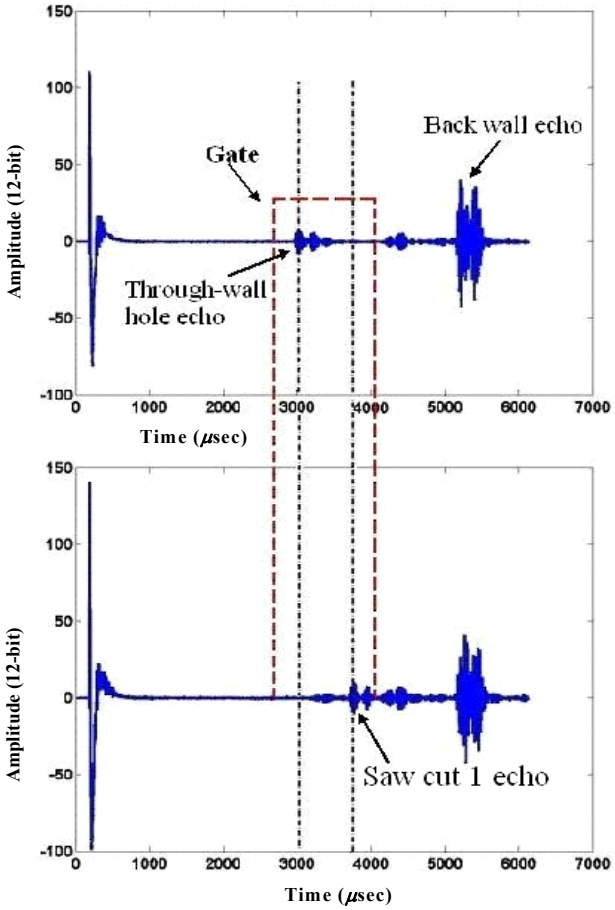

Figure 4-4: Sample waveforms when focusing with the T(m,1) wave group at 40 kHz at 19’3’’ with a 4-channel phased array. An arrival time gate was set to monitor the signals from the range 12’-5’’~20’-8’’. Upper waveform: focus on the angle of the through-wall hole. Lower waveform: focus on saw cut 1.

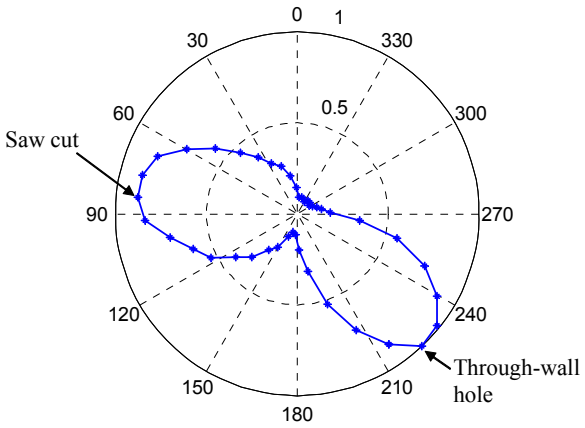

Figure 4-5: Maximum reflected echoes within the distance range: 12’-5’’~20’-8’’. The T(m,1) wave group at 35 kHz was used to focus at 15’-4’’ at 44 different circumferential locations around the pipe. 4-channel phased-array was used. The circumferential length of each excitation channel was 90˚.

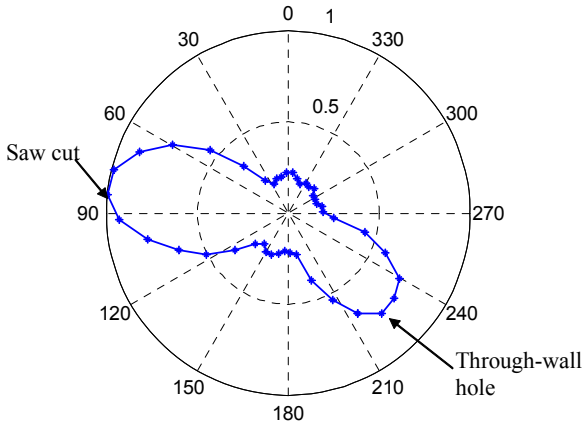

Figure 4-6: Maximum reflected echoes within the distance range: 12’-5’’~20’-8’’. The T(m,1) wave group at 40 kHz was used to focus at 19’-3’’ at 44 different circumferential locations around the pipe. 4-channel phased-array was used. The circumferential length of each excitation channel was 90˚.

4.4 Defect Circumferential Length Analysis

When a 4-channel phased array is used to achieve focusing, the circumferential excitation length of each channel would be approximately 90°. If the focal position is swept along the circumferential direction, the profiles of the energy reflection from a defect versus the focal angle can be obtained theoretically via the focused angular profile by assuming that the defect is almost uniform in depth and considering the defect circumferential span only. Thus, a comparison of the experimental reflection profile and the theoretical energy reflection profiles provides us with the information on the circumferential size of the defect. The focused angular profile at 45 kHz is given in Figure 4-7(a) and the corresponding theoretical energy reflection profiles are given in Figure 4-7(b). It can be seen that the energy reflection profiles depend not only on the size of the defect but also on the shape of the corresponding focused angular profiles. Defect sizing potential is highly related to the resulting focused angular profile and the defect shape as well. A narrower focused angular profile is able to give a better circumferential resolution. Therefore, better sizing can be achieved. Usually, the width of a focused beam is reduced with an increase in the number of the excitation channels. However, the number of the excitation channels cannot be increased infinitely, since more excitation channels usually results in bigger side lobes and subsequent confusion.

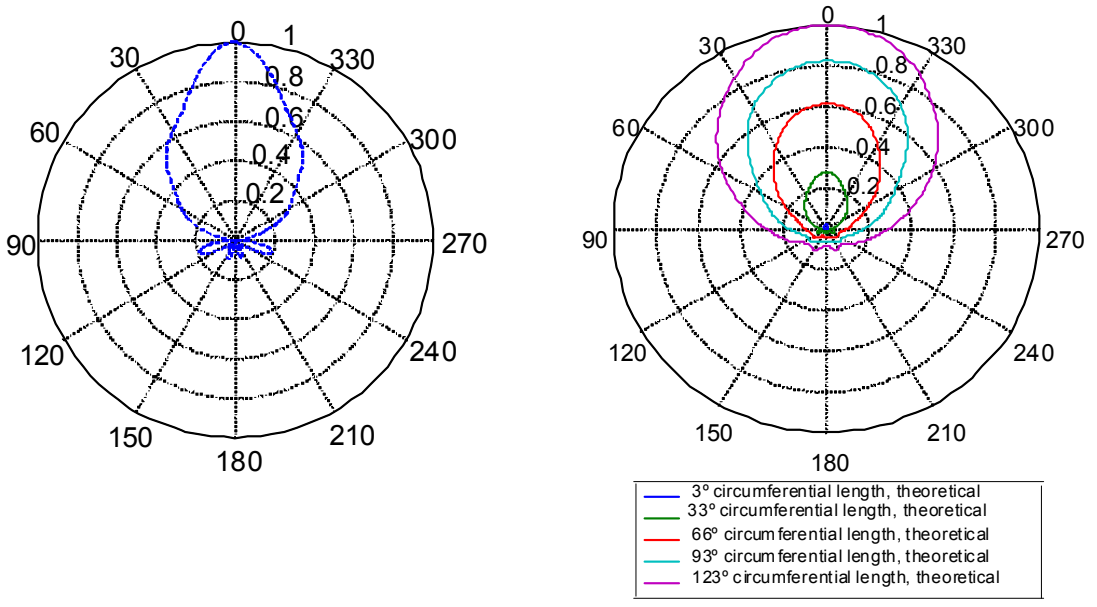

(a) (b)

Figure 4-7: (a). Theoretical focused angular profile of 45kHz focusing at 231in. (saw cut distance). (b). The corresponding theoretical energy reflection profiles for saw cuts with different circumferential sizes.

In this study, by focusing on different positions around the circumferential direction, 44 echoes from a defect can be recorded. The maximum amplitudes of the echoes are plotted versus the focal angles. This experimental reflection profile gave the variation of the reflected energy with respect to the focusing angle. The experimental and theoretical profiles for saw cuts with different circumferential sizes were compared as shown in Figure 4-8(a). Torsional focusing was used. The maximum amplitudes of the theoretical and experimental profiles for the 33º circumferential length were normalized to the same value and the other profiles were also normalized by the same factor. It's shown in Figure 4-8(a) that the profiles for the 66º circumferential length saw cut had larger amplitudes and wider circumferential coverage than that of the 33º circumferential length saw cut. This is obvious, since for a longer saw cut, more energy is reflected and

the 66º circumferential length saw cut can be seen from more focal positions out of the 44 compared than the 33º circumferential length saw cut. The corresponding normalized profiles of Figure 4-8(a) are shown in Figure 4-8(b). It can be seen that the profile broadening of the 66º circumferential length saw cut compared to the 33º one is not as big as the profiles shown in Figure 4-8(a). Normalization minimized the differences between the circumferential extents of the different profiles. However, the normalized theoretical profiles and the normalized experimental profiles still match very well as shown in Figure 4-8(b). A fairly good estimation of the circumferential size of a transverse crack can be made based on Figure 4-8(a) and (b). Note the slight irregularity on the right side of the experimental lobes in both Figure 4-8(a) and (b). This is because the experiments in Figure 4-8(a) and (b) were performed after the corrosion was introduced, and the corrosion lies between the transducer and the saw cut and is located on the right side of the saw cut (please refer to Table 4-1 to get the relative locations of the saw cut and the corrosion). All of the other experiments were done before the corrosion was introduced, so they do not have this problem. These results also revealed the exciting fact that guided wave focusing can be successfully achieved beyond defects and reasonably good circumferential sizing can still be obtained.

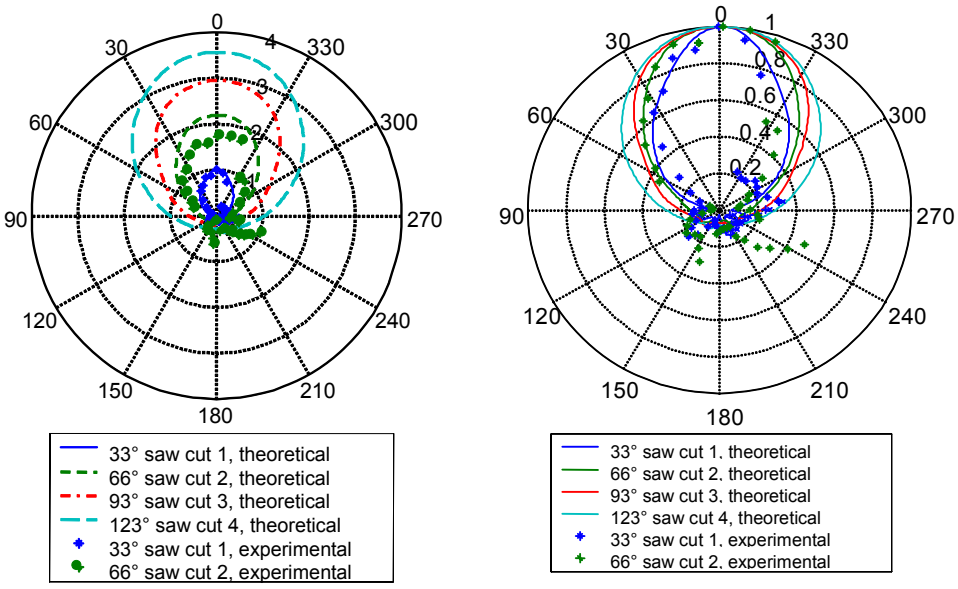

(a) (b)

Figure 4-8: (a). Comparison between theoretical and experimental profiles. The experimental profiles were obtained by applying 4-channel phased-array focusing. The T(m,1) wave group at 45 kHz was focused on 44 different circumferential locations at 231 in. (b). The experimental profiles of the defect echoes for saw cuts with different circumferential sizes are compared with the theoretical energy impingement profiles after normalization.

The experimental and theoretical profiles of the through-wall hole using torsional focusing were compared after normalization in Figure 4-9. It can be seen that the circumferential extent of the through-wall hole can be accurately determined by this technique.

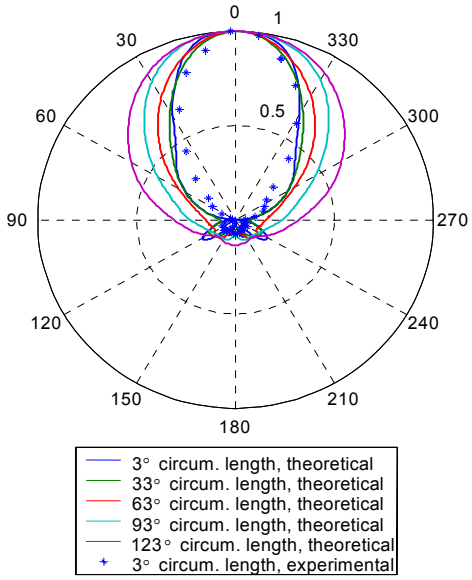

Figure 4-9: Comparison between normalized theoretical and experimental profiles of a through-wall hole. The torsional T(m,1) wave group at 35 kHz was focused on 44 different circumferential locations at 185 in.

Volumetric types of defects are more difficult to detect and characterize, since they scatter waves more severely than planar defects do. Therefore, it is more difficult to obtain good experimental reflection profiles for corrosion. By focusing both longitudinal and torsional wave groups on corrosion, it is revealed that corrosion reflects longitudinal waves more than torsional waves given roughly the same focusing energy. This implies that longitudinal waves are more sensitive to corrosion. The theoretical and experimental profiles of corrosion with 18° circumferential length are compared in Figure 4-10(a)and Figure 4-10(b) for both torsional and longitudinal focusing respectively. It can be seen that reasonably good circumferential measurements are obtained for both torsional and longitudinal focusing.

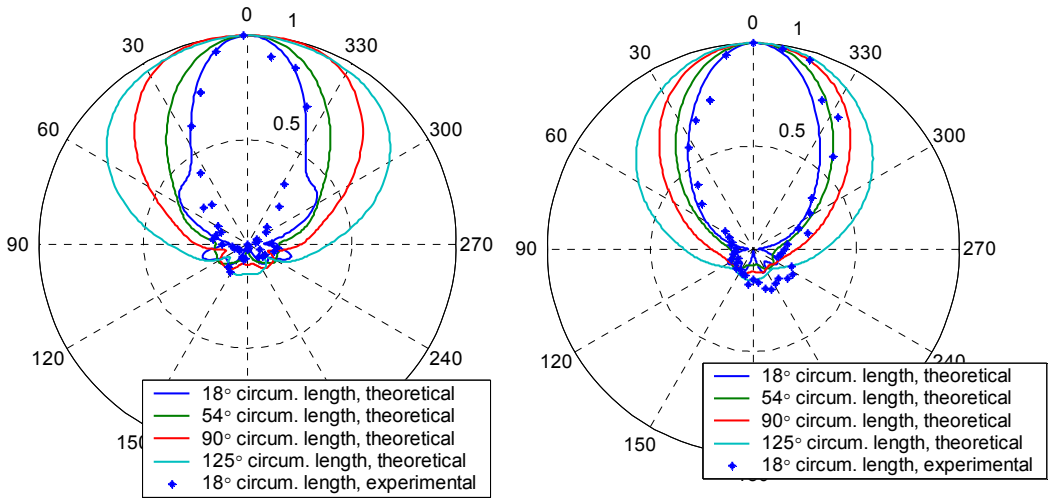

(a) (b)

Figure 4-10: (a). Comparison between normalized theoretical and experimental profiles. The torsional T(m,1) wave group at 35 kHz was focused on 44 different circumferential locations at 131 in. (b). Comparison between normalized theoretical and experimental profiles. The longitudinal L(m,2) wave group at 45 kHz was focused on 44 different circumferential locations at 131 in.

As a result of this study, it is shown that the circumferential lengths of different kinds of defects can be effectively determined by comparing the experimental profile with the theoretical ones. Further comparisons among theoretical profiles of different types of defects reveal the fact that the theoretical profiles of the different defects at the same axial distance are very similar. This is good because it means that defect circumferential size can be determined without knowing any other characteristics of the defect. Therefore, circumferential sizing should be done as the first step in defect characterization. Also, only the peak values of the reflected defect echoes are used in the above circumferential sizing technique. Other defect echo characteristics will help further studies on shape determination. The inverse problem will then be considered.

4.5 Summary

In this study, a long range ultrasonic guided wave test system was used to detect and locate defects as well as to measure the circumferential size of a through-wall hole, transverse saw cuts, and corrsoion by sweeping the focal position around the pipe. The circumferential location was determined very accurately for all of the defects. Multiple defect locations can be achieved in one circumferential scan due to the natural properties of the focused beam. Circumferential length measurements can be obtained by comparing the experimental defect reflection profiles with the theoretical energy reflection profiles. Experiments have shown that this is an effective way to measure the circumferential length of defects and it gives us a very good estimation on different types of defects. However, since only 4 and 8 channels were used to focus, the resulting focused angular profile is relatively wide. This makes it difficult to tell the difference of circumferential lengths below 30°. A narrower focal beam could make circumferential sizing more accurate. It can be achieved by using more channels to focus. Both the shape of a defect and the shape of the angular profile influence the predicted sizing results. Angular profiles with large side lobes must be avoided.

Chapter 5

Guided wave propagation in multilayered hollow cylinders with viscoelastic materials

5.1 Introduction

The work on wave propagation in bounded structures by [Lamb 1917] and [Rayleigh 1945], etc. in early last century sparked the beginning of research on guided wave theories. Ever since then, it has been recognized that there exists many more wave modes in free wave guide structures than those in a bulk medium [Graff 1991; Rose 1999]. These guided wave modes are in general much more complex than bulk waves, since they have to satisfy the boundary conditions of the wave guides. Around the 1950's, accompanied with the rapid development of modern computers, there emerged a massive amount of research on guided wave dispersion curve computations on multilayered structures. The two computational methods that have been widely used till now are the transfer matrix approach developed by [Thomson 1950] and the global matrix method by [Knopoff 1964]. Generally speaking, the global matrix method is more stable computational wise than the transfer matrix technique. A good summary of the matrix techniques can be found in [Lowe 1995]. An important part of these matrix techniques is that a root searching routine has to be established in order to find the roots of the determinant associated with the set of homogeneous equations obtained by satisfying boundary conditions in the wave number and frequency domain. If there is viscoelastic material in the wave guide structure, then the root searching process has to be performed

on both real and imaginary wave number domains for each frequency. This 3-dimensional root searching process can be very difficult and time-consuming. In addition, when the frequency gets higher or matrix size becomes larger due to an increase in the number of layers in the structure, roots are likely to be missed in the searching process.

Gazis [1959] obtained the complete solution for harmonic guided wave modes propagating in an infinite hollow cylinder. This has been very beneficial for long range guided wave inspection on pipelines. In practice, however, most of the pipelines used in industry are covered with viscoelastic coatings for various protection purposes. Waves sent to the pipe will partially leak into the coating leading to a different wave field from that of a bare pipe. The wave fields in a coated pipe will be different from that of a corresponding bare pipe. As a result, bare pipe focusing parameters may not be valid for coated pipes. Therefore, the exploration of guided wave propagation in viscoelastic coated hollow cylinders becomes quite indispensable.

Due to the afore mentioned computation difficulties encountered in matrix methods, theoretical calculation of the wave modes in hollow cylinders with viscoelatic coatings is very difficult. Some researchers have studied plate or plate-like structures with viscoelastic properties, for example, [Simonetti 2004] and [Predoi, et al., 2007]. These plate solutions may be safely used to approximate hollow cylinders with thickness to radius ratio less than 10% [Luo, et al., 2005]. Therefore, it is still valuable to search for a complete solution to wave propagation in multilayered viscoelastic cylinders. The axisymmetric wave modes of such a structure have been provided by Barshinger, et al., [2004] using the global matrix method, but he did not provide the flexural modes in his paper. Ma, et al. [2006] investigated the fundamental torsional mode scattering from an

axisymmetric sludge layer inside a pipe. In his study, the sludge layer is considered to be an elastic epoxy layer. Beard and Lowe [2003] used guided waves to inspect the integrity of rock bolts. They provided 3 lower order (circumferential order equals 1) flexural modes in their study at relatively low frequency range (less than 300 kHz). To the author's best knowledge, such a complete solution including both axisymmetric and non-axisymmetric modes (flexural modes with circumferential orders equal or larger than one) in multilayered hollow cylindrical structures covering a relative wide frequency range (up to mega Hertz) has never been reported in the literature before. Our goal in this chapter is to understand and seek the complete solution to this problem using appropriate techniques.

The Semi-Analytical Finite Element Method (SAFEM) was developed as an alternative way to solve wave propagation problems. In the SAFEM, the wave guide is discretized in the cross section, while an analytical solution is adopted in the wave propagation direction. In this way, the SAFEM is able to solve problems of wave propagation in wave guides with complex cross sections, for example, rails and multilayered cylinders, where it might be difficult to obtain analytical solutions. It is also superior to pure FEM since exact analytical representations are used for one or two dimensions of the wave guide. In this way, computational cost is reduced. In the mean time, the characteristic wave modes that can propagate in a waveguide can still be obtained. Early employment of SAFEM in solving guided wave propagation problems can be found in [Nelson, et al., 1971] and [Dong, et al., 1972]. In recent years, SAFEM was also applied to the analysis of wave modes across a pipe elbow [Hayashi, et al., 2005] and in materials with viscoelastic properties [Shorter, 2004; Bartoli, et al., 2006].

SAFEM is adopted here to generate phase velocity and attenuation dispersion curves including both axisymmetric and flexural modes in hollow cylinders with viscoelastic coatings. Modal characteristics such as wave structures and attenuation properties are provided and discussed. Furthermore, driven by the fact that the wave modes obtained from SAFE calculations are difficult to differentiate from each other, a mode sorting algorithm based on modal orthogonality is developed. An orthogonality relation based upon the SAFE formulation for elastic wave guides is developed by [Damljanović, et al., 2004]. Different from Damljanović, the orthogonality relation derived in this study is valid for both elastic and viscoelastic materials. It can be used in either single-layered or multilayered cylindrical structures. It is applicable not only for dispersion curve calculations by SAFE formulations but also for those obtained from analytical derivations.

5.2 SAFE formulation

Let us start with the governing equation provided by the virtual work principle for a stress free hollow cylinder as in [Hayashi 2003, Sun 2004]. Only linear elastic and viscoelastic material behaviors are considered here.

$$\int_V \delta\mathbf{u}^T \cdot \rho\ddot{\mathbf{u}} dV + \int_V \delta\boldsymbol{\varepsilon}^T \cdot \boldsymbol{\sigma} dV = 0, \qquad 5.1$$

where T represents matrix transpose, ρ is density and $\ddot{\mathbf{u}}$ is the second derivative of displacement $\mathbf{u}$ with respect to time t. $\int_\Gamma d\Gamma$ and $\int_V dV$ are the surface and volume

integrals of the element respectively. In cylindrical coordinates, $dV = rdrd\theta dz$. The first and second terms on the left-hand side are the corresponding increment of kinetic energy and potential energy.

Sun [2004] used 2-D SAFE to calculate the flexural modes in a single elastic cylinder. He meshed the cross section of the cylinder in both the thickness direction r and circumferential direction θ. Due to the fact that he used finite elements to represent the circumferential direction θ, the flexural mode of the highest circumferential order he could obtain in his dispersion curve is limited by the number of elements in the circumferential direction divided by 2. As a result, for calculating dispersion curves of higher circumferential orders, more elements have to be considered in the circumferential direction, which results in an increase in matrix size and computational cost. In order to overcome this limitation and also to save computational cost, we adopted an exact analytical solution $e^{in\theta}$ in the circumferential direction. In this way, the exact representations are used in both the θ and z directions. The finite element approximation reduces to only one dimension r. This 1-D SAFE formulation does not only improve the accuracy in our calculation for flexural modes with higher circumferential orders, but also greatly reduces the computational cost compared to 2-D SAFE. For a harmonic wave propagating in the z direction, the displacement at any point $\mathbf{u}(r,\theta,z,t)$ can be represented by

$$\mathbf{u}(r,\theta,z,t) = \sum_{j=1}^{2} \mathbf{N}(r)\mathbf{U}^{j} e^{i(kz+n\theta-\omega t)}, \qquad 5.2$$

where $\mathbf{U}^j$ is the nodal displacement vector at the j^{th} element and $\mathbf{N}(r)$ is the shape function in the thickness direction r. For a 2 node element, $\mathbf{U}^j$ is a 6 element vector and $\mathbf{N}(r)$ is a 3×6 matrix. The shape function matrix is chosen as follows,

$$\mathbf{N} = \begin{bmatrix} N_1 & 0 & 0 & N_2 & 0 & 0 \\ 0 & N_1 & 0 & 0 & N_2 & 0 \\ 0 & 0 & N_1 & 0 & 0 & N_2 \end{bmatrix}, \tag{5.3}$$

using linear shape functions

$$\begin{aligned} N_1 &= \frac{1}{2}(1-\xi), \\ N_2 &= \frac{1}{2}(1+\xi), \end{aligned} \tag{5.4}$$

where $-1 \le \xi \le 1$ is the natural coordinate in the r direction. The strain-displacement relations are

$$\begin{aligned} \varepsilon_{rr} &= \frac{\partial u_r}{\partial r} \\ \varepsilon_{\theta\theta} &= \frac{u_r}{r} + \frac{1}{r}\frac{\partial u_\theta}{\partial \theta} \\ \varepsilon_{zz} &= \frac{\partial u_z}{\partial z} \\ \gamma_{\theta z} &= \frac{1}{r}\frac{\partial u_z}{\partial \theta} + \frac{\partial u_\theta}{\partial z} \\ \gamma_{rz} &= \frac{\partial u_r}{\partial z} + \frac{\partial u_z}{\partial r} \\ \gamma_{r\theta} &= \frac{1}{r}\frac{\partial u_r}{\partial \theta} + \frac{\partial u_\theta}{\partial r} - \frac{u_\theta}{r} \end{aligned} \tag{5.5}$$

Substituting Eq. 5.2 to Eq. 5.4 into the strain-displacement relationship Eq. 5.5, the six strain components can be express as

$$\begin{aligned}\boldsymbol{\varepsilon} &= (\mathbf{L}_1 + \mathbf{L}_2)\mathbf{u} \\ &= (\mathbf{L}_1 + \mathbf{L}_2)\mathbf{N}\mathbf{U}^j e^{i(kz+n\theta-\omega t)} \\ &= \left(\mathbf{B}_1 + ik\mathbf{B}_2\right)\mathbf{U}^j e^{i(kz+n\theta-\omega t)}\end{aligned}, \qquad 5.6$$

where

$$\mathbf{L}_1 = \begin{bmatrix} \frac{\partial}{\partial r} & 0 & 0 \\ \frac{1}{r} & \frac{1}{r}\frac{\partial}{\partial \theta} & 0 \\ 0 & 0 & 0 \\ 0 & 0 & \frac{1}{r}\frac{\partial}{\partial \theta} \\ 0 & 0 & \frac{\partial}{\partial r} \\ \frac{1}{r}\frac{\partial}{\partial \theta} & \frac{\partial}{\partial r} - \frac{1}{r} & 0 \end{bmatrix}, \qquad 5.7$$

$$\mathbf{L}_2 = \begin{bmatrix} 0 & 0 & 0 \\ 0 & 0 & 0 \\ 0 & 0 & \frac{\partial}{\partial z} \\ 0 & \frac{\partial}{\partial z} & 0 \\ \frac{\partial}{\partial z} & 0 & 0 \\ 0 & 0 & 0 \end{bmatrix} \qquad 5.8$$

$$\mathbf{B}_1 = \begin{bmatrix} \frac{\partial N_1}{\partial r} & 0 & 0 & \frac{\partial N_2}{\partial r} & 0 & 0 \\ \frac{N_1}{r} & i\frac{n}{r}N_1 & 0 & \frac{N_2}{r} & i\frac{n}{r}N_2 & 0 \\ 0 & 0 & 0 & 0 & 0 & 0 \\ 0 & 0 & i\frac{n}{r}N_1 & 0 & 0 & i\frac{n}{r}N_2 \\ 0 & 0 & \frac{\partial N_1}{\partial r} & 0 & 0 & \frac{\partial N_2}{\partial r} \\ i\frac{n}{r}N_1 & \frac{\partial N_1}{\partial r} - \frac{N_1}{r} & 0 & i\frac{n}{r}N_2 & \frac{\partial N_2}{\partial r} - \frac{N_2}{r} & 0 \end{bmatrix}_{6\times 6}, \qquad 5.9$$

$$\mathbf{B}_2 = \begin{bmatrix} 0 & 0 & 0 & 0 & 0 & 0 \\ 0 & 0 & 0 & 0 & 0 & 0 \\ 0 & 0 & N_1 & 0 & 0 & N_2 \\ 0 & N_1 & 0 & 0 & N_2 & 0 \\ N_1 & 0 & 0 & N_2 & 0 & 0 \\ 0 & 0 & 0 & 0 & 0 & 0 \end{bmatrix}_{6\times 6}. \qquad 5.10$$

Substituting the strain components obtained in Eq. 5.6 into the constitutive relation for strain and stress yields the expression for stress components.

$$\boldsymbol{\sigma} = \mathbf{C}\boldsymbol{\varepsilon} = \mathbf{C}\left(\mathbf{B}_1 + ik\mathbf{B}_2\right)\mathbf{U}^j e^{i(kz+n\theta-\omega t)}, \qquad 5.11$$

where **C** is the stiffness matrix. The values in the matrix **C** are real for elastic materials and complex for viscoelastic materials according to the correspondence principle [Christensen 1982].

Substituting the displacements Eq. 5.2, strains Eq. 5.6, stresses Eq. 5.11 into the governing equation Eq. 5.1, one obtains Eq. 5.12 for element j after simplification.

$$\left(\mathbf{K}_1{}^j + ik\mathbf{K}_2{}^j + k^2\mathbf{K}_3{}^j\right)\mathbf{U}^j - \omega^2\mathbf{M}^j\mathbf{U}^j = 0 \qquad 5.12$$

where

$$\begin{aligned} \mathbf{K}_1{}^j &= \int_r\int_\theta \mathbf{B}_1{}^T\mathbf{C}\mathbf{B}_1 r dr d\theta, \\ \mathbf{K}_2{}^j &= \int_r\int_\theta \left(\mathbf{B}_1{}^T\mathbf{C}\mathbf{B}_2 - \mathbf{B}_2{}^T\mathbf{C}\mathbf{B}_1\right) r dr d\theta, \\ \mathbf{K}_3{}^j &= \int_r\int_\theta \mathbf{B}_2{}^T\mathbf{C}\mathbf{B}_2 r dr d\theta, \\ \mathbf{M}^j &= \rho\int_r\int_\theta \mathbf{N}^T\mathbf{N} r dr d\theta. \end{aligned} \qquad 5.13$$

Assembling Eq. 5.12 for all elements in the *r* direction, the equation for the whole system can be written as

$$\left(\mathbf{K}_1 + ik\mathbf{K}_2 + k^2\mathbf{K}_3\right)\mathbf{U} - \omega^2\mathbf{M}\mathbf{U} = 0 \qquad 5.14$$

where $\mathbf{K}_1$, $\mathbf{K}_2$, $\mathbf{K}_3$, and $\mathbf{M}$ are the $M \times M$ matrices where M is three times the number of nodes. Before solving this eigenvalue problem for k, the order of k in Eq. 5.14 can be further reduced by the following manipulation

$$\left[\mathbf{A} - k\mathbf{B}\right]\mathbf{Q} = 0\,, \qquad 5.15$$

where

$$\begin{aligned}
\mathbf{A} &= \begin{bmatrix} 0 & \mathbf{K}_1 - \omega^2\mathbf{M} \\ \mathbf{K}_1 - \omega^2\mathbf{M} & i\mathbf{K}_2 \end{bmatrix}, \\
\mathbf{B} &= \begin{bmatrix} \mathbf{K}_1 - \omega^2\mathbf{M} & 0 \\ 0 & -\mathbf{K}_3 \end{bmatrix}, \qquad 5.16 \\
\mathbf{Q} &= \begin{bmatrix} \mathbf{U} \\ k\mathbf{U} \end{bmatrix}.
\end{aligned}$$

At any given frequency ω, the the wave number *k* can be obtained by solving the eigenvalue problem in Eq. 5.15 using a standard eigenvalue routine. Then, the phase velocity and attenuation dispersion curves can be calculated from the real part and imaginary part of *k*. The corresponding wave structure **U** is obtained from the upper half of the eigenvector **Q**, as can be seen from Eq. 5.16.

5.3 Orthogonality and mode sorting

A common difficulty in producing dispersion curves calculated from the SAFE formulation is modal differentiation. The order of the guided wave modes obtained by solving Eq. 5.15 can be different for different frequencies. In producing dispersion curves, a starting frequency f_{start}, an ending frequency f_{end}, and a frequency step Δf are first chosen. The selected frequency f varies from f_{start} to f_{end} at an increment of Δf. If the order of the wave modes obtained at each frequency f is different, the resulting dispersion curves are difficult to be plotted by lines. Most dispersion curves provided in previous SAFE studies are plotted by dots [for example, Sun 2004; Hayashi, et al., 2003]. Modal differentiation is tremendously helpful for us to track the behavior of a certain mode with respect to frequency change. It also forms the basis of thinking critically and conceptually for problems like wave scattering and source influence. In previous analytical matrix techniques, mode tracking is usually achieved by performing extrapolation (also called curve tracing) during root searching. In the curve tracing process, the value of a dispersion curve at a new frequency is first predicted by extrapolation based on its previous values. Then, the root searching is conducted in the neighborhood of the predicted value. A detailed discussion can be found in [Lowe 1995]. Conducting extrapolation saves time in dispersion curve root searching. It also provides the possibility of tracing a specific mode. The drawback of this extrapolation technique is that it is not robust. Extrapolation makes the curve tracing sensitive to the changes in the previous values. In analytical matrix approaches, roots can be missing during root searching. If one or two roots are missing at the previous frequencies, the curve tracing

can fail. Most importantly, different guided wave modes can cross each other in the dispersion curves. It is difficult to predict the cross modes accurate enough simply by extrapolation and curve fitting.

Of particular importance in mode sorting is to find the distinctive characteristics between different modes. A natural way of accomplishing this goal is to utilize the modal orthogonality. Damljanović, et al., [2004] presented an orthogonality relation based on SAFE formulation for elastic waveguides and used it to solve a point source loading problem. Loveday, et al., [2007] also employed this relation to sort the guided wave modes in a rail. Another way of sorting wave modes can be realized by identifying the similarity between wave modes at adjacent frequencies, which will be discussed in detail later. Here, we prefer using orthogonality not only due to the fact that orthogonality is a natural attribute of guided wave modes but also because orthogonality can be used in our future research of wave scattering and source influence in multilayered cylinders.

The analytical orthogonality relations have been studied and used by researchers for decades. The orthogonality relation for the Rayleigh-Lamb modes of a 2-dimensional plate was obtained by Fraser [1976]. Later, orthogonality relations of guided wave modes have been used as a powerful tool in the study of wave scattering [Kino, 1978; Engan, 1998; Shkerdin, et al., 2004, 2005; Vogt, et al., 2003] and source influence [Ditri 1992, 1994b] analysis. In these studies, orthogonality relations are derived from either real or complex reciprocity relations. As has been pointed out by Auld [1990], both real and complex reciprocity relations are valid for elastic wave guides. However, only the real reciprocity relation is valid for viscoelastic materials. If we set out from the real reciprocity relation, we will reach an orthogonality relation stating that the mode is

orthogonal to all the other modes except a mode with the same modal behavior but incoming from the opposite propagating direction, which is the case in this paper. On the other hand, starting out from the complex reciprocity relation yields an orthogonality relation stating that the mode is orthogonal to all the other modes except itself. Like the two reciprocity relations, these two orthogonalities are both valid for elastic wave guides. Likewise, to obtain an orthogonality relation that is applicable for viscoelastic wave guides, it is necessary to start out from the real reciprocity relation. Although there exist a general 'form' of the orthogonality relation [Auld 1990], the utilization of orthogonality relations is associated with guided wave modes and, therefore, is dependent on wave guide geometries. The previous orthogonality relations for 3-dimensional solid cylinders and hollow cylinders have been provided by Vogt, et al., [2003], Engan [1998], and Ditri [1992] by using the stress free boundary conditions under cylindrical coordinates. Here, for a multilayered viscoelastic cylinder, we prove that the orthogonality relation is still valid by taking into account both the interface continuity conditions and stress free boundary conditions.

In this section, the analytical derivation of orthogonality of the modes in multilayered cylindrical structures containing both elastic and viscoelastic materials will be given. Different from the orthogonality relation developed in [Damljanović et al., 2004], the orthogonality developed in this paper can be applied to multilayered wave guides containing any combination of elastic and viscoelastic materials. In addition, since the following orthogonality relation is derived analytically, it can be applied to dispersion curves obtained from either the SAFE formulation or from the matrix methods. In the following, the mode sorting process will be discussed accordingly.

The orthogonality of normal modes in an elastic hollow cylinder was first developed by [Ditri, et al., 1992]. Different from the complex reciprocity relation used in the paper, we start with the real reciprocity relation, which is valid for both elastic and viscoelastic materials (Auld 1990)

$$\nabla \cdot (\mathbf{v}_1 \cdot \mathbf{T}_2 - \mathbf{v}_2 \cdot \mathbf{T}_1) = 0 \tag{5.17}$$

where $\mathbf{v}_1$, $\mathbf{v}_2$ and $\mathbf{T}_1$, $\mathbf{T}_2$ are the particle velocities and stresses for two different wave modes (either torsional or longitudinal type) in a multilayered hollow cylinder. Without loss of generality, $\mathbf{v}_1$, $\mathbf{v}_2$ and $\mathbf{T}_1$, $\mathbf{T}_2$ can be represented as

$$\begin{aligned} \mathbf{v}_1 &= \mathbf{v}_m^N e^{-i\beta_m^N z}, \\ \mathbf{T}_1 &= \mathbf{T}_m^N e^{-i\beta_m^N z}, \\ \mathbf{v}_2 &= \mathbf{v}_n^M e^{-i\beta_n^M z}, \\ \mathbf{T}_2 &= \mathbf{T}_n^M e^{-i\beta_n^M z}, \end{aligned} \tag{5.18}$$

where N and M denote circumferential orders, n and m are indices of mode group, and β denotes the wave number of mode (M, n) or (N, m). So we have

$$\mathbf{v}_1 \cdot \mathbf{T}_2 - \mathbf{v}_2 \cdot \mathbf{T}_1 = (\mathbf{v}_m^N \cdot \mathbf{T}_n^M - \mathbf{v}_n^M \cdot \mathbf{T}_m^N) e^{-i(\beta_m^N + \beta_n^M) z}. \tag{5.19}$$

Substituting Eq. 5.19 into Eq. 5.17 yields

$$\nabla_{r\theta} \cdot (\mathbf{v}_m^N \cdot \mathbf{T}_n^M - \mathbf{v}_n^M \cdot \mathbf{T}_m^N) - i(\beta_m^N + \beta_n^M)(\mathbf{v}_m^N \cdot \mathbf{T}_n^M - \mathbf{v}_n^M \cdot \mathbf{T}_m^N) \cdot \hat{\mathbf{e}}_z = 0. \tag{5.20}$$

where $\nabla_{r\theta}$ is the 2-D divergence operator in cylindrical coordinates.

By integrating both sides of Eq. 5.20 over the cross section D of the viscoelastic coated hollow cylinder, we obtain

$$\iint_D \nabla_{r\theta} \cdot (\mathbf{v}_m^N \cdot \mathbf{T}_n^M - \mathbf{v}_n^M \cdot \mathbf{T}_m^N) d\sigma = -4i(\beta_m^N + \beta_n^M) P_{mn}^{NM}, \qquad 5.21$$

where

$$P_{mn}^{NM} = -\frac{1}{4} \iint_D (\mathbf{v}_m^N \cdot \mathbf{T}_n^M - \mathbf{v}_n^M \cdot \mathbf{T}_m^N) \cdot \hat{\mathbf{e}}_z d\sigma. \qquad 5.22$$

The left hand side of Eq. 5.21 can be written as

$$\begin{aligned} \iint_D \nabla_{r\theta} \cdot (\mathbf{v}_m^N \cdot \mathbf{T}_n^M - \mathbf{v}_n^M \cdot \mathbf{T}_m^N) d\sigma = & \iint_{D_1} \nabla_{r\theta} \cdot (\mathbf{v}_m^N \cdot \mathbf{T}_n^M - \mathbf{v}_n^M \cdot \mathbf{T}_m^N) d\sigma \\ & + \iint_{D_2} \nabla_{r\theta} \cdot (\mathbf{v}_m^N \cdot \mathbf{T}_n^M - \mathbf{v}_n^M \cdot \mathbf{T}_m^N) d\sigma \end{aligned} \qquad 5.23$$

where D_1 and D_2 denote the cross sections of the elastic hollow cylinder and the viscoelastic coating respectively as shown in Figure 5-1.

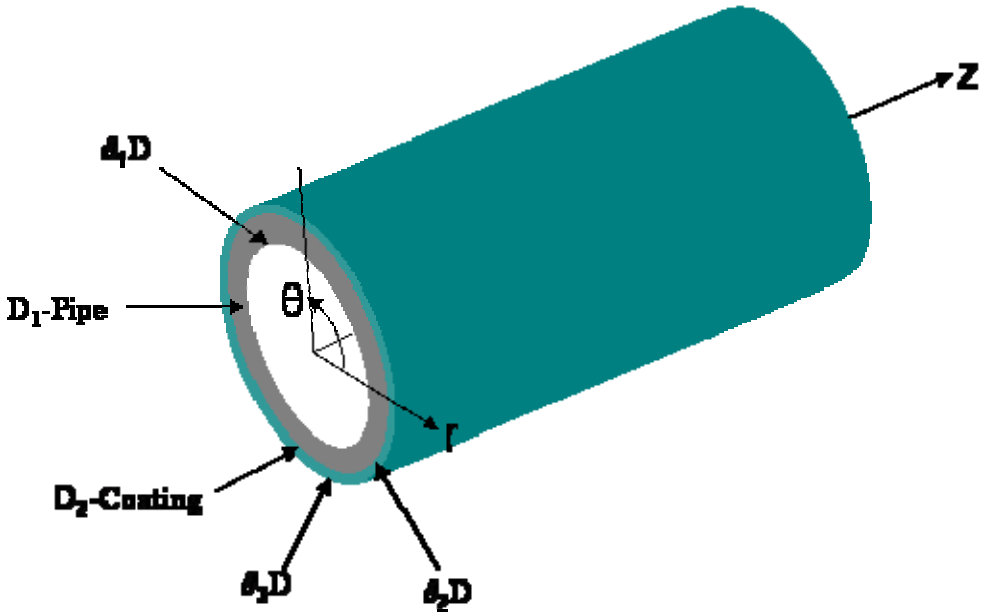

Figure 5-1: Illustration of the cross sections D_1 and D_2, inner boundary $\partial_1 D$, interface $\partial_2 D$, and outer boundary $\partial_3 D$.

Applying the Gauss divergence theorem to the right hand side of Eq. 5.23, we have

$$\begin{aligned}\iint_D \nabla_{r\theta}\cdot(\mathbf{v}_m^N\cdot\mathbf{T}_n^M-\mathbf{v}_n^M\cdot\mathbf{T}_m^N)d\sigma &= \oint_{\partial_1 D}(\mathbf{v}_m^N\cdot\mathbf{T}_n^M-\mathbf{v}_n^M\cdot\mathbf{T}_m^N)\cdot\hat{\mathbf{n}}_1 ds\\ &+\oint_{\partial_2 D}(\mathbf{v}_m^N\cdot\mathbf{T}_n^M-\mathbf{v}_n^M\cdot\mathbf{T}_m^N)\cdot\hat{\mathbf{n}}_2 ds\\ &+\oint_{\partial_2 D}(\mathbf{v}_m^N\cdot\mathbf{T}_n^M-\mathbf{v}_n^M\cdot\mathbf{T}_m^N)\cdot\hat{\mathbf{n}}_1 ds\\ &+\oint_{\partial_3 D}(\mathbf{v}_m^N\cdot\mathbf{T}_n^M-\mathbf{v}_n^M\cdot\mathbf{T}_m^N)\cdot\hat{\mathbf{n}}_2 ds\end{aligned} \qquad 5.24$$

where $\partial_1 D$ represents the inner boundary of D_1, $\partial_2 D$ represents the interface between D_1 and D_2, and $\partial_3 D$ represents the outer boundary of D_2. The unit vectors $\hat{\mathbf{n}}_1$ and $\hat{\mathbf{n}}_2$ are defined as

$$\begin{aligned}\hat{\mathbf{n}}_1 &= -\hat{\mathbf{r}},\\ \hat{\mathbf{n}}_2 &= \hat{\mathbf{r}}.\end{aligned} \qquad 5.25$$

Noting the identities

$$(\mathbf{v}_m^N\cdot\mathbf{T}_n^M-\mathbf{v}_n^M\cdot\mathbf{T}_m^N)\cdot\hat{\mathbf{n}}_1=\mathbf{v}_m^N\cdot(\mathbf{T}_n^M\cdot\hat{\mathbf{n}}_1)-\mathbf{v}_n^M\cdot(\mathbf{T}_m^N\cdot\hat{\mathbf{n}}_1), \qquad 5.26$$

$$(\mathbf{v}_m^N\cdot\mathbf{T}_n^M-\mathbf{v}_n^M\cdot\mathbf{T}_m^N)\cdot\hat{\mathbf{n}}_2=\mathbf{v}_m^N\cdot(\mathbf{T}_n^M\cdot\hat{\mathbf{n}}_2)-\mathbf{v}_n^M\cdot(\mathbf{T}_m^N\cdot\hat{\mathbf{n}}_2), \qquad 5.27$$

and the fact that the displacements and normal stresses are continuous at the interface $\partial_2 D$, by summing up Eq. 5.26 and Eq. 5.27, we simplify Eq. 5.24 to

$$\begin{aligned}\iint_D \nabla_{r\theta}\cdot(\mathbf{v}_m^N\cdot\mathbf{T}_n^M-\mathbf{v}_n^M\cdot\mathbf{T}_m^N)d\sigma &= \oint_{\partial_1 D}(\mathbf{v}_m^N\cdot\mathbf{T}_n^M-\mathbf{v}_n^M\cdot\mathbf{T}_m^N)\cdot\hat{\mathbf{n}}_1 ds\\ &+\oint_{\partial_3 D}(\mathbf{v}_m^N\cdot\mathbf{T}_n^M-\mathbf{v}_n^M\cdot\mathbf{T}_m^N)\cdot\hat{\mathbf{n}}_2 ds\end{aligned}. \qquad 5.28$$

Incorporating the interfacial conditions is important for the development of the orthogonality relation in multilayered structures. This is different from the previous orthogonality development for single layered structures [Ditri, et al., 1992]. Once again,

by applying identities Eq. 5.26 and Eq. 5.27 and by noticing that the tractions produced by the modes (M, n) and (N, m) vanish at the free boundaries of the wave guides, we get

$$\iint_D \nabla_{r\theta} \cdot (\mathbf{v}_m^N \cdot \mathbf{T}_n^M - \mathbf{v}_n^M \cdot \mathbf{T}_m^N) d\sigma = 0 . \qquad 5.29$$

Combining Eq. 5.21 and Eq. 5.29, we finally obtain

$$P_{mn}^{NM} = 0 \text{ for } \beta_m^N \neq -\beta_n^M . \qquad 5.30$$

Direct evaluation of P_{mn}^{NM} using the orthogonality of the angular eigenfunctions cos(Nθ) and sin(Mθ) also shows that

$$P_{mn}^{NM} = 0 \text{ for } M \neq N . \qquad 5.31$$

To summarize, the orthogonality relation in multilayered hollow cylinders containing viscoelastic material is

$$P_{mn}^{NM} = 0 \text{ for } M \neq N \text{ or } \beta_m^N \neq -\beta_n^M . \qquad 5.32$$

From the above analysis, it can be seen that the orthogonality derivation for multilayered viscoelastic hollow cylinders is different from that in an elastic hollow cylinder in two aspects. First, we started from the real reciprocity because only the real reciprocity is valid for viscoelastic materials. Second, we utilized the interfacial displacement and normal stress continuity conditions in order to validate the orthogonality relation in multilayered waveguides. Although the derivation is given for a two layered case, it can be easily generalized to the orthogonality for the N (N>2) layered case.

Once the orthogonality relation is reached, guided modes can be sorted by calculating P_{mn}^{NM} between the modes of adjacent frequencies. For instance, solving Eq. 5.15 yields N_1 modes at frequency ω_1 and N_2 modes at the adjacent frequency ω_2, where $\omega_2 - \omega_1 = \Delta\omega$ is the frequency step. P_{mn}^{NM} is then calculated between each mode at ω_2 and all of the modes at ω_1 using Eq. 5.22 to obtain N_1 results. The biggest value in the N_1 results indicates the two modes used for this orthogonality calculation belonging to the same mode in the dispersion curves. In fact, the other values will be very close to zero. Here, we do not have to know the values of *m*, *n*, and *M*, *N*. We only need to utilize the wave structures obtained from Eq. 5.15 for the two modes under concern, calculate their corresponding stress components, and input these stress and displacement components into Eq. 5.22 to calculate P_{mn}^{NM}. It can be seen from this procedure that the orthogonality computation is performed $N_1 \times N_2$ times for the two adjacent frequencies. Strictly speaking, the orthogonality relation is valid between the modes under any single arbitrary frequency. However, we are performing it between two adjacent frequencies ω_1 and ω_2 as an approximation. Since the behavior of the wave modes in the dispersion curves varies continuously, this approximation holds well for relatively small frequency steps. The frequency step used in our calculation is 10 kHz and the mode sorting procedure worked effectively.

5.4 Dispersion curves and wave structures

5.4.1 Low viscous material: E&C 2057 Cat9 expoxy

In order to verify our calculation, the dispersion curves for a 4 in. schedule 40 steel hollow cylinder coated with 0.02 in. E&C 2057 / Cat9 epoxy are calculated and compared with previous axisymmetric results given by Barshinger [2004]. Nevertheless, the formulation provided in this chapter is general. It is applicable to other pipe sizes and other viscoelastic and elastic cylinders. The materials that can be used in the analytical matrix method can also be implemented in our calculations. It is simply a different input for material and pipe size, the solving procedure remains the same. Even more complex material properties, for example, experimental properties varying nonlinearly with frequency can be easily implemented. However, this is beyond the scope of this thesis and will not be addressed in detail here. The number of elements used in our calculation for the elastic and viscoelastic layers are 24 and 4 respectively. The material properties are listed in Table 5-1, where C_L and C_S are the longitudinal and shear bulk wave velocities respectively. The terms α_L and α_S are attenuation parameters associated with longitudinal and shear bulk waves. They are frequency dependent. The viscoelastic material properties are experimentally measured. Details can be found in Barshinger (2001). Based on the correspondence principle (Christensen 1981), wave propagation problems in elastic materials can be converted to those in viscoelastic materials by simply using complex material parameters. This is quite beneficial for our study, since SAFE

calculations for both elastic and viscoelastic cases are essentially the same, except that the input parameters are different.

Table 5-1: Material properties

Material	C_L (mm/μs)	$\frac{\alpha_L}{\omega}$ $(\frac{dB}{mm}\times\mu s)$	C_S (mm/μs)	$\frac{\alpha_S}{\omega}$ $(\frac{dB}{mm}\times\mu s)$	ρ (g/cm^3)
Steel	5.85	-	3.23	-	7.86
E&C 2057 / Cat9 expoxy	2.96	0.0047	1.45	0.0069	1.6

For comparison purposes, the same dispersion curves for longitudinal and torsional modes are also calculated from the analytical formulation developed in [Barshinger, et al., 2004]. Compared to Barshinger's algorithm, the SAFE formulation calculates dispersion curves 10 times faster without the mode sorting process and twice as fast with the mode sorting process. Barshinger's algorithm based upon the analytical global matrix method calculates only the axisymmetric waves.

It can be seen from the SAFE formulation in this chapter that the dispersion curves can be calculated for any selected circumferential order *n*. However, for each circumferential order (including the axisymmetric case, where *n*=0), the longitudinal and the torsional modes are not separated. In the global matrix method, the axisymmetric longitudinal and axisymmetric torsional wave solution can be decomposed from each other. Therefore, they are calculated separately [Barshinger, et al., 2004]. The comparison of phase velocity and attenuation dispersion curves of the axisymmetric wave modes obtained from SAFE and the axisymmetric longitudinal wave modes from

analytical formulations are shown in Figure 5-2 and Figure 5-3, where the solid lines represent results obtained from the SAFE formulation while the dotted lines are results from analytical formulation. The comparison of phase velocity and attenuation dispersion curves of the axisymmetric wave modes obtained from SAFE and the axisymmetric torsional wave modes from analytical formulations are shown in Figure 5-4 and Figure 5-5, where the solid lines represent results obtained from the SAFE formulation while the dotted lines are results from analytical formulation. As can be seen in these four figures, the phase velocity and attenuation dispersion curves generated by the two different methods are in excellent agreement at low frequency. At very high frequency (higher than 1 MHz), there exists small discrepancies due to relatively large mesh sizes compared to wave length. This can be improved by increasing the number of elements for the discretization in the r direction. Since the frequency range used in guided wave applications is usually lower than 1 MHz, the current mesh configuration will be used throughout the thesis unless otherwise stated.

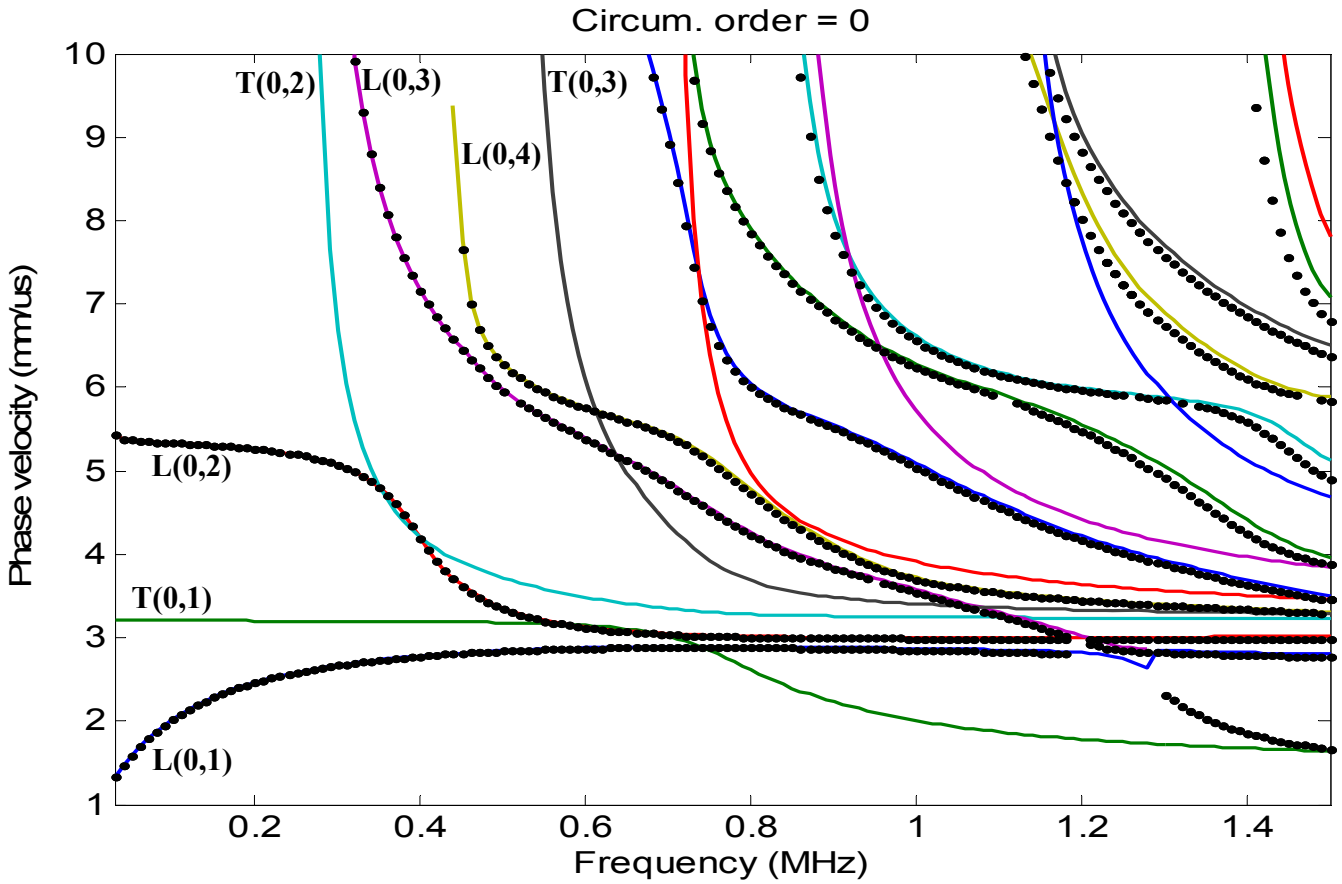

Figure 5-2: Comparison of phase velocity dispersion curves obtained from analytical and SAFE formulations. Dotted line: **longitudinal** modes from analytical formulation; solid line: longitudinal and torsional modes from SAFE formulation.

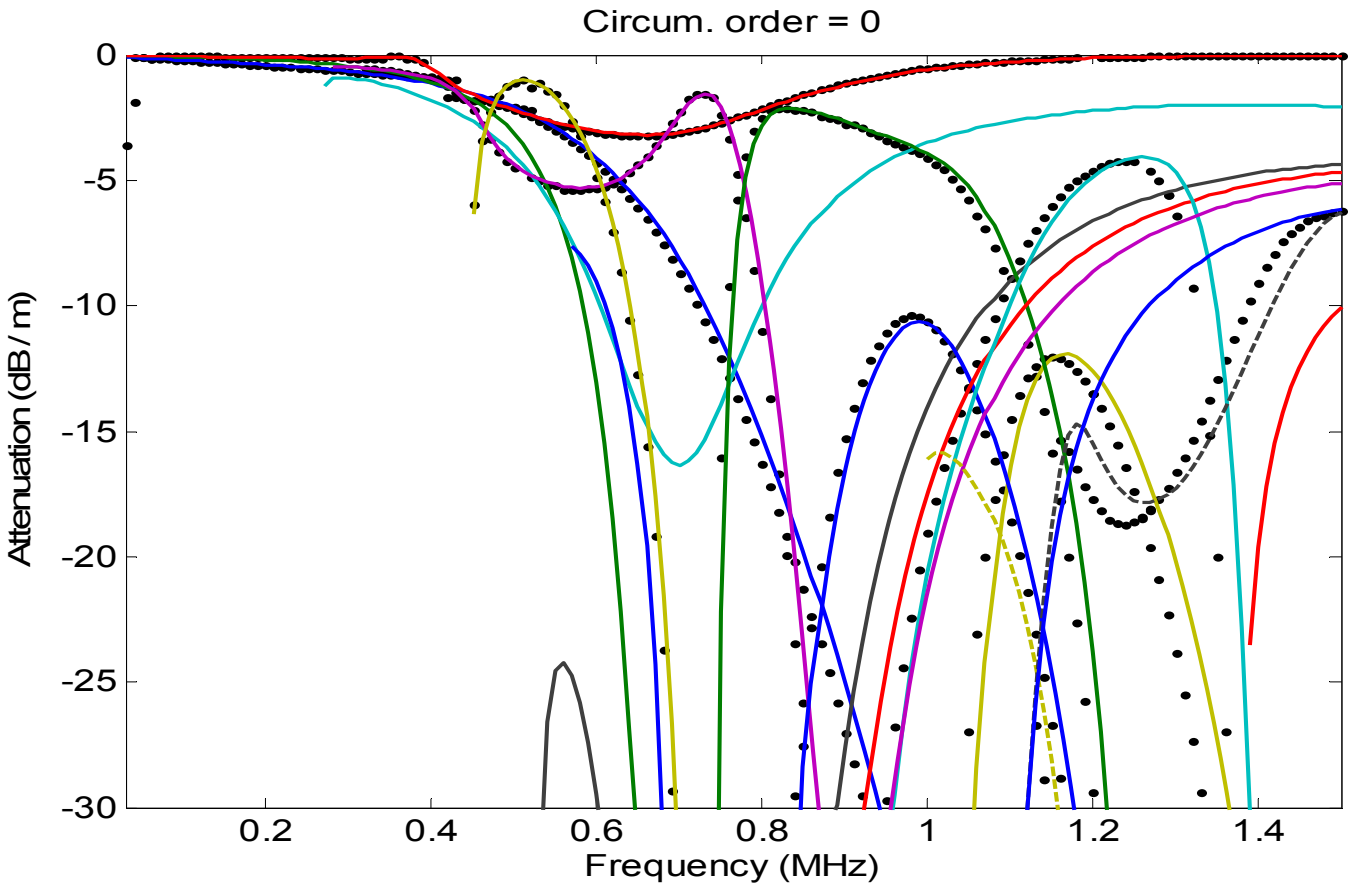

Figure 5-3: Comparison of attenuation dispersion curves obtained from analytical and SAFE formulations. Dotted line: **longitudinal** modes from analytical formulation; solid line: longitudinal and torsional modes from SAFE formulation.

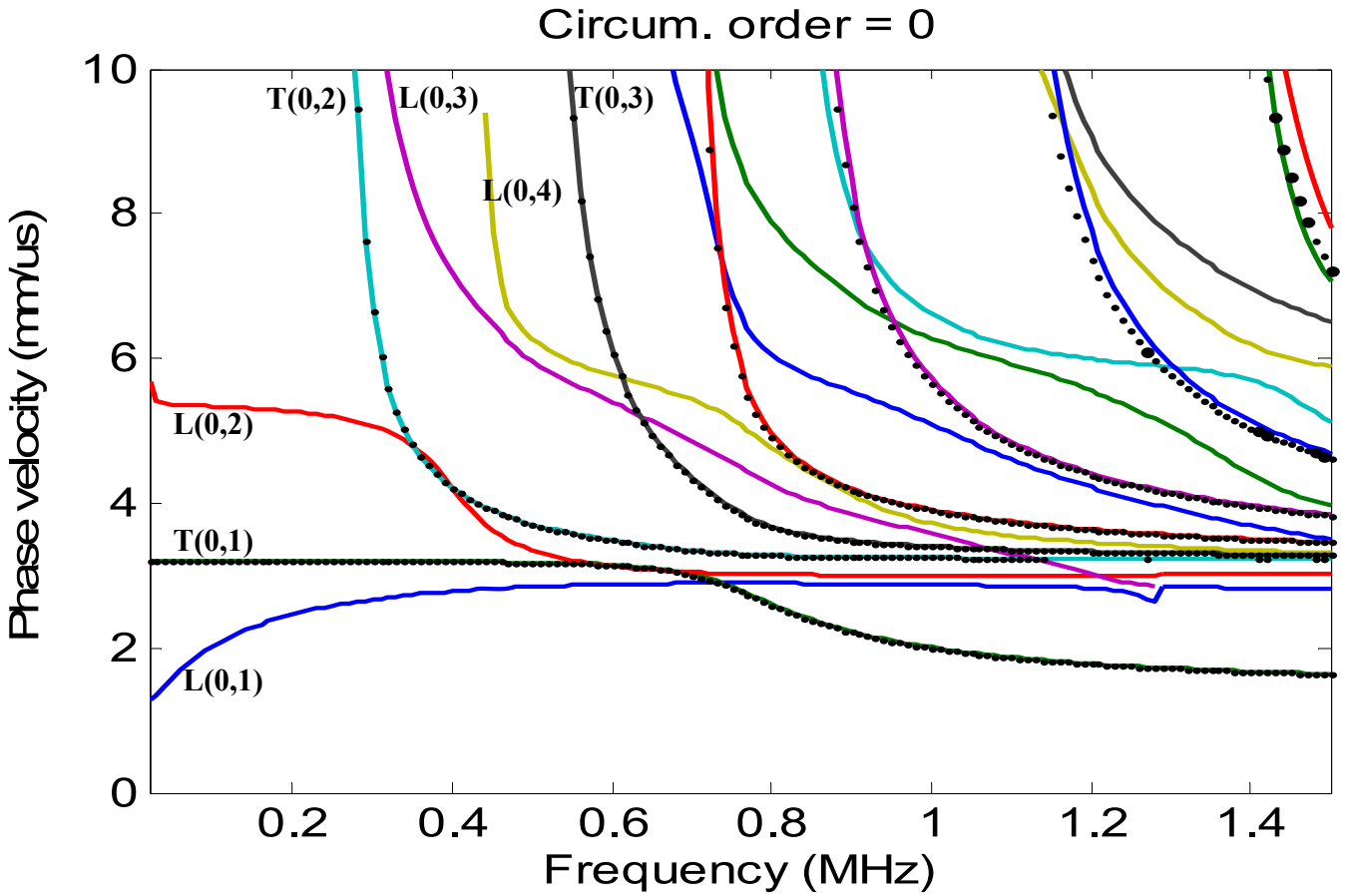

Figure 5-4: Comparison of phase velocity dispersion curves obtained from analytical and SAFE formulations. Dotted lines: **torsional** modes from analytical formulation; solid lines: longitudinal and torsional modes from SAFE formulation.

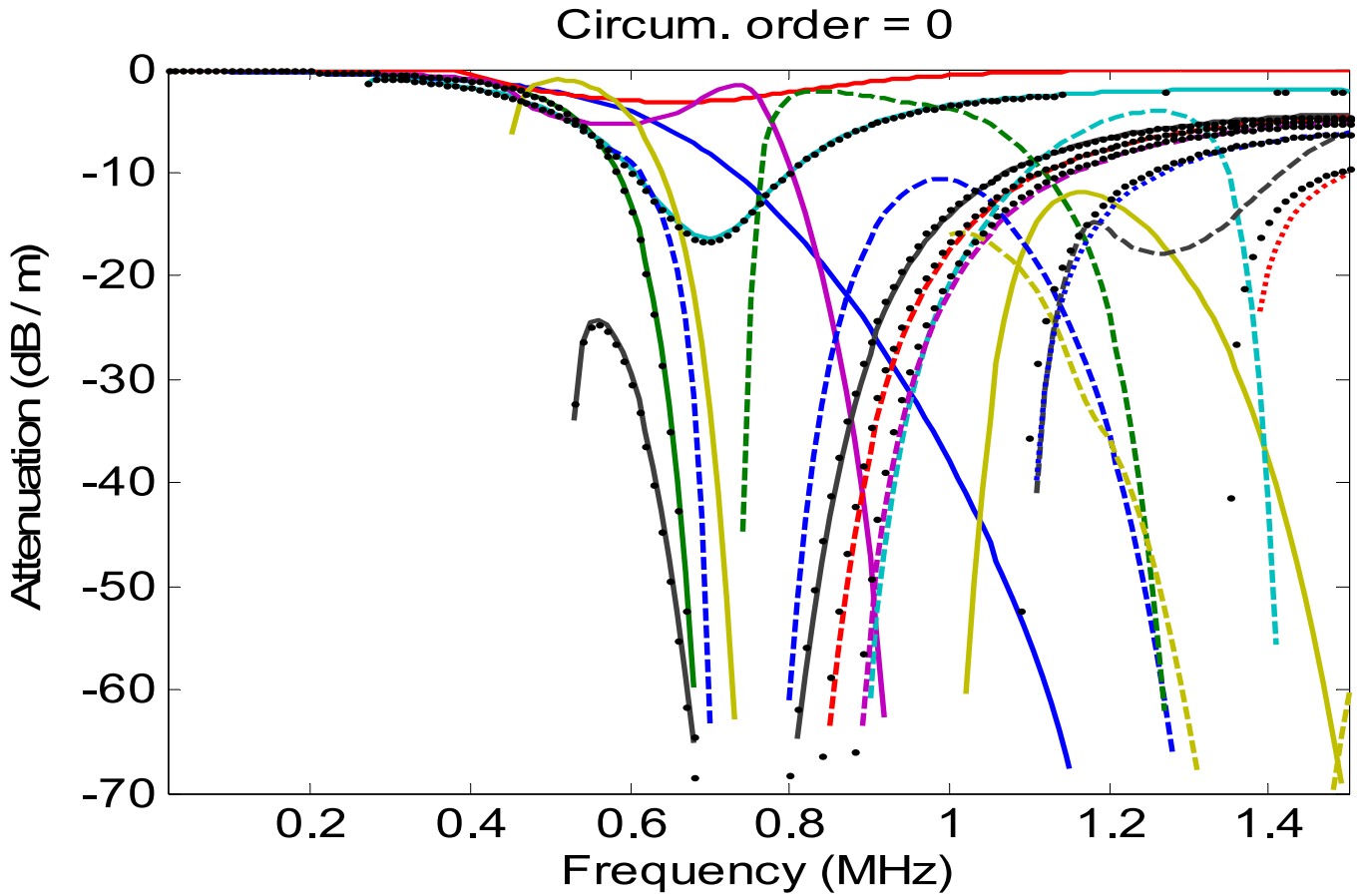

Figure 5-5: Comparison of attenuation dispersion curves obtained from analytical and SAFE formulations. Dotted line: **Torsional** modes from analytical formulation; solid line: longitudinal and torsional modes from SAFE formulation.

Mode sorting is tremendously helpful when using guided wave modes. Especially when the number of wave modes is large (for example, more than 20 modes), there may be multiple mode crossings or mode branches, which makes it difficult to identify the trend of a specific mode under investigation. For well sorted wave modes, it will be very convenient to analyze the behavior of a specific mode with respect to frequency. On one hand, the orthogonality between different modes in natural wave guides provides us with a natural way of mode sorting. On the other hand, mode sorting can also serve as an effective means of verifying the derivation and calculation of dispersion curves.

The dispersion curves of the longitudinal mode group (denoted by L) and the torsional mode group (denoted by T) after mode sorting for axisymmetric (circumferential order n equals zero) and flexural modes (circumferential order n ranging from one to ten) are displayed in Figure 5-6 and Figure 5-7 respectively. For clarity, a magnified figure for wave attenuation at low frequencies (below 300 kHz) is also shown in Figure 5-7.In these two figures, the different modes are sorted beautifully with respect to frequency. The results in Figure 5-6 and Figure 5-7 validate our theory of orthogonality. This orthogonality mode sorting method is fairly powerful and can be applied to various wave guides such as multilayered plates, beams, rods, rails, and so on.

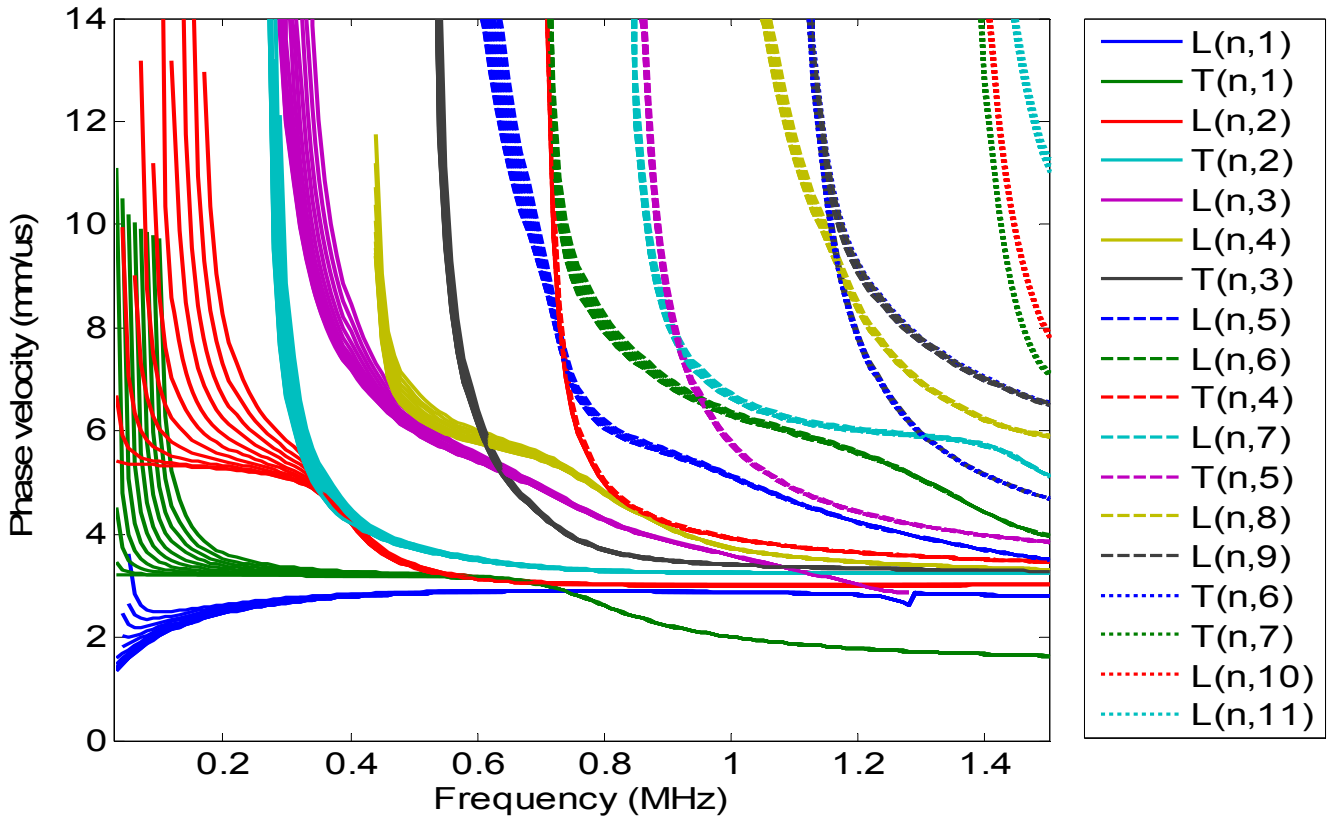

Figure 5-6: Phase velocity dispersion curves for guided wave modes with circumferential order n from 0 to 10 in a 4 in. schedule 40 steel hollow cylinder coated with 0.02 in. thick E&C 2057 Cat9 expoxy.

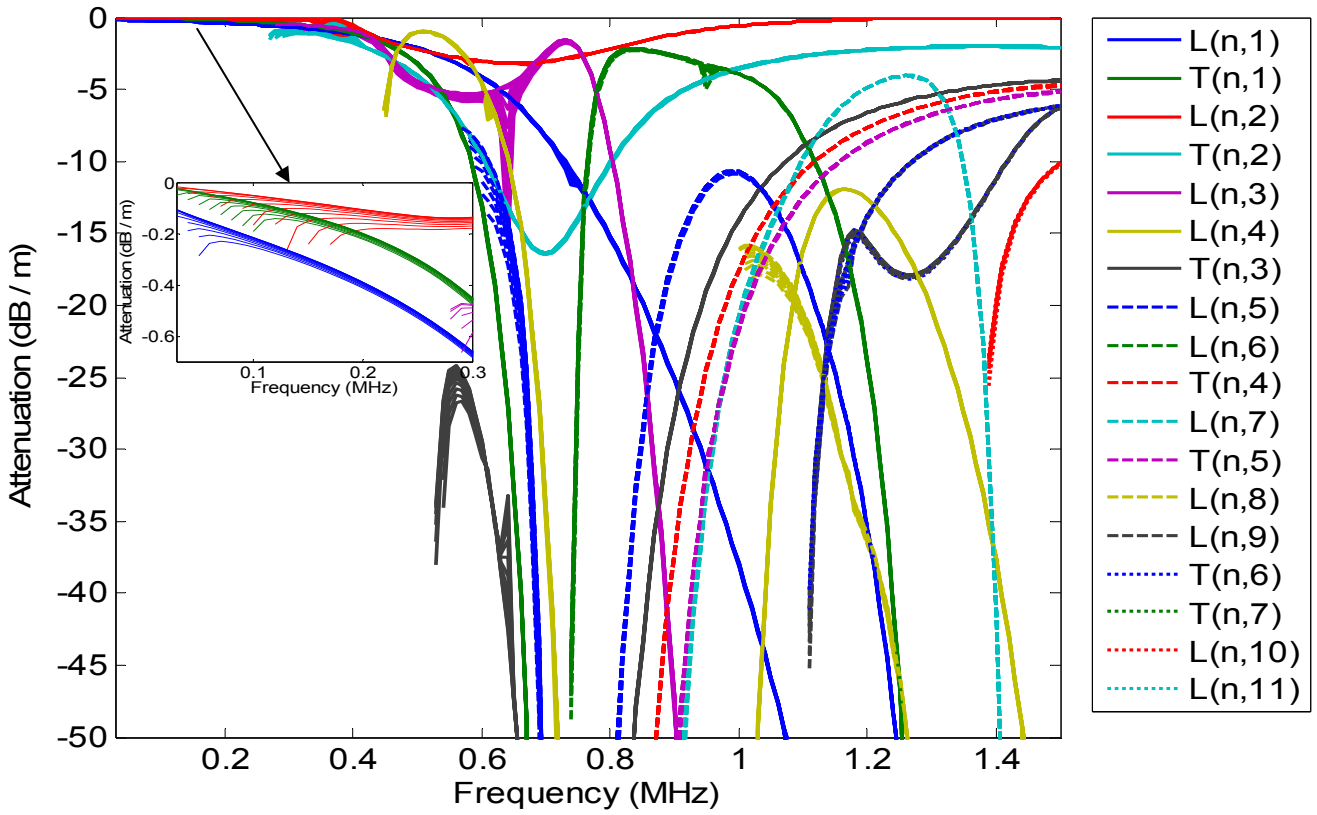

Figure 5-7: Attenuation dispersion curves for guided wave modes with circumferential order n from 0 to 10 in a 4 in. schedule 40 steel hollow cylinder coated with 0.02 in. thick E&C 2057 Cat9 epoxy.

It can be observed from Figure 5-7 that guided wave mode attenuation is quite complicated. However, with careful observation, several characteristics can be noticed:

1) The most striking characteristic in Figure 5-7 is that the mode group L(n,2) has low attenuation over almost the whole frequency bandwidth. Especially for frequency higher than 1.2 MHz, the attenuation of the mode group L(n,2) converges to zero asymptotically. This advantage makes the L(n,2) mode group a suitable choice for a large frequency bandwidth in practical applications.

2) The attenuation of mode groups L(n,1) and T(n,1) increases monotonically with an increase in frequency. This feature also holds for ultrasonic waves in bulk media, which are more attenuative at higher frequencies. The attenuations with these modes below 0.2 MHz are less than 1dB/m. As a result, the wave modes in this region are good choices for nondestructive testing.

3). Generally speaking, for almost all of the other mode groups having cutoff frequencies in the corresponding bare hollow cylinder problem, very high attenuation occurs close to their cutoff frequencies. This makes sense, since they become nonpropagating modes for frequencies lower than their cutoff frequencies in a hollow cylinder without viscoelastic coatings. As the frequency increases, the attenuation (the absolute value of attenuation in Figure 5-7) decreases and reaches its minimum at a certain frequency for a certain mode. After that, the attenuation increases with an increase in frequency like that of bulk waves. This is a significant characteristic since it occurs in almost all of the wave modes. Finding out where the minimal attenuation values occur for the different wave modes is crucial for NDE applications and would be an interesting subject for future work.

Wave structures are displacement amplitude distributions along the thickness direction for certain guided wave modes. The behavior of a specific guided wave mode is highly related to its wave structure. Therefore, it is valuable to check the wave structures of different modes. Some sample wave structures of wave modes L(n,2), L(n,1) and T(n,1) for circumferential orders n=0 and n=5 are shown from Figure 5-8 through Figure 5-13. The coated hollow cylinder size and material parameters are the same as in the previous sections.

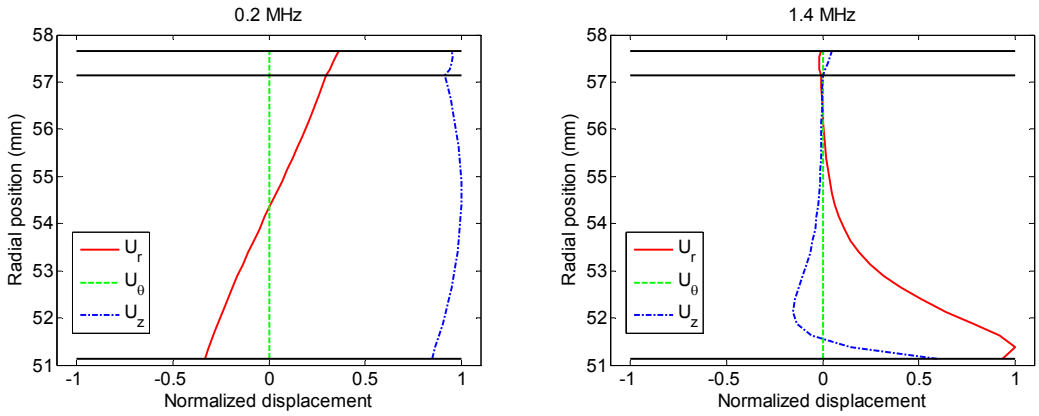

Figure 5-8: Normalized displacement distribution across hollow cylinder thickness for the L(0,2) mode at 0.2 MHz and 1.4 MHz.

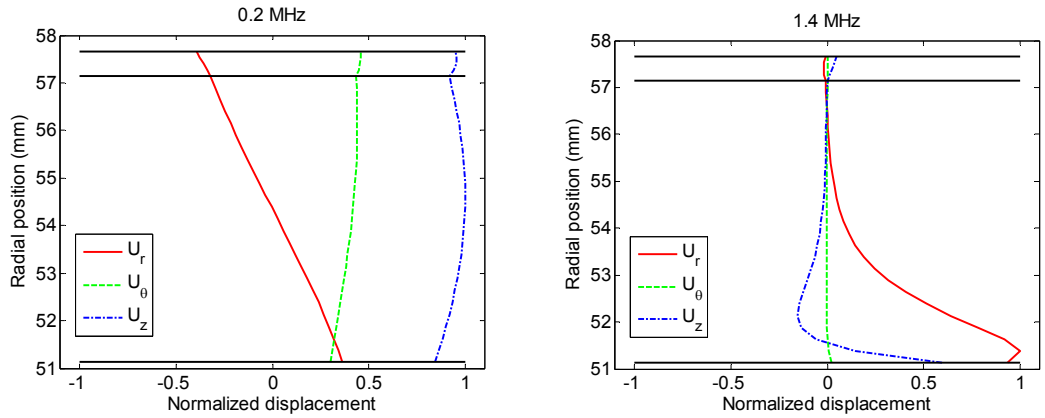

Figure 5-9: Normalized displacement distribution across hollow cylinder thickness for the L(5,2) mode at 0.2 MHz and 1.4 MHz.

From the above analysis regarding the phase velocity and attenuation dispersion curves, it is natural to consider the mode group L(n,2) of most interest, since this group is the least attenuative at both low (<0.32 MHz) and high (>1 MHz) frequencies. Sample wave structures of L(0,2) (axisymmetric mode) and L(5,2) (flexural mode) at 0.2 MHz and 1.4 MHz are shown in Figure 5-8 and Figure 5-9 respectively. It can be seen that the wave structure of L(0,2) at low frequency (0.2 MHz) has a similar distribution as the S0 mode in a plate. The wave structure changes with frequency. At a frequency of 1.4 MHz, the wave structure of L(0,2) changes to become similar to that of a surface wave. In addition, the displacement is mostly concentrated on the inner surface of the two layered hollow cylinder. This phenomenon explains why the attenuation of L(0,2) approaches zero at high frequencies. Comparison of wave structures from L(0,2) and L(5,2) reveals that the displacements in the radial and axial directions (U_r and U_z) have very similar distributions for axisymmetric modes and flexural modes in a mode group. However, the displacements in the circumferential direction for L(0,2) and L(5,2) are similar at high frequency but different at low frequency. This can be expected because the wave

velocities of the modes with different circumferential orders in a mode group are quite different at low frequency, but approach each other at high frequency.

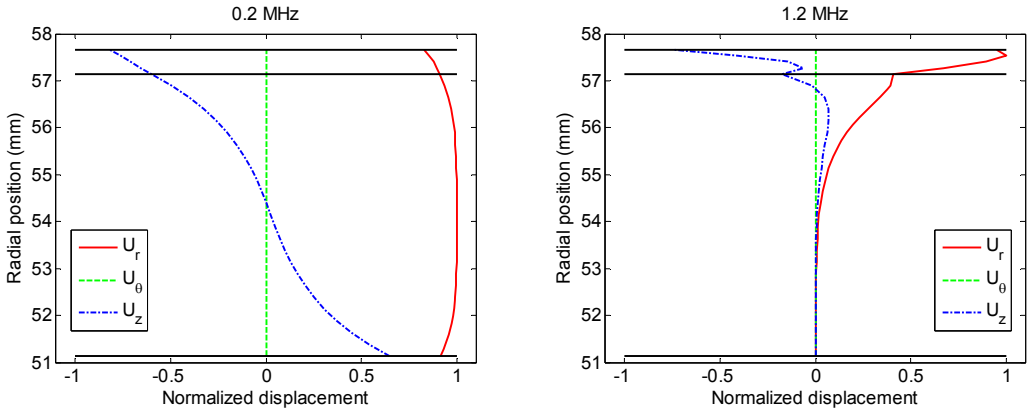

Figure 5-10: Normalized displacement distribution across hollow cylinder thickness for the L(0,1) mode at 0.2 MHz and 1.2 MHz.

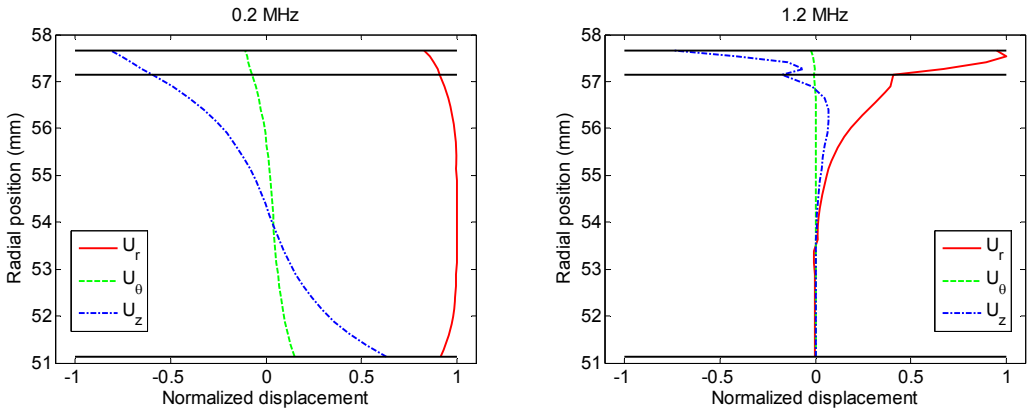

Figure 5-11: Normalized displacement distribution across hollow cylinder thickness for the L(5,1) mode at 0.2 MHz and 1.2 MHz.

Similar phenomena are also observed for the L(n,1) mode group too. At low frequency (0.2 MHz), the wave structure of L(0,1) is similar to that of the Lamb wave mode A0. At high frequency, L(n,1) tends to a surface wave. Contrary to L(n,2), most energy of L(n,1) propagates in the coating layer in a high frequency range, which

indicates that the attenuation of the mode group L(n,1) increases with an increase in frequency. This increase in attenuation can be clearly observed from the attenuation dispersion curves in Figure 5-7. In a similar fashion to L(5,2), L(5,1) also has a bigger displacement in the circumferential direction at low frequency, but very small displacement in the circumferential direction at high frequency. The wave structures of the longitudinal modes L(0,2) and L(0,1) agree quite well with the analytical results in [Barshinger, et al., 2004].

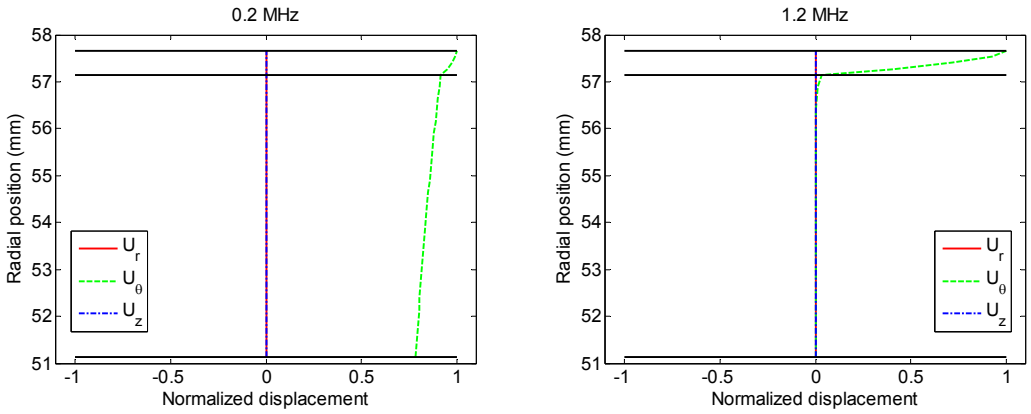

Figure 5-12: Normalized displacement distribution across hollow cylinder thickness for the T(0,1) mode at 0.2 MHz and 1.2 MHz, showing that most energy of T(0,1) is concentrated in the coating layer at high frequency.

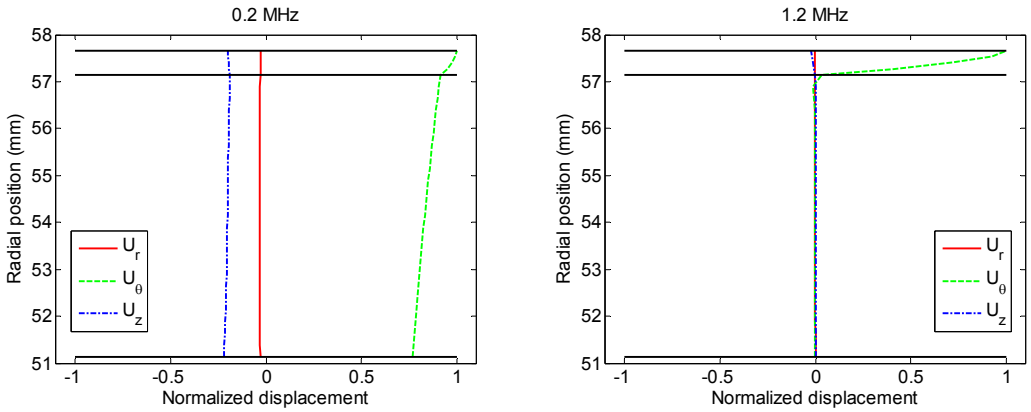

Figure 5-13: Normalized displacement distribution across hollow cylinder thickness for the T(5,1) mode at 0.2 MHz and 1.2 MHz, showing that most energy of T(5,1) is concentrated in the coating layer at high frequency.

The T(n,1) mode group behaves like the SH waves in a plate. For the axisymmetric mode T(0,1), only the displacement in the circumferential direction exists. Both T(0,1) and T(5,1) have almost all of their energy contained in the coating layer. Correspondingly, the attenuation of T(n,1) is very high at high frequency. The increase in attenuation for T(n,1) with respect to frequency can also be observed in Figure 5-7.

From the above discussion, it can be summarized and concluded that, in general, wave mode attenuation in a multilayered hollow cylinder is greatly related to its energy concentration in the viscoelastic layer. The more the energy is concentrated in the viscoelastic layer, the greater the attenuation for the wave mode. This conclusion is also drawn in Simonetti (2004) to approximate the guided wave attenuation by calculating the portion of energy contained in the viscoelastic layer of a multilayered plate structure.

Sample cross sectional deformations of the above wave modes are given in Figure 5-14 to Figure 5-19. Figure 5-14 to Figure 5-16 are for axisymmetric modes, as can be directly seen from the deformation in these figures. Figure 5-17 to Figure 5-19 are

for flexural modes with a period of 5 in the circumferential direction. In order to get better visualization of the cross sectional deformation, the displacements in r, θ, and z directions are magnified by different factors. Therefore, the ratios among the displacement components may differ from those given in the corresponding wave structures. Also, in viscoelastic wave guides, the phases of the displacement components can be any angles in the range of $[0, 2\pi]$. Wave structures are displacement amplitude distributions across thickness. When plotting wave structures, the phases of the displacement components distributed in a 2D plane are mapped to two signs '+' for $[0, \pi]$ and '-' for $[\pi, 2\pi]$. So the relative phases between the displacement components in the cross sectional deformation may not match exactly those given in the wave structures. In all cross sectional deformations, color is used to represent the magnitude of the total displacement. The magnitude of the total displacement can be arbitrary for each mode, so the detailed color scales of the cross sectional deformations are not provided. However, all the color scales are linear and the red color denotes the highest amplitude, while the blue color denotes the lowest amplitude.

Figure 5-14 shows the cross section deformation of mode L(0,1) at a frequency of 200 kHz. Comparing with the wave structure of L(0,1) at 200 kHz in Figure 5-10, it can be seen that the cross section expands (and contracts) in the r direction. At a certain distance, the inner surface and outer surface of the coated pipe expand (and contract) simultaneously. On the contrary, the displacement u_z are out of phase on the inner and outer surfaces. When the outer surface moves in the $+z$ direction, the inner surface moves towards the $-z$ direction and vice versa. These characteristics can be clearly observed in Figure 5-14.

Figure 5-15 shows the cross sectional deformation of mode T(0,1) at a frequency of 200 kHz. As can be seen from Figure 5-12, the only nonzero displacement component is u_θ with the highest amplitude concentrated in the coating layer and the lowest amplitude at the inner surface. This can also be verified by the red color at the coating region and the blue color at the inner surface in Figure 5-15**.**

Figure 5-16 is the cross sectional deformation of mode L(0,2) at 200 kHz. For this mode, the cross section moves up and down in the *z* direction. In the mean time, it also expands and shrinks in the radial direction. In Figure 5-16, the cross section is moving up towards the +*z* direction and expanding in the radial direction. The expanding and shrinking in the radial direction is caused by the out of phase movement of the inner and outer surfaces in the *r* direction as shown in Figure 5-8.

The cross sectional deformations given in Figure 5-17 to Figure 5-19 can easily be interpreted from their corresponding wave structures in a similar way as have been done for the previous figures, so they will not be described in detail here. The only difference is that, now the displacements are in all three directions. Therefore, expanding and contracting are expected in both radial and circumferential directions. In *z* direction, the movement is up and down. In addition, all movements vary periodically in the circumferential direction.

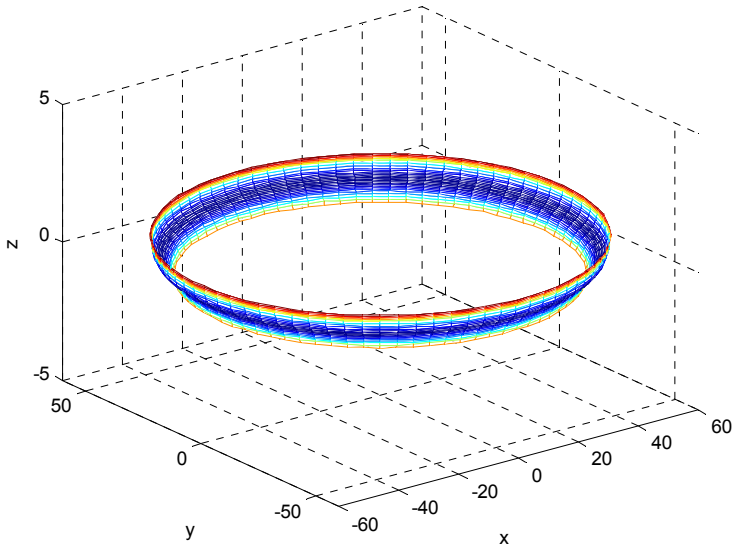

Figure 5-14: Cross sectional deformation of L(0,1) at a frequency of 0.2MHz

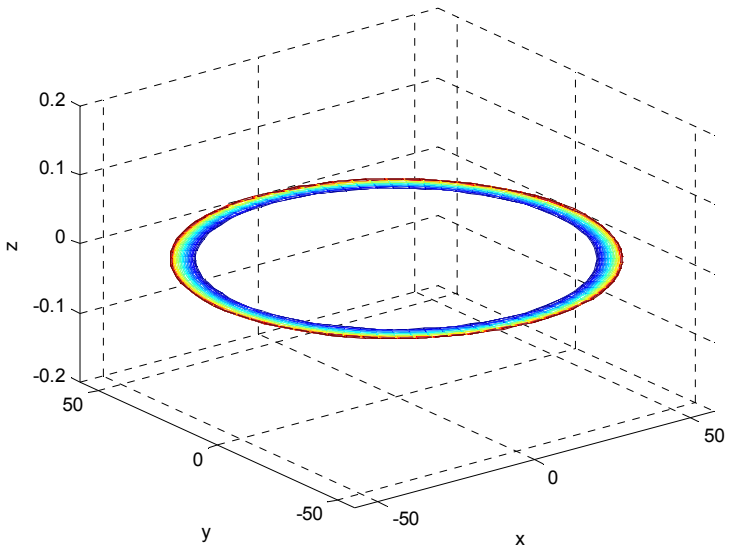

Figure 5-15: Cross section deformation of T(0,1) at a frequency of 0.2MHz

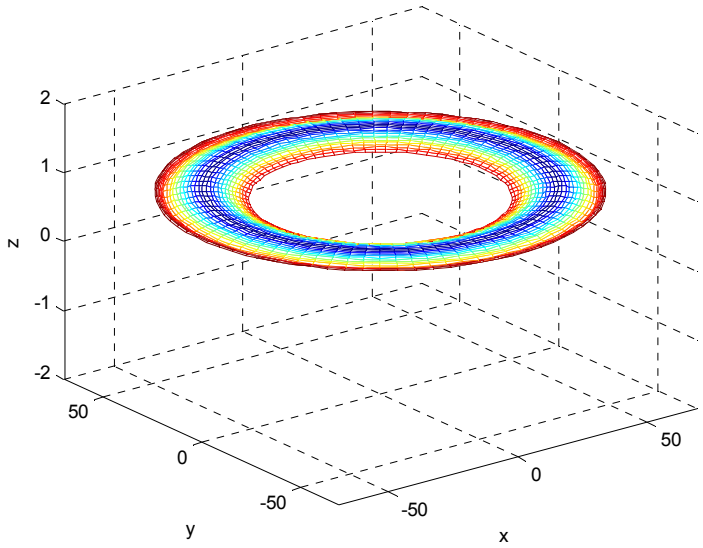

Figure 5-16: Crosss section deformation of L(0,2) at a frequency of 0.2MHz

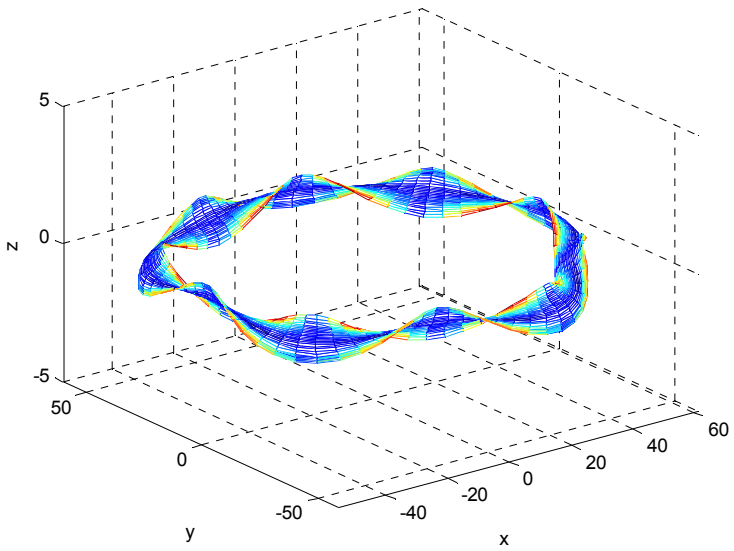

Figure 5-17: Cross sectional deformation of L(5,1) at a frequency of 0.2MHz

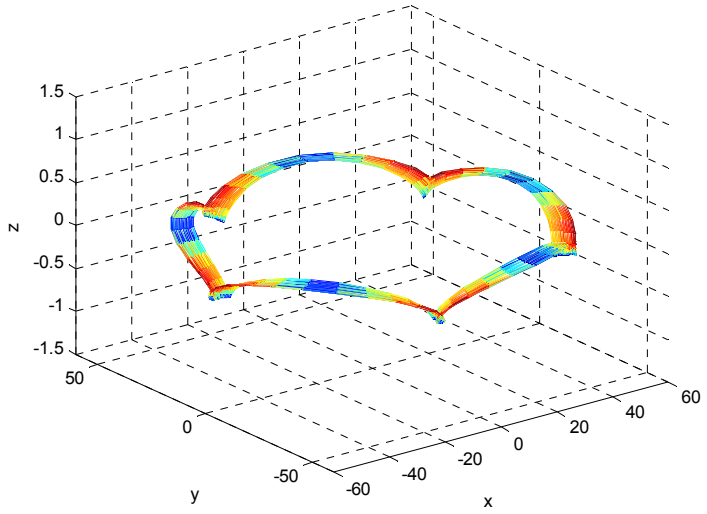

Figure 5-18: Cross sectional deformation of T(5,1) at a frequency of 0.2MHz

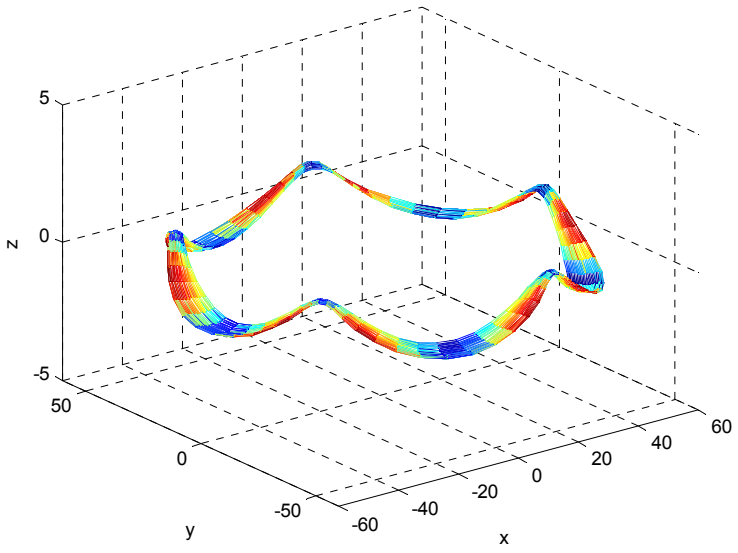

Figure 5-19: Cross sectional deformation of L(5,2) at a frequency of 0.2MHz

5.4.2 Highly viscous material: Bitumastic 50

The properties of Bitumastic 50 are given in Table 5-2. The properties are taken from Barshinger [2004]. It can be seen from Table 5-2 that Bitumastic 50 is much more attenuative, especially for shear waves, compared to E&C 2057 / Cat9 epoxy.

Table 5-2: Material properties

Material	C_L (mm/μs)	$\frac{\alpha_L}{\omega}$ $(\frac{dB}{mm}\times\mu s)$	C_S (mm/μs)	$\frac{\alpha_S}{\omega}$ $(\frac{dB}{mm}\times\mu s)$	ρ (g/cm^3)
Bitumastic 50	1.86	0.023	0.75	0.24	1.5

The phase velocity dispersion curves and attenuation curves for a 4 in. schedule 40 steel pipe coated with 0.02 in Bitumastic 50 are calculated and shown in Figure 5-20 and Figure 5-21. A threshold is set for displaying the dispersion curves, so that the modes with an imaginary part of wave number larger than 0.5 are not shown in Figure 5-20. Comparing the phase velocity dispersion curves in Figure 5-20 and Figure 5-6, two major differences can be observed. First, the phase velocities of certain modes groups L(n,3) and L(n,6) decrease at their low frequencies. Secondly, at relatively high frequencies, some modes experience non-monotonic variation with an increase of frequency, for example, modes L(n,3) and L(n,5) in the circled areas B and A. Non-monotonic change of phase velocity with frequency is also found in the dispersion curves of highly attenuative plates [Chan, et al., 1998]. In this paper, the dispersion curves of highly attenuative plates are solved by the partial wave technique. The author calculated the

ratio between the longitudinal and shear partial waves for different modes. They found that the rise in phase velocity with an increase in frequency may be associated with the amplitude ratio between the longitudinal and shear partial waves in the wave guide. It is also pointed out in the paper that in these rising regions of phase velocities, the conventional way of calculating group velocity dispersion curves by using the formula $c_g = \frac{d\omega}{dk}$ is likely to fail.

Figure 5-21 shows the wave modes whose attenuations are smaller than 100 dB/m. A comparison between the attenuation curves in Figure 5-21 and Figure 5-7 reveals that, overall, the mode groups in a 4 in. schedule 40 pipe coated with Bitumastic 50 are more attenuative than the same mode groups in a 4 in. schedule 40 pipe but coated with E&C 2057/Cat9 epoxy of the same thickness. This agrees with the material properties of the two coatings.

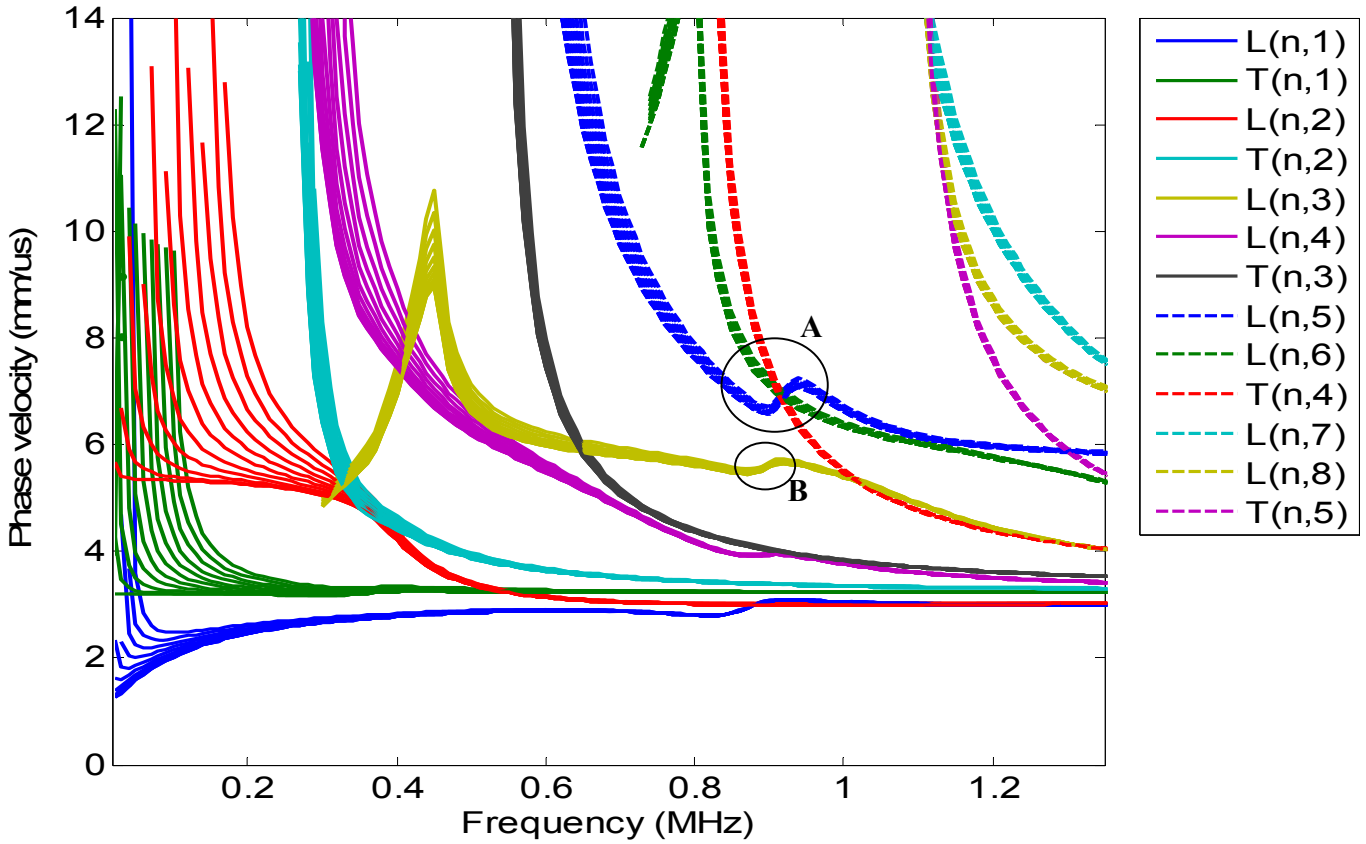

Figure 5-20: Phase velocity dispersion curves for guided wave modes with circumferential order n from 0 to 10 in a 4 in. schedule 40 steel hollow cylinder coated with 0.02 in. thick Bitumastic 50, showing that modes L(n,5) and L(n,3) experience non-monotonic change with frequency in the circled area A and B.

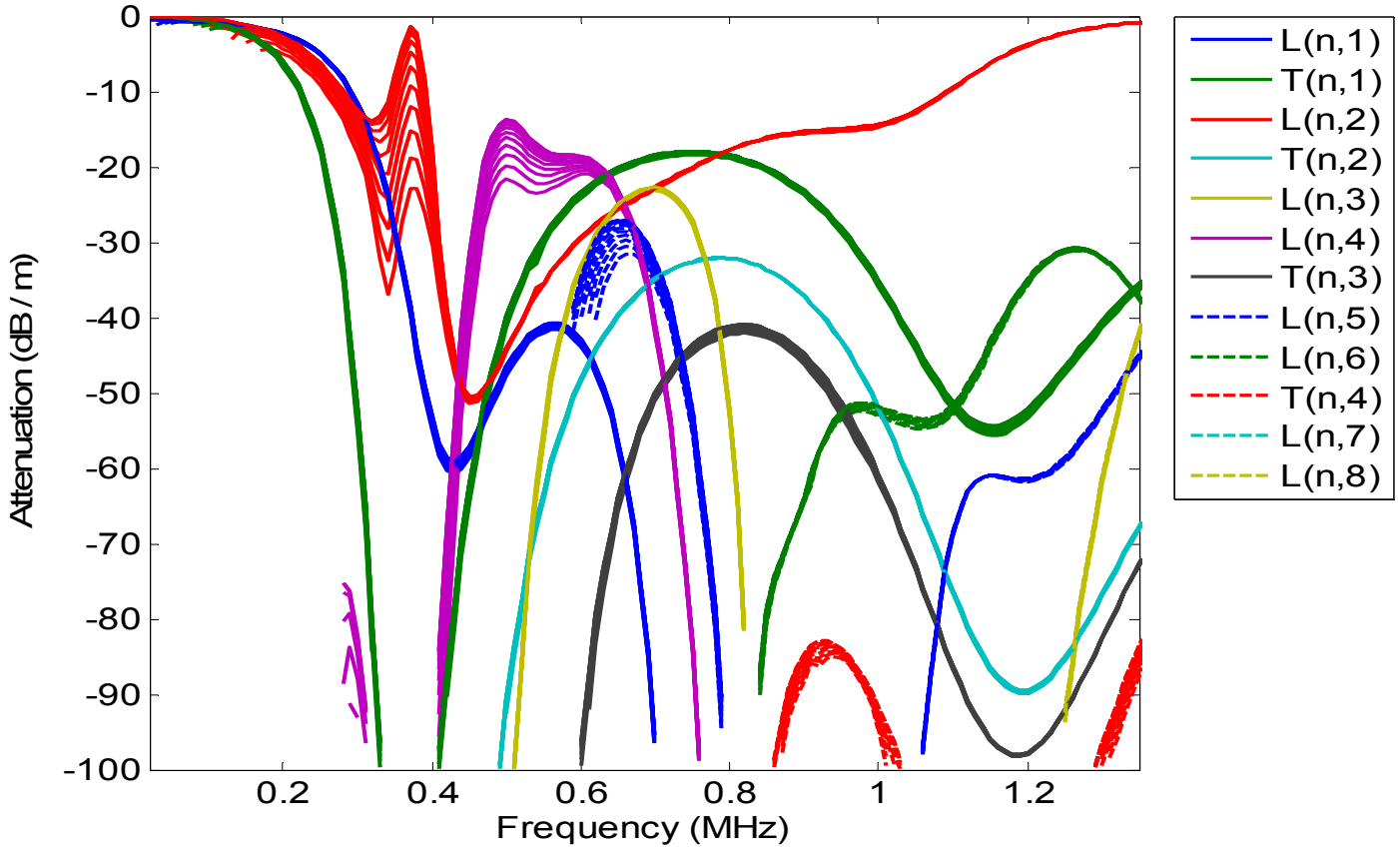

Figure 5-21: Attenuation curves for guided wave modes with circumferential order n from 0 to 10 in a 4 in. schedule 40 steel hollow cylinder coated with 0.02 in. thick Bitumastic 50.

Figure 5-22 shows the magnified axisymmetric phase velocity dispersion curves in the circled area **A** in Figure 5-20. The modal behavior in this region is relatively more complex compared to that in the other regions. In Figure 5-22, several modes cross each other and mode L(0,5) changes non-monotonically with an increase in frequency. Eight points are chosen on the three guided wave modes shown in Figure 5-22 for more analysis. They are labeled from A to H. The detailed information of the chosen modes including frequency, phase velocity values, and attenuation values are listed in Table 5-3. It may be noticed from Table 5-3 that the attenuation values of mode L(0,5) at points A, B, and C are much higher than the attenuation at point D. An inspection of the other guide wave modes reveals that the modes are generally more attenuative in the regions where the phase velocity rise with the increase in frequency than the surrounding regions. This could be the reason why the conventional way of calculating group velocity dispersion curves by using $c_g = \frac{d\omega}{dk}$ fails in these regions.

The wave structures of the four points A to D on the mode L(0,5) are plotted in Figure 5-23. It can be seen from the figure that the four wave structures are very similar to each other, which verifies that they are from the same mode and the mode L(0,5) does evolve non-monotonically with frequency in this region. The wave structures of E and F on the mode L(0,6) are plotted in Figure 5-24. It can be seen that they are from the same mode too. The wave structures of G and H on the mode T(0,4) are plotted in Figure 5-25. It can be seen that the wave structures of the three modes are quite different from each other, while the wave structure of a single mode evolves continuously. This verifies that our mode sorting technique is quite effective.

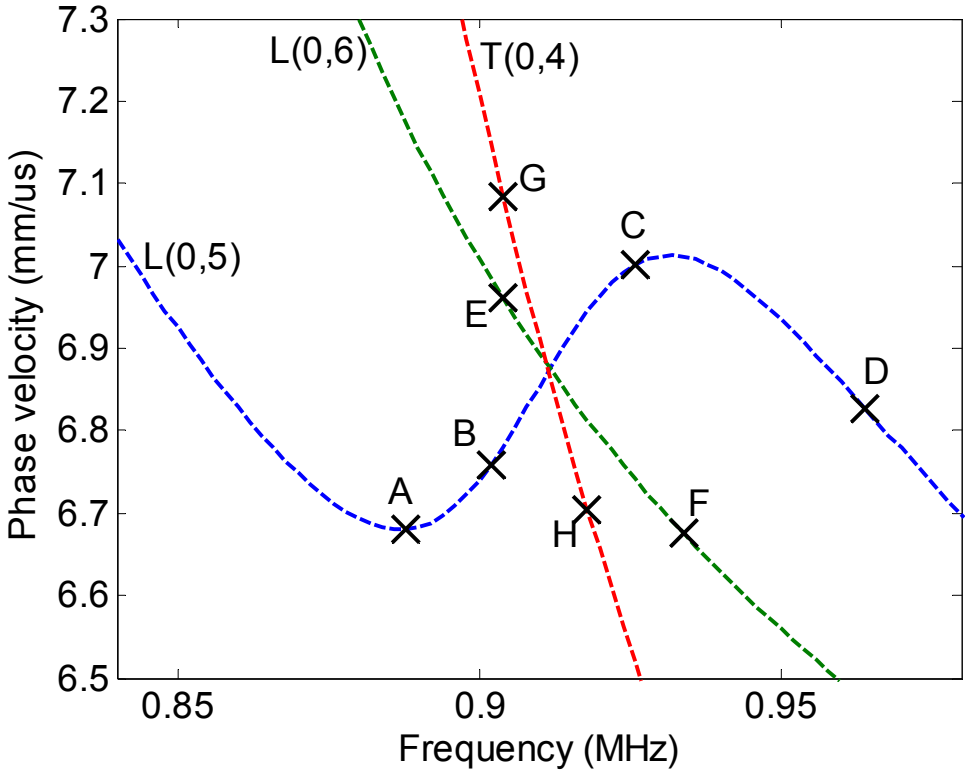

Figure 5-22: Magnified axisymmetric phase velocity dispersion curves in the circled area **A** in Figure 5-20.

Table 5-3: List of selected modes

Label	Mode	Frequency (MHz)	Phase Velocity (mm/μs)	Attenuation (dB/m)
A	L(0,5)	0.888	6.6802	-698.95
B	L(0,5)	0.902	6.7590	-875.21
C	L(0,5)	0.926	7.001	-797.84
D	L(0,5)	0.964	6.8276	-392.48
E	L(0,6)	0.904	6.9608	-71.052
F	L(0,6)	0.934	6.6752	-62.535
G	T(0,4)	0.904	7.0852	-98.064
H	T(0,4)	0.918	6.7044	-98.052

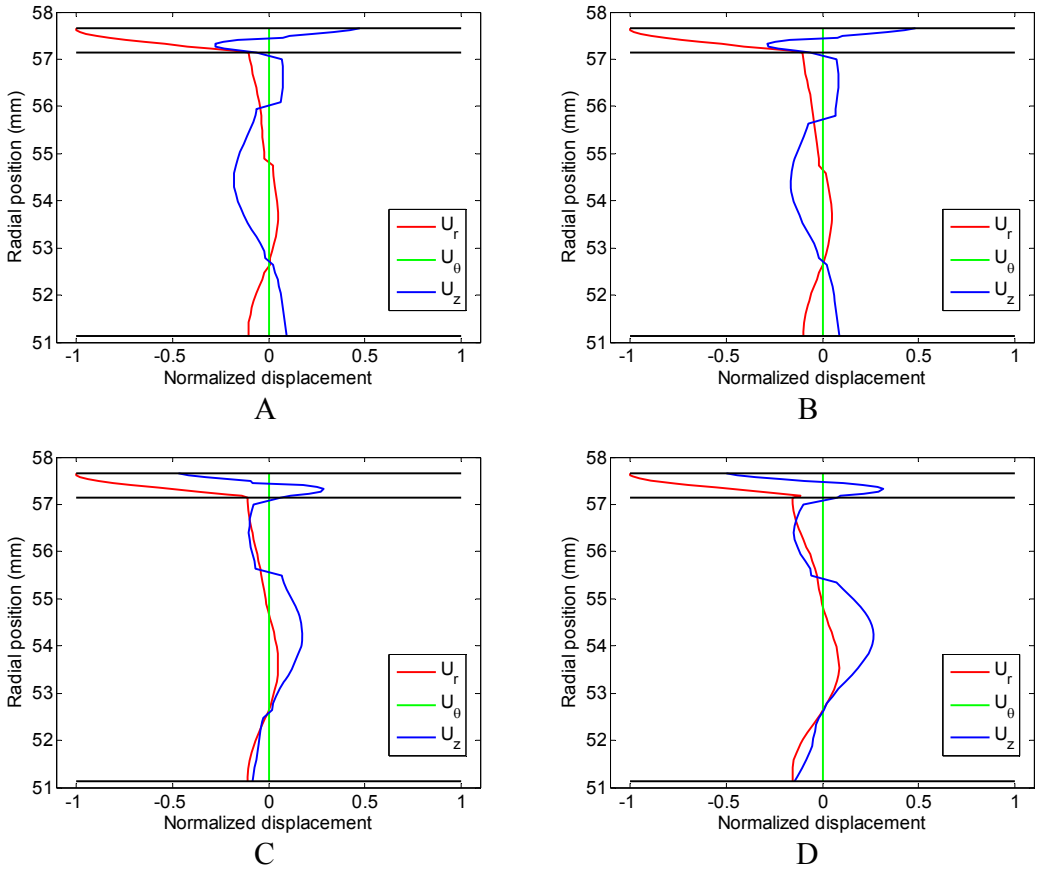

Figure 5-23: The wave structures of A, B, C, and D on mode L(0,5) in Figure 5-22.

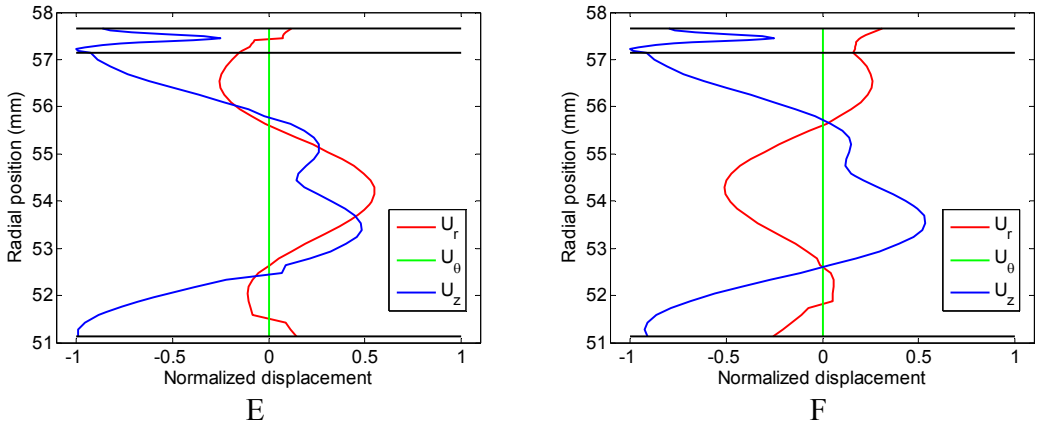

Figure 5-24: The wave structures of E and F on mode L(0,6) in Figure 5-22

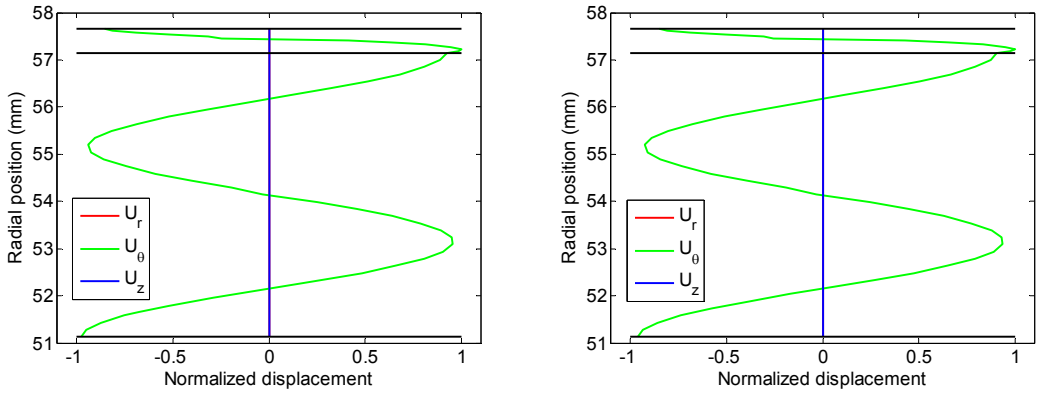

Figure 5-25: The wave structures of G and H on mode T(0,4) in Figure 5-22

5.5 Summary

This chapter solves the problem of guided wave propagation in viscoelastic multilayered hollow cylinders. The Semi-Analytical Finite Element (SAFE) method is adopted to solve this problem. A suitable SAFE formulation is developed. The SAFE formulation enables us to solve the dispersion curves and wave structures of the modes that exist in multilayered hollow cylinders containing viscoelastic materials.

In order to separate different modes and to build the foundation for further research on source influence, the orthogonality relation between the guided wave modes in viscoelastic multilayered hollow cylinders are derived. The orthogonality relation basically means that all the wave modes in a viscoelastic multilayered hollow cylinder are orthogonal to each other. They are all normal modes. The orthogonality relation

derived here is valid in both single-layered and any number of multilayered hollow cylinders with either viscoelastic or elastic materials. Therefore it is more general than the orthogonality relation that has been given by Ditri [1992], which only applies to a single-layered elastic hollow cylinder.

The orthogonality relation is then used to sort all the wave modes. Excellent mode sorting results are obtained. All the normal modes are well separated. This mode sorting enables us to trace the behavior of a specific mode with the change in frequency. It is also the basis of further calculation on source influence and guided focusing in multilayered hollow cylinders.

Finally, numerically results of pipes coated with different viscoelastic materials are given in detail and compared with the axisymmetric modes given by Barshinger [2004]. The flexural modes of higher circumferential orders are first obtained for such coated pipe structures. The numerical mode sorting results validate the analytical derivation of the orthogonality relation. Examples of multiple wave structures are given to show that mode sorting is effective. The cross sectional deformations of various modes are also illustrated to help understand the vibration characteristics of different normal modes.

Chapter 6

Guided wave focusing in viscoelastic multilayered hollow cylinders

The problem of free waves in viscoelastic multilayered hollow cylinders now has been solved. In many practical problems, transducers have to be mounted on the surface in order to send ultrasonic energy into the cylinders. Changing surface conditions affects the ultrasonic energy source and hence mode types; commonly known as "source influence." Similar to the source influence problem in single-layered elastic hollow cylinders, Normal Mode Expansion (NME) can be used as a potent tool to solve the source influence problem in viscoelastic multilayered hollow cylinders. The process of solving the source influence problem in multilayered hollow cylinders is similar to that in a single layered elastic hollow cylinder. The difference lies in the fact that the whole derivation is based upon the real reciprocity relation and one needs to make use of the interfacial displacement and normal stress continuity conditions for the viscoelastic multilayered case, while the derivation for the single-layered elastic case is based on the complex reciprocity relation but no interfacial conditions are considered. These differences also correspond to the differences in the derivation of the orthogonality relations for viscoelastic multilayered cylinders and single-layered elastic cylinders.

6.1 Source influence

Consider the wave field generated by a finite source to be a superposition of all the normal modes in a viscoelastic coated hollow cylinder. This generated wave field is chosen to be solution "1" in the reciprocity relation (Eq. 5.17). The displacement vector and stress tensor of the generated wave field can be expanded as follows

$$\mathbf{v}_1 = \mathbf{v} = \sum_{N=0}^{\infty} \sum_{\mu} A_{\mu}^{N}(z)\mathbf{v}_{\mu}^{N}(r,\theta), \tag{6.1}$$

and

$$\mathbf{T}_1 = \mathbf{T} = \sum_{N=0}^{\infty} \sum_{\mu} A_{\mu}^{N}(z)\mathbf{T}_{\mu}^{N}(r,\theta), \tag{6.2}$$

where N is the circumferential order, μ is the group index, and $A_{\mu}^{N}(z)$ is the amplitude of the normal mode (N, μ) obtained from NME method. The normal mode n of circumferential order M is chosen to be solution "2" in the reciprocity relation. The expressions are given in Eq. 6.3 and Eq. 6.4.

$$\mathbf{v}_2 = \mathbf{v}_n^M(r,\theta)e^{-i\beta_n^M z} \tag{6.3}$$

$$\mathbf{T}_2 = \mathbf{T}_n^M(r,\theta)e^{-i\beta_n^M z} \tag{6.4}$$

Then we have

$$\mathbf{v}_1 \cdot \mathbf{T}_2 = \sum_{N=0}^{\infty} \sum_{\mu} A_{\mu}^{N}(z)\mathbf{v}_{\mu}^{N}(r,\theta) \cdot \mathbf{T}_n^M(r,\theta)e^{-i\beta_n^M z}, \tag{6.5}$$

$$\mathbf{v}_2 \cdot \mathbf{T}_1 = \sum_{N=0}^{\infty} \sum_{\mu} A_{\mu}^{N}(z)\mathbf{v}_n^M(r,\theta) \cdot \mathbf{T}_{\mu}^{N}(r,\theta)e^{-i\beta_n^M z}. \tag{6.6}$$

Subtracting Eq. 6.6 from Eq. 6.5 gives

$$\mathbf{v}_1 \cdot \mathbf{T}_2 - \mathbf{v}_2 \cdot \mathbf{T}_1 = \sum_{N=0}^{\infty} \sum_{\mu} A_\mu^N(z)[\mathbf{v}_\mu^N(r,\theta) \cdot \mathbf{T}_n^M(r,\theta) - \mathbf{v}_n^M(r,\theta) \cdot \mathbf{T}_\mu^N(r,\theta)] e^{-i\beta_n^M z} . \quad 6.7$$

Substituting Eq. 6.7 into the reciprocity relation Eq. 5.17, we obtain

$$\nabla_{r\theta} \cdot [\mathbf{v}_1 \cdot \mathbf{T}_n^M(r,\theta) - \mathbf{v}_n^M(r,\theta) \cdot \mathbf{T}_1] e^{-i\beta_n^M z} + \frac{\partial}{\partial z} \{ \sum_{N=0}^{\infty} \sum_{\mu} A_\mu^N(z)[\mathbf{v}_\mu^N(r,\theta) \cdot \mathbf{T}_n^M(r,\theta) - \mathbf{v}_n^M(r,\theta) \cdot \mathbf{T}_\mu^N(r,\theta)] \cdot \hat{\mathbf{e}}_z e^{-i\beta_n^M z} \} = 0 . \quad 6.8$$

Integrating the preceding equation over the cross section of the cylinder D and making use of the definition of $P_{\mu n}^{NM}$, Eq. 6.8 becomes

$$e^{-i\beta_n^M z} \iint_D \nabla_{r\theta} \cdot [\mathbf{v}_1 \cdot \mathbf{T}_n^M(r,\theta) - \mathbf{v}_n^M(r,\theta) \cdot \mathbf{T}_1] d\sigma = 4 \frac{\partial}{\partial z} \{ \sum_{N=0}^{\infty} \sum_{\mu} A_\mu^N(z) P_{\mu n}^{NM} e^{-i\beta_n^M z} \} . \quad 6.9$$

Eq. 6.9 can be convert to

$$\iint_D \nabla_{r\theta} \cdot [\mathbf{v}_1 \cdot \mathbf{T}_n^M(r,\theta) - \mathbf{v}_n^M(r,\theta) \cdot \mathbf{T}_1] d\sigma = 4 e^{i\beta_n^M z} \frac{\partial}{\partial z} \{ \sum_{N=0}^{\infty} \sum_{\mu} A_\mu^N(z) P_{\mu n}^{NM} e^{-i\beta_n^M z} \} . \quad 6.10$$

Letting

$$\{\} = \mathbf{v}_1 \cdot \mathbf{T}_n^M(r,\theta) - \mathbf{v}_n^M(r,\theta) \cdot \mathbf{T}_1 , \quad 6.11$$

the left hand side of Eq. 6.10 becomes Eq. 6.12 and after some mathematical manipulation as done in the previous chapter for the derivation of orthogonality,

$$\iint_D \nabla_{r\theta} \cdot \{\} d\sigma = \oint_{\partial_1 D} \hat{\mathbf{n}}_1 \cdot \{\} \mathrm{ds} + \oint_{\partial_2 D} \hat{\mathbf{n}}_2 \cdot \{\} \mathrm{ds} + \oint_{\partial_2 D} \hat{\mathbf{n}}_1 \cdot \{\} \mathrm{ds} + \oint_{\partial_3 D} \hat{\mathbf{n}}_2 \cdot \{\} \mathrm{ds} . \quad 6.12$$

In Eq. 6.12, D_1 and D_2 denote the cross sections of the elastic hollow cylinder and the viscoelastic coating respectively. $\partial_1 D$ represents the inner boundary of D_1, $\partial_2 D$

represents the interface between D_1 and D_2, and $\partial_3 D$ represents the outer boundary of D_2. The direction vectors $\hat{\mathbf{n}}_1$ and $\hat{\mathbf{n}}_2$ are defined in Eq. 5.25.

Making use of the identities

$$\hat{\mathbf{n}}_1 \cdot [\mathbf{v}_1 \cdot \mathbf{T}_n^M(r,\theta) - \mathbf{v}_n^M(r,\theta) \cdot \mathbf{T}_1] = \mathbf{v}_1 \cdot (\hat{\mathbf{n}}_1 \cdot \mathbf{T}_n^M(r,\theta)) - \mathbf{v}_n^M(r,\theta) \cdot (\hat{\mathbf{n}}_1 \cdot \mathbf{T}_1), \quad 6.13$$

$$\hat{\mathbf{n}}_2 \cdot [\mathbf{v}_1 \cdot \mathbf{T}_n^M(r,\theta) - \mathbf{v}_n^M(r,\theta) \cdot \mathbf{T}_1] = \mathbf{v}_1 \cdot (\hat{\mathbf{n}}_2 \cdot \mathbf{T}_n^M(r,\theta)) - \mathbf{v}_n^M(r,\theta) \cdot (\hat{\mathbf{n}}_2 \cdot \mathbf{T}_1), \quad 6.14$$

and noticing that the displacements and normal stresses are continuous at the interface $\partial_2 D$, Eq. 6.12 is simplified to

$$\begin{aligned} \iint_D \nabla_{r\theta} \cdot \{\} d\sigma = & \oint_{\partial_1 D} \{\mathbf{v}_1 \cdot (\hat{\mathbf{n}}_1 \cdot \mathbf{T}_n^M(r,\theta)) - \mathbf{v}_n^M(r,\theta) \cdot (\hat{\mathbf{n}}_1 \cdot \mathbf{T}_1)\} \mathrm{ds} \\ & + \oint_{\partial_3 D} \{\mathbf{v}_1 \cdot (\hat{\mathbf{n}}_2 \cdot \mathbf{T}_n^M(r,\theta)) - \mathbf{v}_n^M(r,\theta) \cdot (\hat{\mathbf{n}}_2 \cdot \mathbf{T}_1)\} \mathrm{ds} \end{aligned}. \quad 6.15$$

Also notice that the tractions produced by the normal modes vanish at the inner and outer boundaries, Eq. 6.15 can be further reduced to

$$\iint_D \nabla_{r\theta} \cdot \{\} d\sigma = -\oint_{\partial_1 D} \mathbf{v}_n^M(r,\theta) \cdot (\hat{\mathbf{n}}_1 \cdot \mathbf{T}_1) \mathrm{ds} - \oint_{\partial_3 D} \mathbf{v}_n^M(r,\theta) \cdot (\hat{\mathbf{n}}_2 \cdot \mathbf{T}_1) \mathrm{ds}. \quad 6.16$$

From Eq. 6.10 and Eq. 6.16, we obtain

$$\begin{aligned} & 4e^{i\beta_n^M z} \frac{\partial}{\partial z} \{\sum_{N=0}^{\infty} \sum_{\mu} A_\mu^N(z) P_{\mu n}^{NM} e^{-i\beta_n^M z}\} \\ & = -\oint_{\partial_1 D} \mathbf{v}_n^M(r,\theta) \cdot (\hat{\mathbf{n}}_1 \cdot \mathbf{T}_1) \mathrm{ds} - \oint_{\partial_3 D} \mathbf{v}_n^M(r,\theta) \cdot (\hat{\mathbf{n}}_2 \cdot \mathbf{T}_1) \mathrm{ds} \end{aligned}. \quad 6.17$$

From the orthogonality relation Eq. 5.32, the only non-zero term on the left hand side of Eq. 6.17 is

$$\begin{aligned} & 4e^{i\beta_n^M z} \frac{\partial}{\partial z} \{A_{-n}^M(z) P_{-nn}^{MM} e^{-i\beta_n^M z}\} \\ & = -\oint_{\partial_1 D} \mathbf{v}_n^M(r,\theta) \cdot (\hat{\mathbf{n}}_1 \cdot \mathbf{T}_1) \mathrm{ds} - \oint_{\partial_3 D} \mathbf{v}_n^M(r,\theta) \cdot (\hat{\mathbf{n}}_2 \cdot \mathbf{T}_1) \mathrm{ds} \end{aligned}. \quad 6.18$$

where P_{-nn}^{MM} is from the two modes with wave numbers β_n^M and $-\beta_n^M$. For traction loading on the inner boundary, we obtain

$$4P_{-nn}^{MM}(\frac{\partial}{\partial z}-i\beta_n^M)A_{-n}^M(z)=-\oint_{\partial_1 D}\mathbf{v}_n^M(r,\theta)\cdot(\hat{\mathbf{n}}_1\cdot\mathbf{T}_1)\mathrm{ds}\,. \qquad 6.19$$

For convenience, interchange n and –n, β_n^M and $-\beta_n^M$, we get

$$4P_{n(-n)}^{MM}(\frac{\partial}{\partial z}+i\beta_n^M)A_n^M(z)=-\oint_{\partial_1 D}\mathbf{v}_{-n}^M(r,\theta)\cdot(\hat{\mathbf{n}}_1\cdot\mathbf{T}_1)\mathrm{ds}\,. \qquad 6.20$$

Solving the above equation yields the amplitude factors of the generated normal modes

$$A_n^M=-\frac{e^{-i\beta_n^M z}}{4P_{n(-n)}^{MM}}\int_{-\infty}^{z}e^{i\beta_n^M\eta}\{\oint_{\partial_1 D}\mathbf{v}_{-n}^M(r,\theta)\cdot(\hat{\mathbf{n}}_1\cdot\mathbf{T}_1)\mathrm{ds}\}d\eta \qquad 6.21$$

6.2 Focusing in multilayered viscoelastic hollow cylinders

After the source influence problem is solved, the computation of focusing parameters in multilayered viscoelastic hollow cylinders follows closely to that in single layered hollow cylinders as described in Chapter 3. The transducer location for the source influence in the previous section was assumed to be the inner surface of the pipe. In applications, guided wave focusing in pipes is usually conducted at relatively low frequencies. It is found that, at low frequencies, the dominant displacement and stress distribution are mostly uniform across the thickness. Applying the traction on either the inner surface, outer surface or the interface of the coated pipe does not make a significant

influence in resulting angular profiles and focusing parameters. What is needed to be pointed out here is that the outer surface of the pipe section corresponds to the interface between the pipe and the coating. Sometimes if the coating is very viscous, a small area of the coating can be removed from the pipe to get better coupling between the transducer arrays and the pipe. In this case, part of the energy excited in the bare pipe will be reflected when impinged onto the coated pipe. However, the angular profiles in this work are assumed not to be affected by the reflection between the bare pipe and the coated pipe. The displacement and stress field distribution in bare pipes are almost the same as the displacement and stress field distribution in the pipe section in a coated pipe over low frequency range. This can be observed from the previous calculation on wave structures of the same mode (for example, L(0,2)) in bare pipes (Figure 2-8 in Chapter 2) and in coated pipes (Figure 5-8 Chapter 5). Because of the match in the field distributions between bare pipes and the coated pipes, the influence of reflection on the wave incident from a bare pipe into a coated pipe can be neglected.

6.2.1 Focusing in a single layered elastic hollow cylinder: SAFE vs. analytical GMM

Due to the fact that finite element approximation is used in at least one dimension or two over the cross section of the wave guide in the SAFE method, there have existed some doubts on how accurate the SAFE calculation can be in such a problem of guided wave propagation and focusing in hollow cylinders. Although we have showed by the dispersion curve figures in the previous chapter that the SAFE calculation of coated pipe dispersion curves match those calculated from the analytical global matrix method

(GMM) very well at low frequency. Quantitative comparison was not provided in the previous chapter. In this chapter, we will compare quantitatively the phase velocities, angular profiles, and focusing parameters calculated from both methods for a single layered elastic hollow cylinder to show that the SAFE method can provide enough accuracy in computing the wave propagation and focusing parameters in hollow cylindrical structures.

The phase velocities of modes T(n,1) for n=0 to 10 in an 8 in. schedule 40 steel pipe at a frequency of 60 kHz calculated using the analytical GMM and the SAFE method are listed and compared in Table 6-1. 26 nodes are used in the radial direction across the pipe thickness in the SAFE calculation. Both methods are programmed in MATLAB® using double precision. It can be seen from Table 6-1 that the phase velocities calculated from both methods match each other up to 15 digits.

Table 6-1: Phase velocity comparison using the Analytical GMM and the SAFE for modes T(n,1) in an 8 in. schedule 40 steel pipe at a frequency of 60 kHz. The unit of phase velocity is mm/μs.

Circumferential order n	Analytical GMM	SAFE
0	3.229999999999498	3.229999999999498
1	3.241024295421381	3.241024295421381
2	3.274761185134115	3.274761185134115
3	3.333318152134975	3.333318152134975
4	3.420633969562764	3.420633969562764
5	3.543289222538042	3.543289222538042
6	3.712104504906446	3.712104504906446
7	3.945415614923628	3.945415614923628
8	4.276416296128982	4.276416296128982
9	4.772104034238862	4.772104034238862
10	5.594113921161920	5.594113921161920

The wave structures of the above torisonal flexural modes T(n,1) with n=1 to 6 calculated from analytical GMM and SAFE method are plotted and compared in Figure 6-1. The displacement amplitudes in the r, θ, and z directions are plotted in blue, red, and green respectively. Also, different markers and line styles are used to represent the displacement components calculated by the two different methods as shown in the legend in each plot. It can be seen from Figure 6-1 that the wave structures calculated from the analytical GMM and the SAFE method agree with each other very well.

The amplitude factors of the torsional modes group T(n,1) generated by a 45° shear source loading on the 8 in. schedule 40 steel pipe based on the phase velocities and wave structures calculated for the analytical GMM and the SAFE method are plotted in Figure 6-2. As can be seen from Figure 6-2, the amplitude factors calculated from both methods match very well. Only very slight difference can be observed for the amplitude factors of mode T(1,1) and T(2,1).

Some sample angular profiles for the 45° shear source loading and their corresponding 8 channel focused angular profiles calculated based on analytical and SAFE methods are shown in Figure 6-3. The left column shows the partial loading angular profiles and the right column is the corresponding focused profiles at different axial distances in the 8 in. schedule 40 steel pipe at a frequency of 60 kHz. As can be observed from Figure 6-3, the final focused profiles calculated from both analytical and SAFE methods overlap, indicating they agree with each other quite well. A more quantitative comparison of the focusing parameters calculated from both methods for the focused profile at 0.5 m. in Figure 6-3 is given in Table 6-2. The largest difference

between the focusing parameters calculated from both methods is below 0.3% in this case.

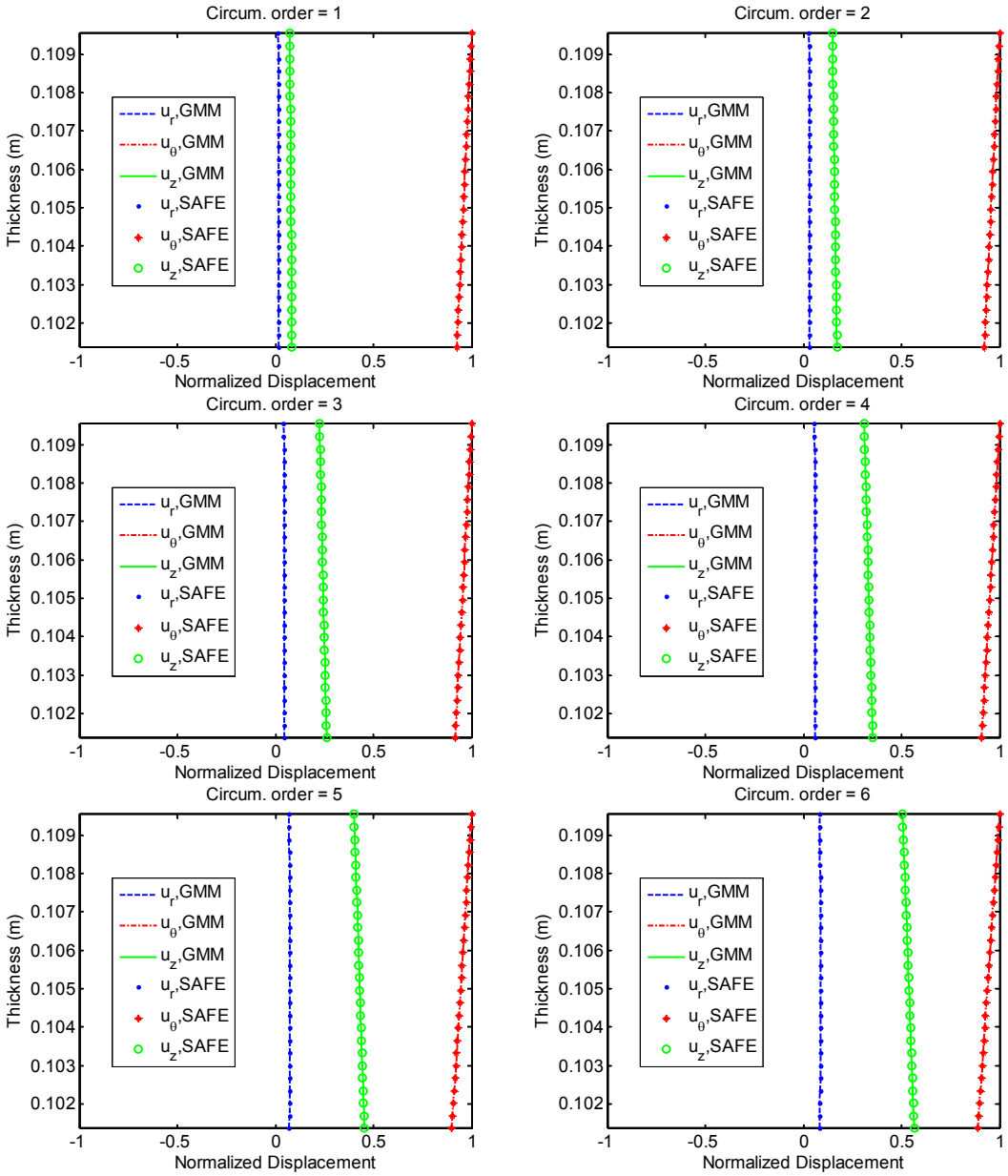

Figure 6-1: Sample wave structure comparison. The wave structures are computed using analytical GMM and the SAFE for modes T(n,1), where circumferential order n equals 1 to 6, in an 8 in. schedule 40 steel pipe at a frequency of 60 kHz.

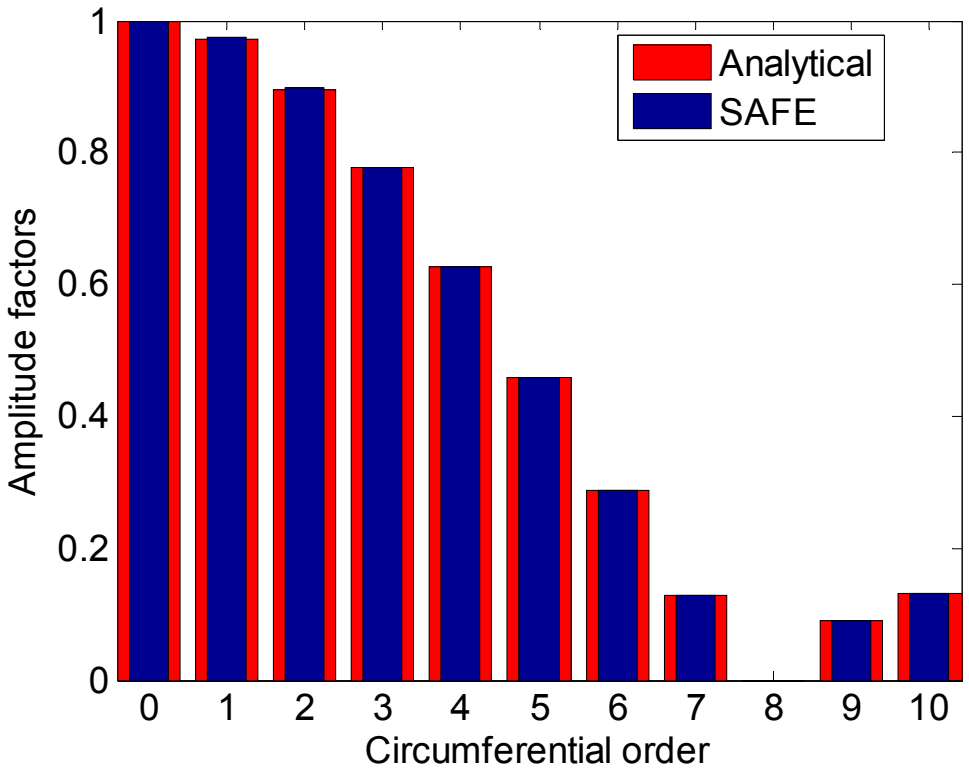

Figure 6-2: Comparison of the amplitude factors computed from the analytical method and SAFE method for a 45° shear partial loading on an 8 in. schedule 40 steel pipe in generating the torsional mode group T(n,1) at 60 kHz. In the figure, the amplitude factors are plotted for circumferential order n from 0 to 10.

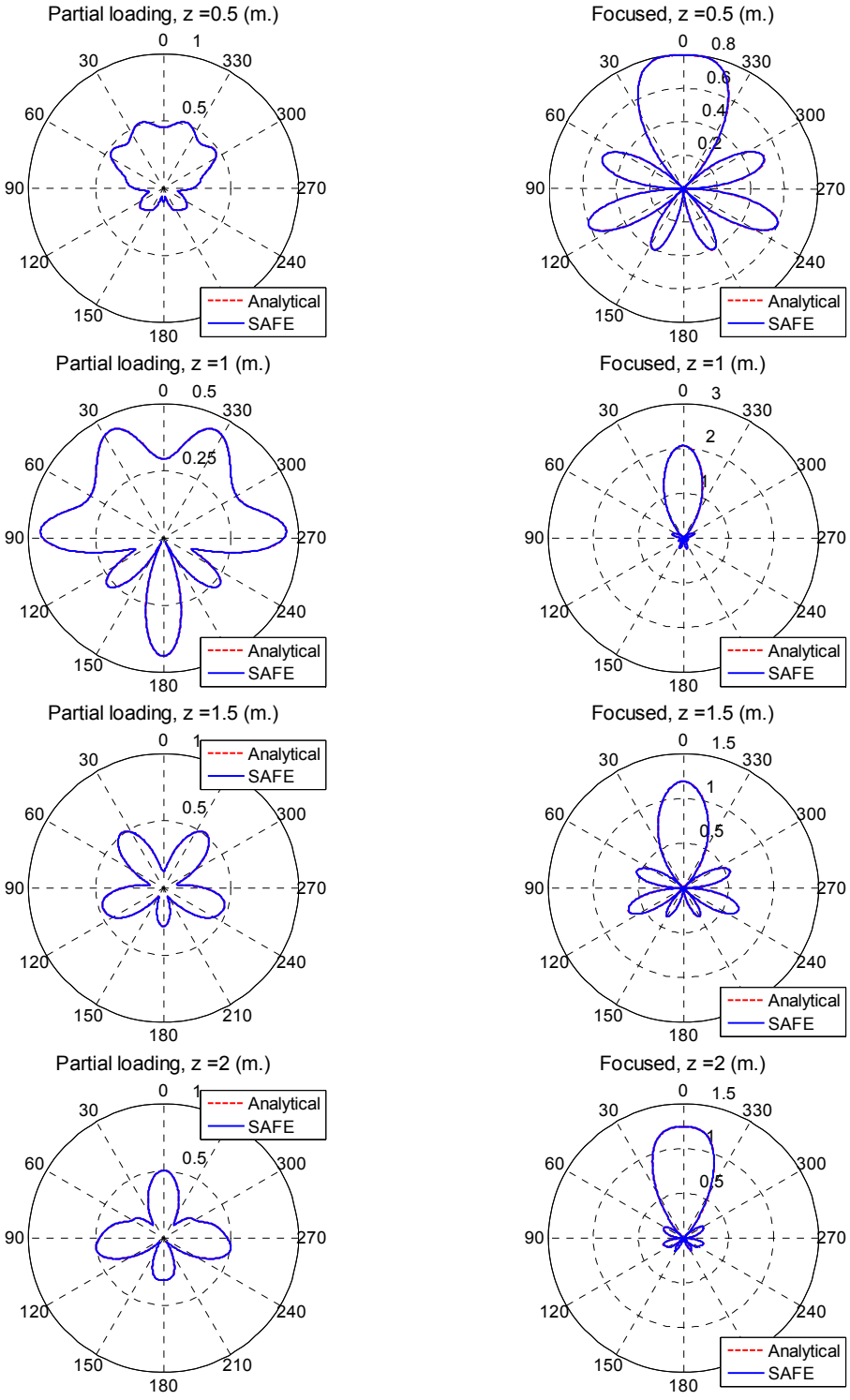

Figure 6-3: Angular profiles of 45° shear partial loading (left column) and their corresponding focused profiles (right column) at different axial distances in an 8 in. schedule 40 steel pipe calculated from analytical and SAFE methods at 60 kHz.

Table 6-2: Comparison of 8 channel focusing parameters in an 8 in. schedule 40 steel pipe at a focal distance of 0.5 m. for torsional modes T(n,1) at 60 kHz. (The focusing parameters correspond to the focused profile on the right hand side in the first row in Figure 6-3.)

	Analytical		SAFE	
Channel #	Amplitude factors	Time delays (μs)	Amplitude factors	Time delays (μs)
1	1.000	14.928	1.000	14.926
2	0.589	9.381	0.589	9.381
3	0.244	5.992	0.244	5.989
4	0.498	16.203	0.497	16.201
5	0.622	6.578	0.621	6.579
6	0.498	16.203	0.497	16.201
7	0.244	5.992	0.244	5.989
8	0.589	9.381	0.589	9.381

The comparison of longitudinal focusing using the analytical method and the SAFE method is also given below. The phase velocities of modes L(n,2) for n=0 to 10 in an 8 in. schedule 40 steel pipe at a frequency of 95 kHz calculated using the analytical GMM and the SAFE method are listed in Table 6-3. 26 nodes (the same as the torsional case) are used in the radial direction across pipe thickness in the SAFE calculation. The phase velocities calculated by the two methods are still in very good agreement, although the accuracy is not as good as in the torsional case. The largest difference in the phase velocities calculated by the two methods is less than 0.0013%.

The amplitude factors of the longitudinal modes group L(n,2) generated by a 45° source loading on the 8 in. schedule 40 steel pipe calculated for the analytical GMM and SAFE methods are plotted in Figure 6-4. As can be seen from Figure 6-4, the amplitude factors calculated from both methods match very well.

A sample angular profile for the 45° longitudinal source loading and its corresponding 8 channel focused angular profiles calculated based on analytical and SAFE methods are shown in Figure 6-5. The left plot in Figure 6-5 is the partial loading angular profile and the right one is the corresponding focused profile at an axial distance of 4.6 m. in an 8 in. schedule 40 steel pipe at a 95 kHz. As can be observed from Figure 6-5, the final focused profiles for the longitudinal case calculated from both analytical and SAFE methods agree quite well with each other. A comparison of the focusing parameters calculated from both methods for the focused profile in Figure 6-4 is given in Table 6-4. The largest difference between the focusing parameters calculated from both methods is less than 6%.

Table 6-3: Phase velocity comparison using the Analytical GMM and the SAFE for modes L(n,2) in an 8 in. schedule 40 steel pipe at a frequency of 95 kHz. The unit is mm/μs.

Circumferential order n	Analytical GMM	SAFE
0	5.357340631484985	5.357365912407072
1	5.376876831054688	5.376902395541808
2	5.436795587539673	5.436822058343757
3	5.541280241012573	5.541308335504786
4	5.698246393203736	5.698277055756171
5	5.921181259155273	5.921215842902375
6	6.232908039093018	6.232948667164218
7	6.673722028732300	6.673772352486621
8	7.321066303253174	7.321133528599280
9	8.346378173828125	8.346479261771242
10	10.235868984401089	10.235868984401089

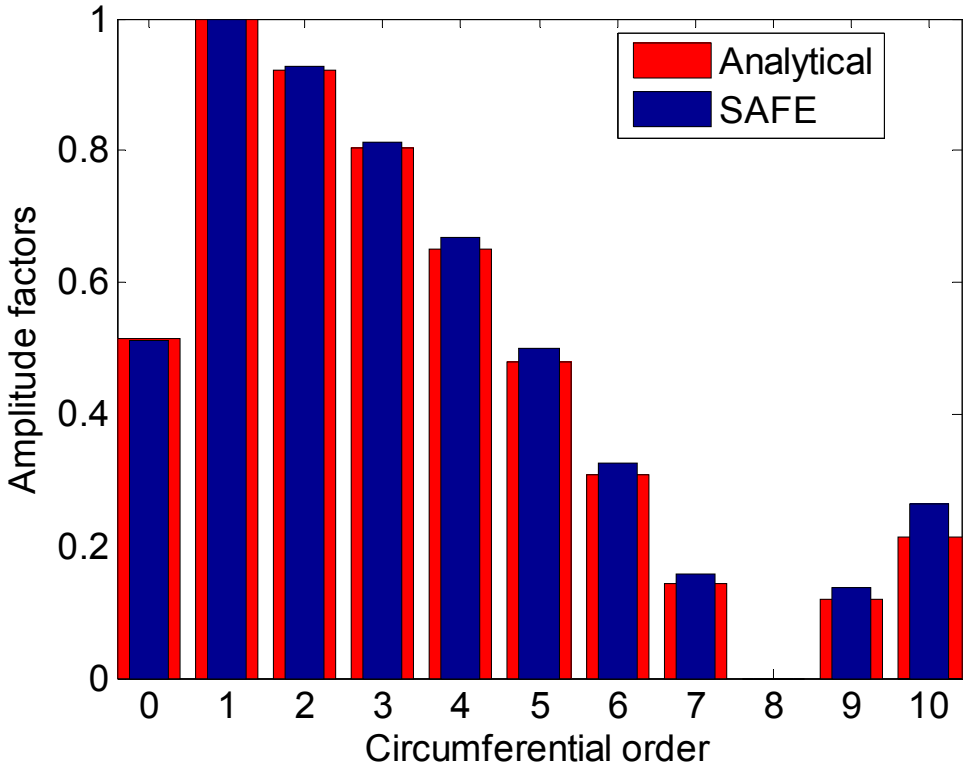

Figure 6-4: Comparison of the amplitude factors computed from the analytical method and SAFE method for a 45° longitudinal partial loading on an 8 in. schedule 40 steel pipe in generating the longitudinal mode group L(n,2) at 95 kHz. In the figure, the amplitude factors are plotted for circumferential order n from 0 to 10.

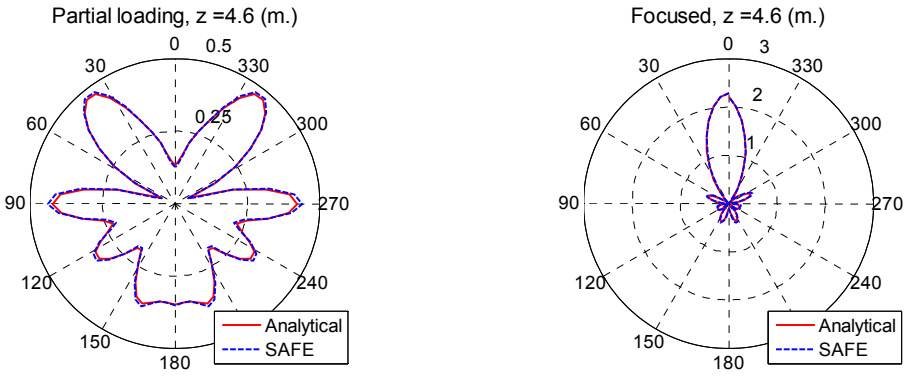

Figure 6-5: Angular profile of 45° longitudinal partial loading (left) and the corresponding focused profile (right) at 4.6 m. in an 8 in. schedule 40 steel pipe calculated from analytical and SAFE methods at 95 kHz.

Table 6-4: Comparison of 8 channel focusing parameters in an 8 in. schedule 40 steel pipe at a focal distance of 4.6 m. for longitudinal modes L(n,2) at 95 kHz. (The focusing parameters correspond to the focused profile on the right hand side in Figure 6-5.)

	Analytical		SAFE	
Channel #	Amplitude factors	Time delays (μs)	Amplitude factors	Time delays (μs)
1	0.617	6.535	0.611	6.589
2	1.000	7.023	1.000	7.019
3	0.933	2.963	0.921	3.025
4	0.686	2.354	0.694	2.370
5	0.678	5.149	0.640	5.065
6	0.686	2.354	0.694	2.370
7	0.933	2.963	0.921	3.025
8	1.000	7.023	1.000	7.019

6.2.2 Focusing in multilayered viscoelastic hollow cylinders using SAFE

The comparison between the focusing in bare pipes using analytical and SAFE methods in the previous chapter shows that the SAFE method is an effective tool in

calculating the focusing amplitude factors and time delays. In this chapter, the SAFE method is used for the calculation of focusing parameters in viscoelastic coated pipes. The method can be generalized in calculating guided wave focusing in other viscoelastic multilayered cylindrical structures also. However, only the numerical calculation of focusing in coated pipes will be given here to demonstrate the technique.

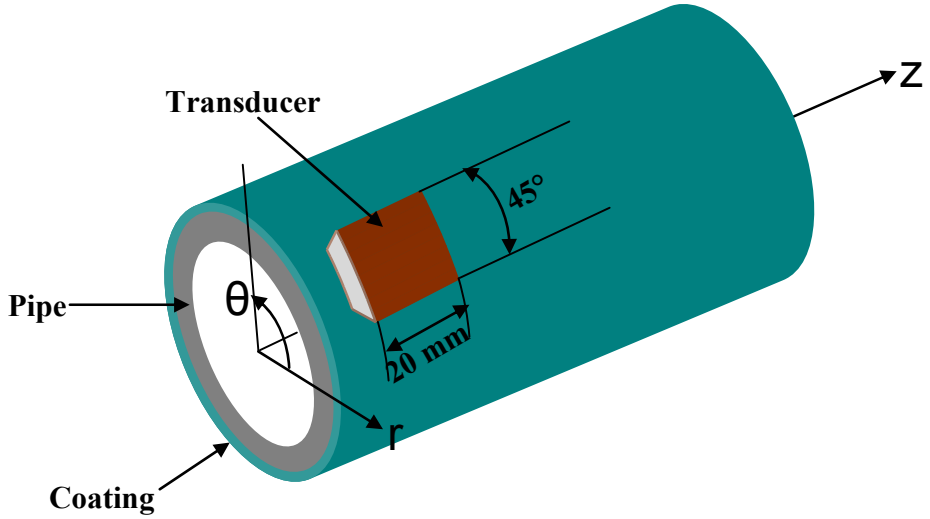

Figure 6-6: Coated pipe with a source loading covering 45°in circumferential direction and 20 mm. in axial direction.

Consider a transducer array covering 45° in the circumferential direction vibrating in the axial direction on the outer surface of an 8 *in*. schedule 40 steel pipe (Figure 6-6). The pipe is coated with 2 mm thick E&C 2057 / Cat9 epoxy. The material properties can be found in Table 5-1. The total field generated by such a partial source loading can be calculated from the amplitude factors of the generated guided wave modes and their superposition. The generated guided wave modes in this case are mostly the longitudinal modes L(n,2). Theoretically speaking, the other longitudinal mode group L(n,1) (n>0), which has small displacement in the z direction, will be generated as well, but with much

smaller amplitudes compared to the generated L(n,2) modes. In addition, the group velocities of the L(n,1) and the L(n,2) modes are very different from each other. In practice, most likely these two mode groups will not reach the focal position at the same time if the exciting signal is a toneburst. Therefore, the displacement angular profiles are only calculated based on the summation of the L(n,2) modes only. The particle displacement angular profiles of the generated field at the interface between the pipe and the coating are shown in the left column of Figure 6-7. Their corresponding 8 channel focused profiles are given in the right column respectively. As shown in Figure 6-7, the angular profiles are plotted at difference sample distances and at a frequency of 120 kHz.

It can be observed from Figure 6-7 that, similar to bare pipes, the angular profile changes with distance in viscoelastic coated pipes due to the difference in phase velocities of the generated modes. Angular profiles are results of the constructive and destructive interference among the wave modes around the pipe circumference. Because the phase velocities vary with frequency, the angular profiles and focusing parameters change with frequency correspondingly.

The angular profile tuning of the torsional modes T(n,1) can be achieved in the same way as longitudinal modes except that the transducer vibration direction should be in the circumferential direction in order to generate the T(n,1) modes. Using the transducers vibrating in the circumferential direction of the pipe coincides with the dominant displacement direction of the torsional modes T(n,1). Thus, the T(n,1) modes can be largely generated. The displacement angular profiles for the T(n,1) modes generated by 45° normal loading in an 8 *in*. schedule 40 steel pipe coated with 2-mm E&C 2057 / Cat9 epoxy are illustrated in the left column of Figure 6-8 for different

propagating distances. Their corresponding 8-channel focused profiles are shown in the right column of Figure 6-8. Similar to the longitudinal case, the angular profiles and focusing parameters change with propagating distance and operating frequency.

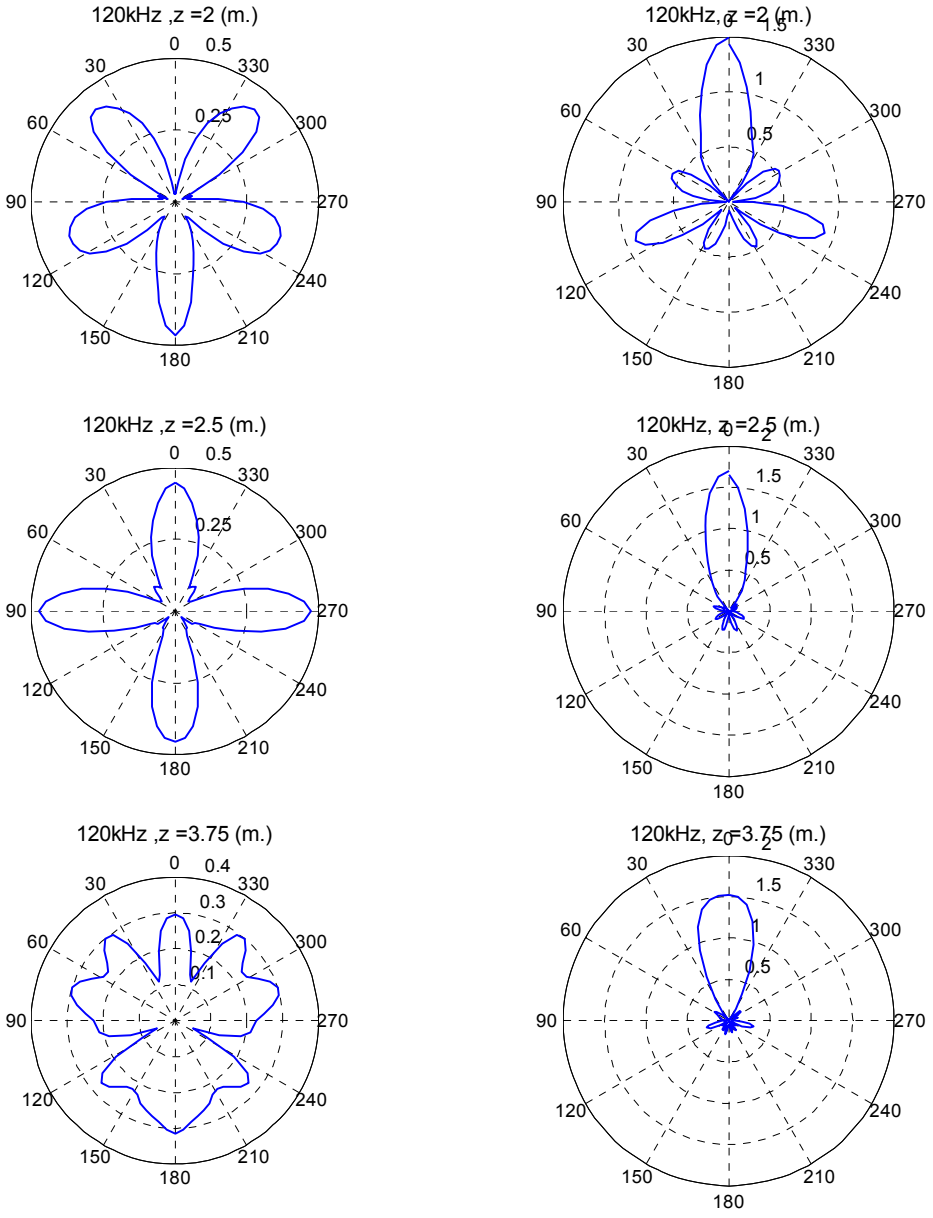

Figure 6-7: The particle displacement angular profiles (left column) and their corresponding focused profiles (right column) at different distances in an 8 *in*. schedule 40 steel pipe coated with 2-mm E&C 2057 / Cat9 epoxy. L(n,2) modes are generated and 8 channel focusing is used.

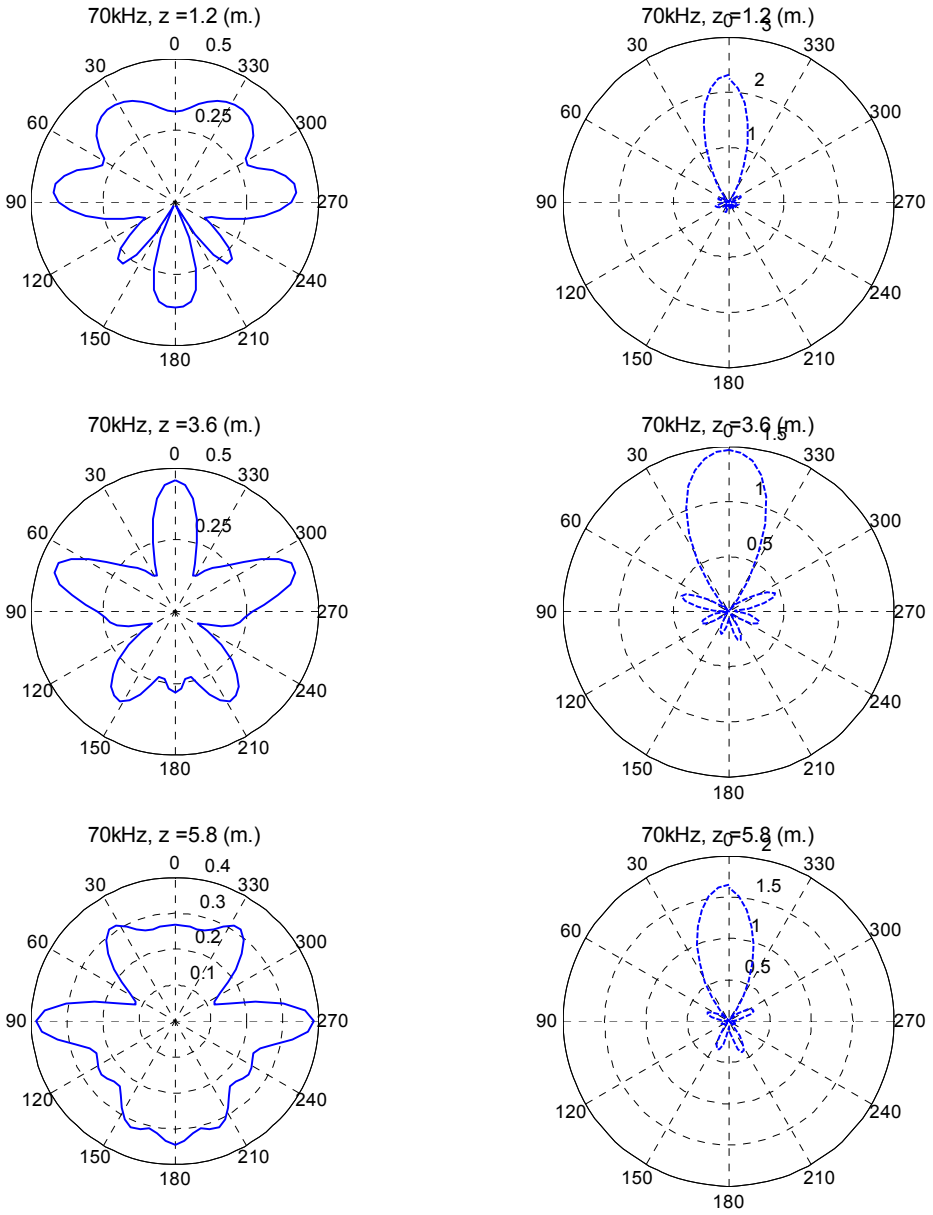

Figure 6-8: The particle displacement angular profiles (left column) and their corresponding focused profiles (right column) at different distances in an 8 *in*. schedule 40 steel pipe coated with 2-mm E&C 2057 / Cat9 epoxy. T(n,1) modes are generated and 8 channel focusing is used.

6.2.3 Comparison of coated pipe and bare pipe focusing parameters

In the previous chapter, it has been shown that the dispersion curve of a viscoelastic coated pipe is similar to that of a bare pipe, especially at low frequency. It would also be interesting to see how much difference there exists in comparing bare pipe parameters and coated pipe parameters used in coated pipe focusing. It can be easily understood that bare pipe focusing parameters probably work very well in coated pipes where the coatings are very thin compared to pipe thickness. When the coating gets thicker, a difference should exists in the focused profiles for the focusing parameters calculated from the bare pipe only and the pipe with coating taken into account.

The comparison of 8 channel longitudinal focusing at 60 kHz using coated pipe parameters and the corresponding single layer bare pipe parameters are shown in Figure 6-9. The comparison for the 12 channel torsional focusing is given in Figure 6-10. An 8 in. schedule 40 steel pipe coated with 1.5 mm Cat9 expoxy is used as an example here. In both figures, the comparison of the partial loading angular profiles at the focal distance is shown in the left. The partial loading angular profiles for the coated pipe are plotted using blue solid lines. The partial loading angular profiles for the 8 in. schedule 40 single layer steel pipe are plotted by red dash-dot lines. The focused profiles using the coated pipe parameters and the bare pipe parameters, as well as the axisymmetric wave profiles, are illustrated in the right columns of Figure 6-9 and Figure 6-10. The focused profiles using the coated pipe parameters are plotted using

blue solid lines. The focused profiles in the coated pipe but using the bare pipe parameters are denoted by red solid lines. The axisymmetric wave profiles at the propagating distances are represented by green solid lines.

It can be seen from Figure 6-9 and Figure 6-10 that at these propagating distances the focusing parameters calculated from the coated pipe can provide significantly higher penetration power than the aixisymmetric waves. Also, the parameters calculated from the coated pipe focuses much better than the focusing parameters calculated from the corresponding bare pipe. In Figure 6-9, the parameters calculated from the bare pipe are still able to focus at the correct circumferential location. In Figure 6-10, the bare pipe focusing parameters completely fail to focus in coated pipe. These numerical examples demonstrate that calculation of the focusing parameters based on the coating pipe configuration is necessary. It is also revealed from numerical calculations that at other distances, it is possible that the bare pipe focusing parameters work almost as well as the coated pipe parameters in the coated pipe, particularly when the propagating distances are not too long. The reason lies in the deconvolution algorithm we use to calculate the focusing parameters. In the deconvolution algorithm, our goal of focusing is to achieve a constructive interference at 0º (the center of channel #1) while complete destructive interference at the center of the other channels. This is why a 4 channel focused profile will always have 2 side lobes, while an 8 channel focused profile always has 6 side lobes. The smallest amplitude between two lobes is strictly controlled to be zero and the locations of these minima correspond to the center of channel #2 to #6. Due to the fact that the deconvolution algorithm strictly controls the amplitude at the

center of channel #2 to #6 to be zero, the focused amplitude in the channel #1 can be sacrificed. In other words, the focused amplitude and the focusing parameters from the deconvolution process may not be optimal in some cases. Therefore, in these cases, the bare pipe focusing parameters may work well in the coated pipe too, because the bare pipe focusing parameters do not control the side lobes in the coated pipes. In general, when the propagating distances are long enough and the coatings are thick enough, the bare pipe parameters may finally fail in the coated pipe. However, the relationship between the focal amplitude at a certain distance and the coating thickness may not be linear or monotonic. If bare pipe parameters are to be used in coated pipe inspection, a parametric study should be conducted to evaluate the distances and frequencies where the bare pipe parameters can fail.

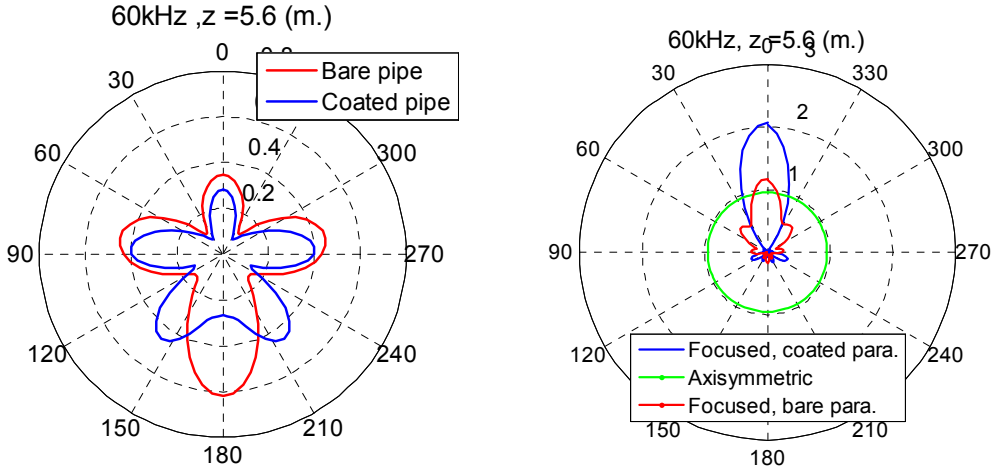

Figure 6-9: Longitudinal L(n,2) 8 channel focusing in an 8 in. schedule 40 steel pipe coated with 1.5 mm Cat9 expoxy at 60 kHz. Left: partial loading profiles at 5.6 m. in the coated pipe (blue) and the corresponding bare pipe (red); right: axisymmetric(green), focused profiles using bare pipe parameters (red) and coated pipe parameters (blue) at 5.6 m.

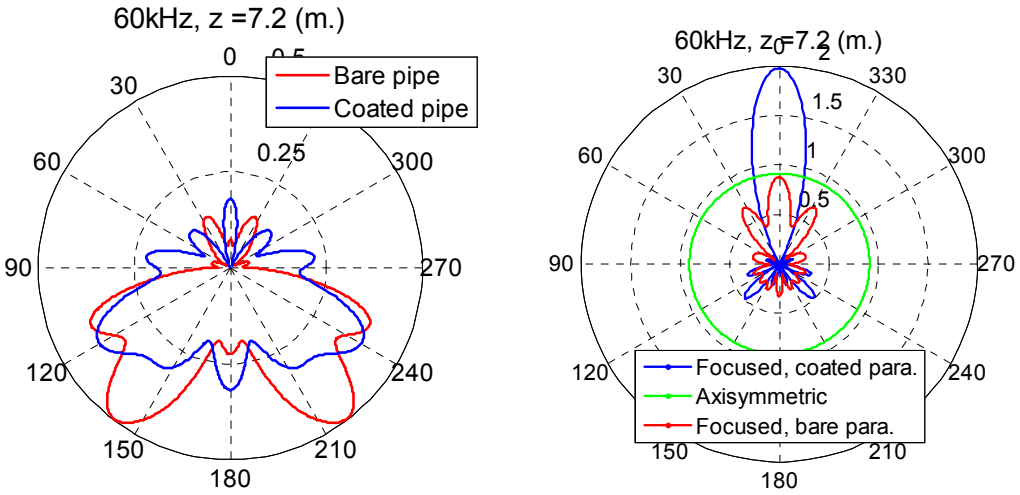

Figure 6-10: Torsional T(n,1) 12 channel focusing in an 8 in sch. 40 steel pipe coated with 1.5 mm Cat9 expoxy at 60 kHz. Left: partial loading profiles at 7.2 m. in the coated pipe (blue) and the corresponding bare pipe (red); right: axisymmetric(green), focused profiles using bare pipe parameters (red) and coated pipe parameters (blue) at 7.2 m.

6.3 FE modeling of focusing in coated pipes

FE modeling is now widely adopted as a suitable tool to analyze problems with complex structures. It is also convenient to use FEM in numerical experiments to visualize physical phenomenon and to verify theories. In this work, ABAQUS is used to simulate guided wave focusing in coated pipes. The process of modeling is discussed below.

The modeled pipe is an 8 in. schedule 40 steel pipe with 1.5 mm thick bitumastic 50 coating. The focal distance is designed to be 5.6 m. The focusing profiles are calculated for 8 channel phased array loading with longitudinal flexural wave modes L(n2) at a frequency of 60 kHz. The focused displacement profiles in the coated pipe are

illustrated in Figure 6-11. In Figure 6-11 the focusing profile using the coated pipe focusing parameter is plotted with blue dashed line and the focusing profile using the focusing parameter calculated from the bare 8 in. schedule 40 steel pipe is plotted with red dash-dot line. It can be seen from Figure 6-11 that using the coated pipe focusing parameters provides an increase in displacement amplitude at the focal position compared to using the bare pipe focusing parameters. The focused displacement amplitude of using coated pipe parameters is 0.67, whereas the focused displacement amplitude of using bare pipe parameters is 0.40. Therefore, the increase in displacement amplitude is approximately 67%.

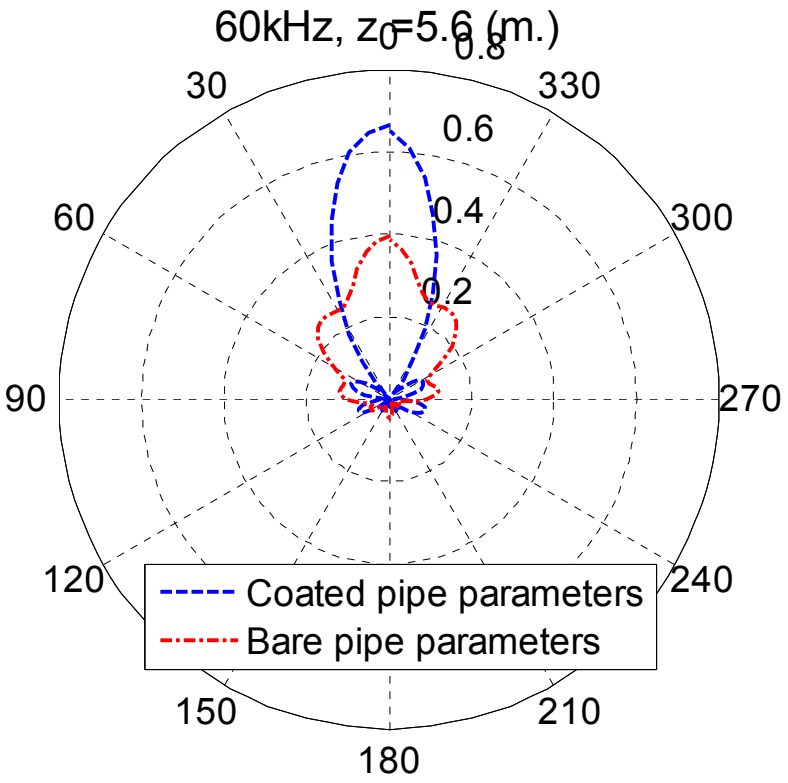

Figure 6-11: Theoretical calculation of the focused displacement profiles in an 8 in. schedule 40 steel pipe coated with 1.5 mm. bitumastic 50 coating. Focused profile using coated pipe parameters: blue dashed line; focused profile using bare pipe parameter: red dash-dot line.

In building the model, the whole cylindrical structure is first constructed. The cylinder is then partitioned into two sections, one pipe section and one coating section, as illustrated in Figure 6-12. In the modeling, the loading area is defined at the edge for convenience. The partition for the 8 channel loading is also shown in Figure 6-12. The loading is in axial direction denoted by arrows in orange. The structure is meshed with the maximum length of the elements being less than one-eighth of the wavelength. The time steps in the calculation can be automatically decided by ABAQUS. If chosen manually, the time steps should be at least several times less than the period of the input

signal and less than the time ultrasonic wave propagates from one end of the element to the other end.

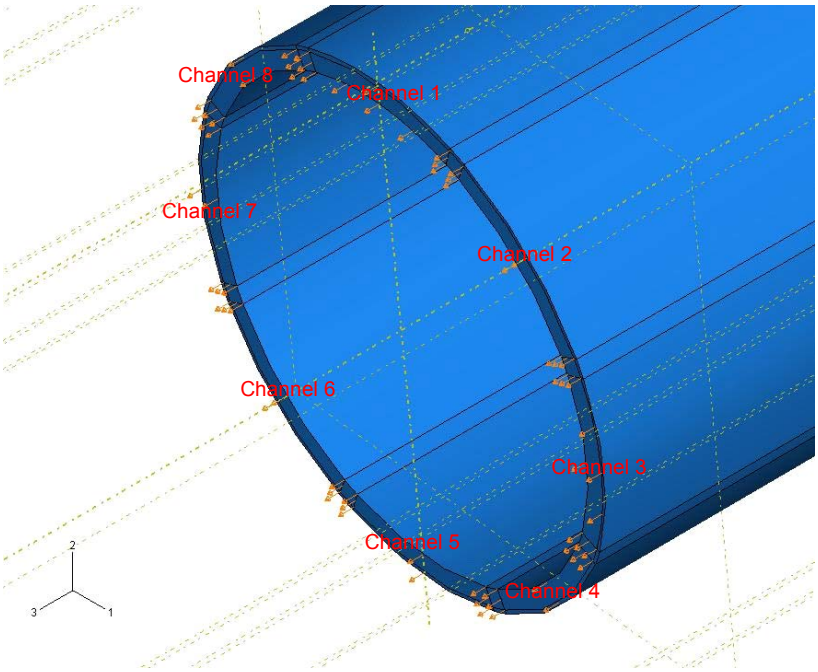

Figure 6-12: Illustration of the coated pipe configuration for FEM modeling purpose.

Luo et al. [2007] used finite elements to model guided wave focusing in coated pipes using bare pipe focusing parameters. They selected longitudinal waves to focus in a 10 in. schedule 40 steel pipe with two different coatings (Mereco 303 epoxy and bitumastic 50). It is shown that for most of the cases he modeled, focusing parameters calculated based on bare pipes were able to focus in coated pipes too. The viscoelastic material property in his model was approximated by a single damping factor introduced from the complex elastic modulus and the material was defined as elastic. In fact, the viscoelastic material had different attenuation on shear and volumetric behavior, which are represented by the complex longitudinal velocity $C_L^*(\omega)$ (Eq. 6.22) and the complex shear velocity $C_S^*(\omega)$ (Eq. 6.23), as have been used in our SAFE calculation.

$$C_L^*(\omega) = \frac{1}{C_L(\omega) + i\frac{\alpha_L(\omega)}{\omega}} \quad 6.22$$

$$C_S^*(\omega) = \frac{1}{C_S(\omega) + i\frac{\alpha_S(\omega)}{\omega}} \quad 6.23$$

Here, $C_L(\omega)$ and $C_S(\omega)$ are the bulk longitudinal and shear velocity in the viscoelastic material. $\alpha_L(\omega)$ and $\alpha_S(\omega)$ are the attenuation associated with longitudinal and shear waves respectively. These parameters can all be frequency dependent. However, in many ultrasonic applications, $C_L(\omega)$, $C_S(\omega)$, $\frac{\alpha_L(\omega)}{\omega}$, and $\frac{\alpha_S(\omega)}{\omega}$ are measured to be almost constant [Barshinger 2004].

The complex longitudinal and shear velocities can be converted into complex shear modulus $G^*(\omega)$ and complex bulk modulus $K^*(\omega)$ via Eq. 6.24 and Eq. 6.25 respectively.

$$G^*(\omega) = \rho[C_S^*(\omega)]^2 \quad 6.24$$

$$K^*(\omega) = \rho[C_L^*(\omega)]^2 - \frac{4}{3}\rho[C_S^*(\omega)]^2 \quad 6.25$$

ρ is the material density. The complex shear of the bulk moduli can be written as

$$G^*(\omega) = G'(\omega) + G''(\omega) \quad 6.26$$

$$K^*(\omega) = K'(\omega) + K''(\omega) \quad 6.27$$

where $G'(\omega)$ and $G''(\omega)$ are the real and imaginary parts of the complex shear modulus; $K'(\omega)$ and $K''(\omega)$ are the real and imaginary parts of the complex bulk modulus. $G'(\omega)$,

$G''(\omega)$, $K'(\omega)$, and $K''(\omega)$ can be converted to the long term shear modulus $G(t)\big|_{t=\infty}$ and the long term bulk modulus $K(t)\big|_{t=\infty}$ by [Christensen 1981]

$$G'(0) = G(t)\big|_{t=\infty} = G(\infty), \tag{6.28}$$

$$K'(0) = K(t)\big|_{t=\infty} = K(\infty). \tag{6.29}$$

The long term Young's modulus and Poisson's ratio can be calculated from the long term shear modulus $G(\infty)$ and bulk modulus $K(\infty)$. The long term Young's modulus and Poisson's ratio are input into ABAQUS to give the definition of the long term behavior of the viscoelastic material [ABAQUS Analysis User's Manual version 6.5]. The other variables that need to be input into ABAQUS to give the definition of viscoelastic behavior in frequency domain are $\omega R(g^*)$, $\omega I(g^*)$, $\omega R(k^*)$, $\omega I(k^*)$, which can be calculated from the following

$$\omega R(g^*) = G''(\omega) / G(\infty) \tag{6.30}$$

$$\omega I(g^*) = 1 - G'(\omega) / G(\infty) \tag{6.31}$$

$$\omega R(k^*) = K''(\omega) / K(\infty) \tag{6.32}$$

$$\omega I(k^*) = 1 - K'(\omega) / K(\infty) \tag{6.33}$$

In our modeling, the finite element computation is conducted in time domain. Therefore, the viscoelastic material properties in frequency domain will be converted into the time domain by ABAQUS via a Prony series approximation before the computation [ABAQUS Analysis User's Manual version 6.5].

The ABAQUS modeling results are shown in Figure 6-13 and Figure 6-14. The predetermined focal distance is pointed out by arrows in both figures. Figure 6-13 shows

the waves sent out from the left end of the coated pipe. A 6 cycle pulse is used as the driving signal. The bare pipe focusing parameters are used in the upper plot, while the coated pipe focusing parameters are used in the lower plot. The upper plot in Figure 6-14 shows the static shot of waves at the focal distance in the coated pipe using bare pipe focusing parameters. The lower one is the static shot of wave focusing in the coated pipe using coated pipe focusing parameters. The focal position is indicated by the arrows in the figure. The color scale shows the displacement magnitude of the wave field in the coated pipe. As can be seen from the figure, both sets of focusing parameters work. However, the focused wave displacement magnitude in the upper static shot is much smaller than that in the lower one. The maximum focused displacement magnitude for the bare pipe parameters is found to be 3.6×10^{-7}, while the maximum focused displacement magnitude using the coated pipe parameters is 5.3×10^{-7}. The displacement input amplitude of the ABAQUS model is 1×10^{-6} for amplitude factor 1. The improvement in the focused displacement amplitude is about 47%.

Table 6-5: Comparison of focused amplitudes between theoretical calculation and ABAQUS modeling driven by a **6** cycle pulse.

Focused amplitudes	**Theoretical calculation**	**ABAQUS modeling (6 cycles)**	**Difference between theory and model**
Coated pipe parameters	0.67	0.53	26%
Bare pipe parameters	0.40	0.36	11%

The difference in focused amplitudes between the theoretical calculations in Figure 6-11 and ABAQUS modeling is summarized in Table 6-5. It can be observed that the focused displacement amplitudes in the FE modeling are smaller than the theoretical

values. This difference is possibly caused by two reasons. First, the viscoelastic material properties are converted from frequency domain to time domain in the FE computation. In the conversion, approximately 10 terms are used in the Prony series. The truncation of the number of terms may lead to difference in the results. Second and more importantly, in our theoretical calculation, continuous waves at a single frequency are used. Therefore, all of the generated flexural modes in the theoretical calculations are continuous waves. However, in our modeling, the driving signal is a 6-cycle hanning windowed sinusoidal signal. This frequency bandwidth of such a signal will result in wave dispersion after propagating some distance. In other words, the generated flexural modes are not continuous waves anymore and will eventually separate from each other given a long enough propagation distance, because they all have different speeds. This dispersion will affect the focusing results. The dispersed part of the waves are of much smaller displacement amplitudes compared to the focused ones and are hidden in the figure by setting a threshold in the color scale in order to obtain a better view of the focused waves.

To make sure dispersion is the reason that makes the focal amplitudes in the FE modeling less than those predicted by theories (Table 6-5), another FE model is constructed. The coated pipe configuration is the same. However, this time it is driven by a 12-cycle hanning windowed sinusoidal signal. The focused amplitudes driven by a 12 cycle pulse are compared with the theoretical calculation in Table 6-6. It can be seen that the focused amplitudes are enhanced compared to those in the FE model driven by a 6 cycle pulse. The difference between the FE modeling and theoretical predictions for both bare pipe and coated pipe focusing parameters are of only 5% difference for a 12 cycle driving signal. This difference is majorly caused by the material properties mentioned in

the previous paragraph. The FE modeling provides us excellent verification to the theories and can be taken as a convenient numerical experiment.

Table 6-6: Comparison of focused amplitudes between theoretical calculation and ABAQUS modeling driven by a **12** cycle pulse.

Focused amplitudes	**Theoretical calculation**	**ABAQUS modeling (12 cycles)**	**Difference between theory and model**
Coated pipe parameters	0.67	0.70	4.5%
Bare pipe parameters	0.40	0.42	5.0%

Figure 6-13: The waves sent out from the end of the left pipe by using a **6** cycle driving signal. FE modeling of guided wave focusing in a coated pipe using bare pipe parameters (upper) and coated pipe parameters. Pipe size: 8 in. schedule 40 steel. Coating: 1.5-mm bitumastic 50. The designed focal distance is 5.6 m. 8 channel longitudinal focusing is used.

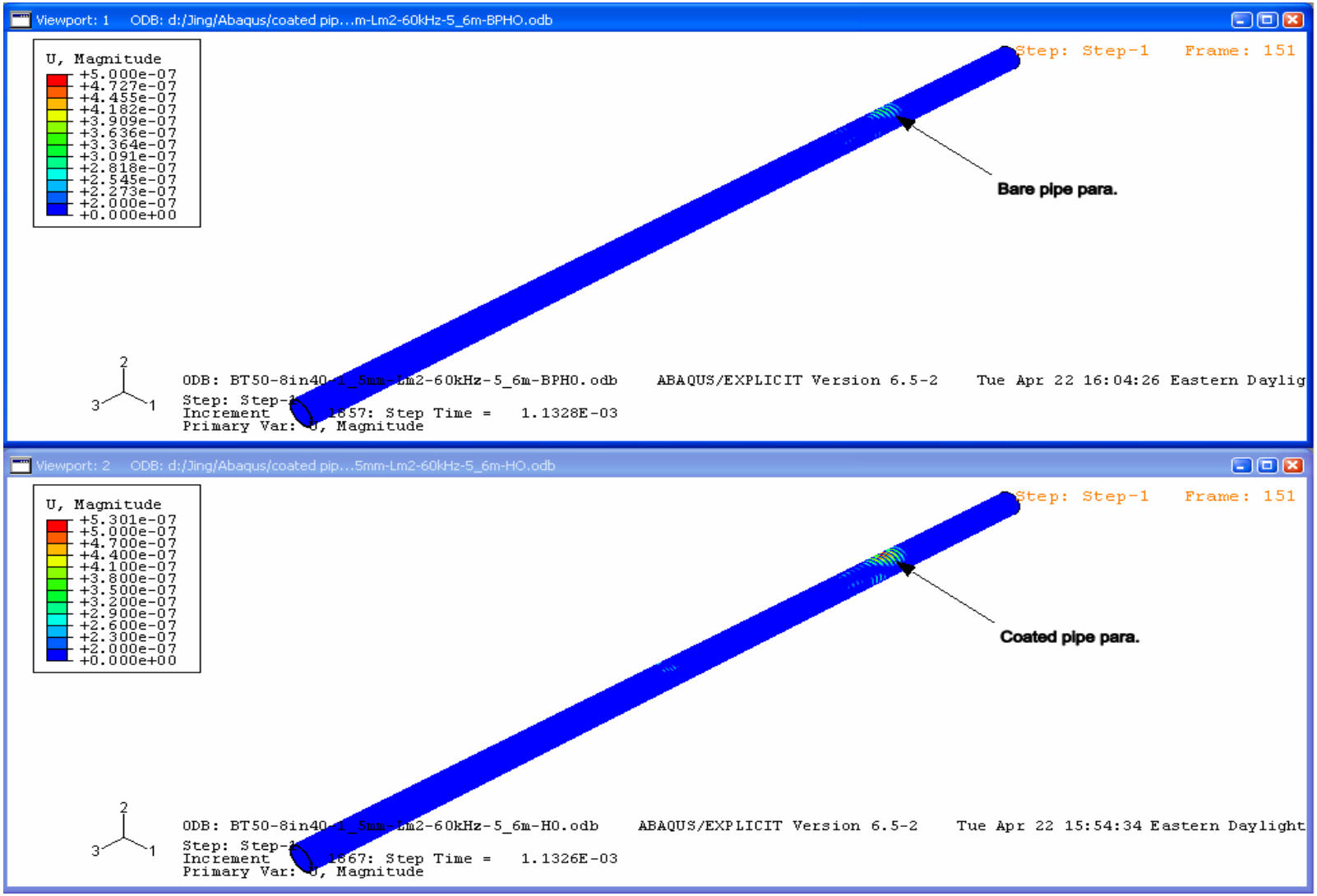

Figure 6-14: The focused wave packages for a **6** cycle driving signal. FE modeling of guided wave focusing in a coated pipe using bare pipe parameters (upper) and coated pipe parameters. Pipe size: 8 in. schedule 40 steel. Coating: 1.5-mm bitumastic 50. The designed focal distance is 5.6 m. 8 channel longitudinal focusing is used.

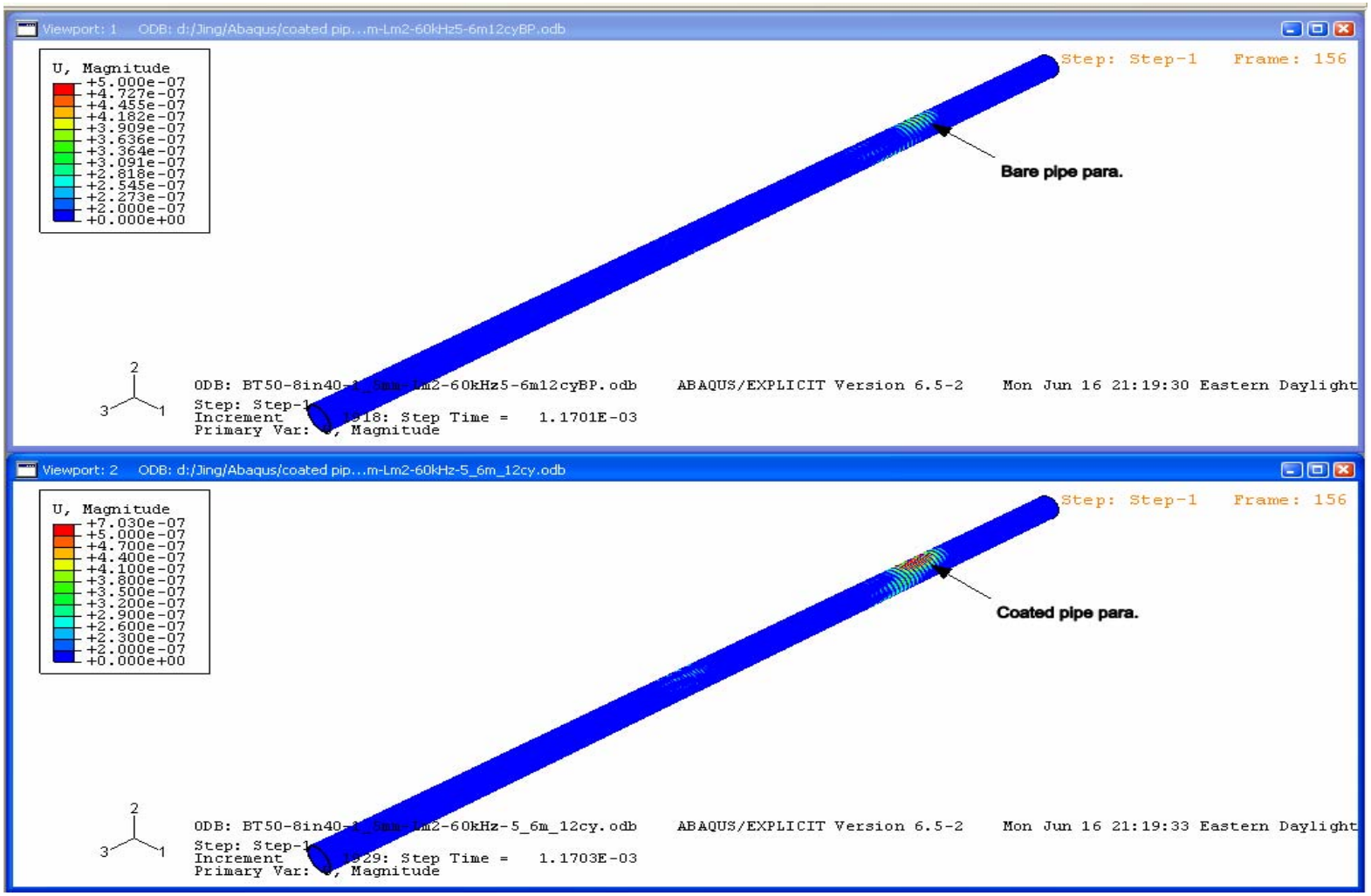

Figure 6-15: The focused wave packages for a **12** cycle driving signal. FE modeling of guided wave focusing in a coated pipe using bare pipe parameters (upper) and coated pipe parameters. Pipe size: 8 in. schedule 40 steel. Coating: 1.5-mm bitumastic 50. The designed focal distance is 5.6 m. 8 channel longitudinal focusing is used.

6.4 Summary

This chapter tackles the guided wave source influence problem in multilayered hollow cylindrical structures containing viscoelastic materials. The excited guided wave field of a specific source loading is composed of multiple normal modes. These normal modes are the characteristic solutions of the viscoelastic multilayered hollow cylinder. The amplitude factor of each generated normal mode is computed by the Normal Mode Expansion (NME) technique. By superimposing the generated normal modes with their corresponding amplitude factors, the total excited guided wave field is obtained.

The focusing computation in viscoelastic multilayered hollow cylinders is handled in the same way as that in a single layered elastic hollow cylinder [Li, et al., 2002]. Based on the displacement amplitude angular profile obtained from the source influence calculation, a deconvolution algorithm is incorporated to provide the amplitude factors and time delays to achieve guided wave focusing in multilayered pipes using a phased array.

Since the whole derivation from dispersion curves to focus computation is general and applicable in either single-layered or multilayered cylinders. The derivation based on the SAFE method is first implemented to calculate the dispersion curve values, the focusing parameters, and angular profiles in a single layered hollow cylinder. The results are quantitatively compared with the previous calculation of a single layered hollow cylinder based on a pure analytical method [Li, et al., 2002]. Excellent agreement is achieved between the two methods for both longitudinal flexural waves and torsional

flexural waves. The largest difference in phase velocity for the two methods is less than 0.01%. The comparison further validates the derivation based on the SAFE method.

The calculation is then carried out on multilayered hollow cylinders with viscoelastic materials. Considering that, in applications, most pipes are coated with viscoelastic materials for protection purpose, the focused profiles in a coated pipe by using coated pipe focusing parameters and its corresponding bare pipe parameters are compared. It is revealed that the bare pipe focusing parameters focus effectively under the circumstances where low frequency and thin coating are used. When the coating gets thicker, using bare pipe focusing parameters in a coated pipe can fail. In this situation, the coated pipe focusing parameters must be used.

Finally, a finite element model in ABAQUS is built to visualize the difference in focused energy by using coated pipe focusing parameters and the corresponding bare pipe focusing parameters in a pipe with relatively thick coating. The results show that the coated pipe parameters focus much better than the bare pipe parameters as have been predicted in the theoretical calculations.

Chapter 7

Experimental results

The theories of guided wave propagation and focusing in multilayered hollow cylinders have now been developed through a combination of Semi-Analytical Finite Element (SAFE) modeling and an analytical derivation of modal orthogonality as well as source influence. Finite element modeling in Abaqus is also performed to visualize the focusing process in the time domain and to verify our theoretical calculations. Since the generation of guided wave focusing parameters in coated pipe is based on the dispersion curves, wave structures, modal orthogonality, and source influence calculations, it would be beneficial to conduct experiments to verify the coated pipe focusing parameters and to further validate our theories from the dispersion curves to focusing calculation. In the following, the coated pipe focusing experimental methodology, experiment process, and results will be discussed in detail.

7.1 Synthetic focusing in pipes

To better understand the guided wave synthetic focusing in pipes, let us start with the ultrasonic bulk wave phased-array focusing. Two focusing methods are commonly used in bulk wave phased-array focusing. One is the real-time phased-array bulk wave focusing. The other is the synthetic bulk wave focusing, which is often referred to as Synthetic Aperture Focusing Technique (SAFT) [Chiao, et al., 1994]. In the real-time

phased-array bulk wave focusing technique, the time delays are input into each transducer in the phased array. Then, the signals are excited with different time delays from the transducers in the phased array, these ultrasonic signals will form constructive interference at the focal region or direction is created, while destructive interference at other regions or directions. In synthetic bulk wave focusing, the signal is transmitted from each of the transducers without any time delay and received by a set of transducers. All the received signals are collected and put into a post processing scheme, where the time delays needed for focusing at different regions are compensated.

Similar to bulk wave focusing, guided wave focusing in pipes can be realized both in real time and in post processing. For real-time guided wave focusing in pipes, appropriate amplitude factors (voltage levels) and time delays are applied to different channels in the phased array. The generated guided wave modes then form a constructive interference at the predetermined focal position, as described in our bare and coated pipe focusing calculations. For guided waves, the synthetic focusing used in our experiments, the signal is sent from each channel and received from all the channels without any added time delay and voltage control. For a 4-channel array, the signal is sent from channel 1 and received by all 4 channels. The process is then repeated from channel 2 to 4. In this way, 16 (4×4) signals will be obtained for a 4-channel phased array. The time delays and amplitude factors are then applied to the 16 received signals in post processing.

As can be expected, the signals transmitted from different channels will arrive at the defect with different phases and amplitudes. The difference in phases and amplitudes needs to be compensated in the synthetic focusing. On the other hand, any signal scattered from the defect will also arrive at the 4 channels with different phases and

amplitudes. The difference in phases and amplitudes upon receiving is associated with the displacement angular profile of the defect, which is unknown. The defect can be visualized as a source also. In our synthetic focusing, the angular profile of the defect is assumed to be approximately the same as the angular profile of a single channel. Therefore, the same amplitudes and time delays can be compensated in the receiving part as that done to the sending part. This forms exactly a convolution process which is the reverse process of the deconvolution algorithm used in the focusing parameter calculation. The convolution process for guided wave synthetic focusing is further illustrated in Figure 7-1.

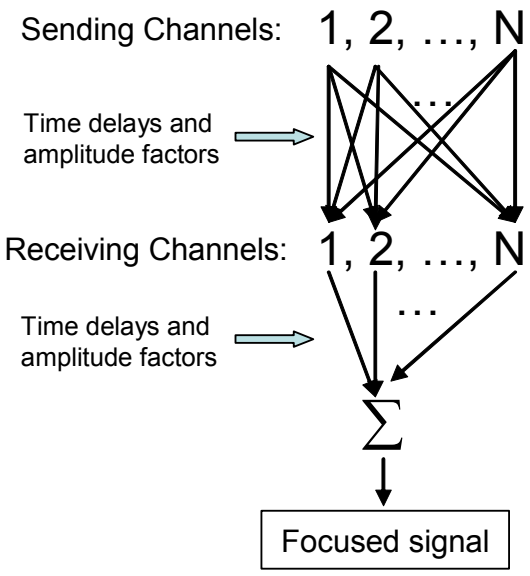

Figure 7-1: Guided wave synthetic focusing process, where N is the total number of channels.

7.2 Experiment setup

The system employed in the synthetic focusing experiments is the Power Focus system made by FBS Inc. As shown in Figure 7-2, a customized portable data acquisition system is used with software designed to control signal transmission and receiving. The guided wave phased array is wrapped around the circumference of the pipe. The phased array contains two rings of transducers, one for signal transmission, and the other for receiving. Each of the two rings is composed of 12 approximately equally spaced piezoelectric transducers. Each ring is also segmented into 4 channels with 3 transducers distributed in each channel. During experiments, the phased array is kept in tight contact with the pipe by pressure. The operative frequency range of the phased array is from 70 kHz to 140 kHz. The synthetic focusing experiment is carried out from 70 kHz to 140 kHz for every 5 kHz increment. In the following, only the experiment results for frequencies 75 kHz and 80 kHz will be discussed in detail because both theoretical calculation and experimental results reveal that the focusing effect is the strongest for these two frequencies.

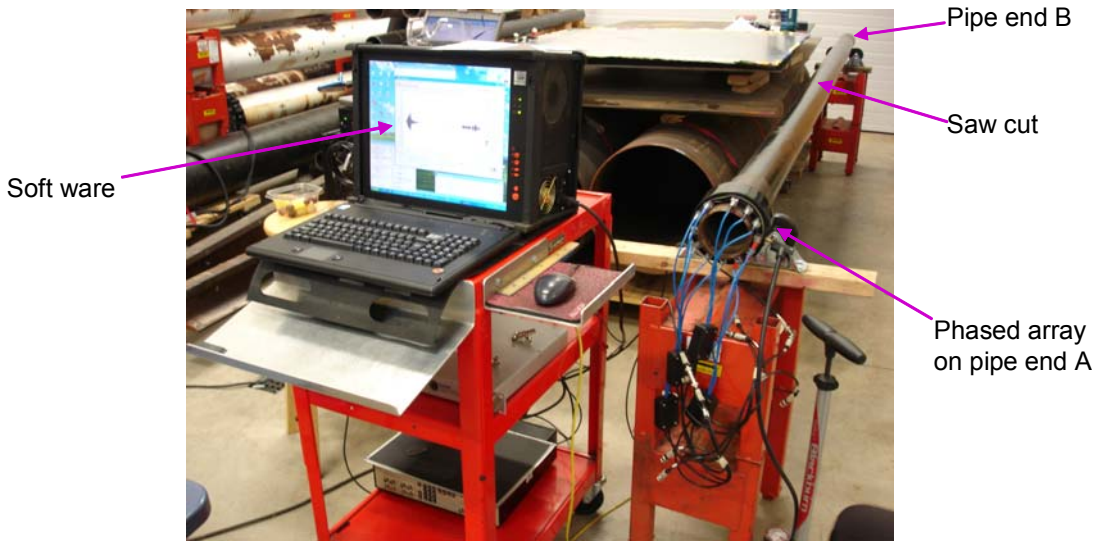

Figure 7-2: Guided wave synthetic focusing pipe experiment setup.

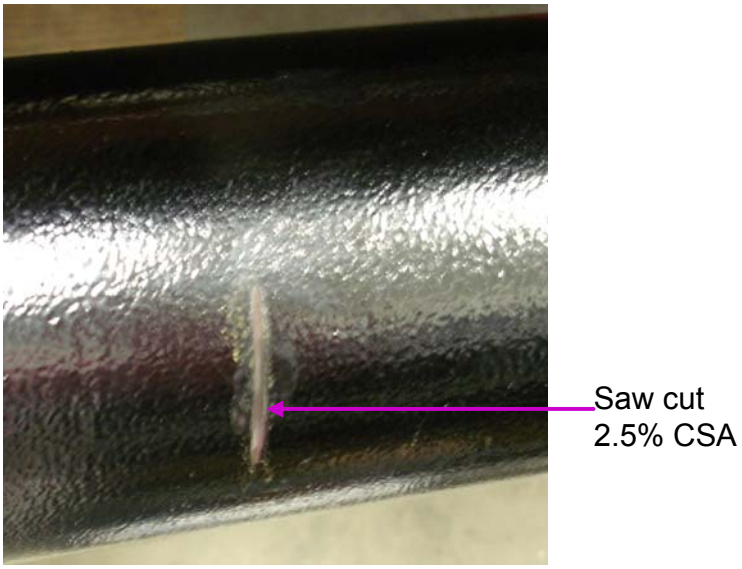

Figure 7-3: Saw cut with 2.5% cross sectional area (CSA)

The pipe utilized in the experiment is a 4 in. schedule 40 steel pipe coated with 0.4 mm bitumastic 50. The properties of bitumastic 50 are listed in Table 5-2. Since bitumastic 50 is a very attenuative material, the coating is made relatively thin to reduce

attenuation to the guided wave signal. The pipe is 15 ft. long. A saw cut is machined on the pipe for the experiment with a cross sectional area of 2.5% as shown in Figure 7-3. The saw cut is 6 ft. and 6 in. from pipe end A.

7.3 Coated pipe synthetic focusing experimental results

Before conducting experiments, theoretical calculations are first performed. The transducer array is placed at 1.4 in to pipe end A. Therefore, the saw cut location is approximately 6.4 ft from the transducer array. The focused profiles of the torsional waves T(n,1) at the saw cut location using bare pipe focusing parameters and coated pipe focusing parameters are shown in Figure 7-4. The frequency is chosen to be 80 kHz, because at this frequency, the focused profiles appear to have small side lobes at the focal distance. It can be seen from Figure 7-4 that the focused profiles obtained from using both coated pipe focusing parameters and the corresponding bare pipe focusing parameters are almost the same. This is not surprising, since the coating is relatively thin and the operating frequency is low. The difference between the dispersion curves for a coated pipe and uncoated bare pipe are small at low frequency, but it increases with an increase in frequency.

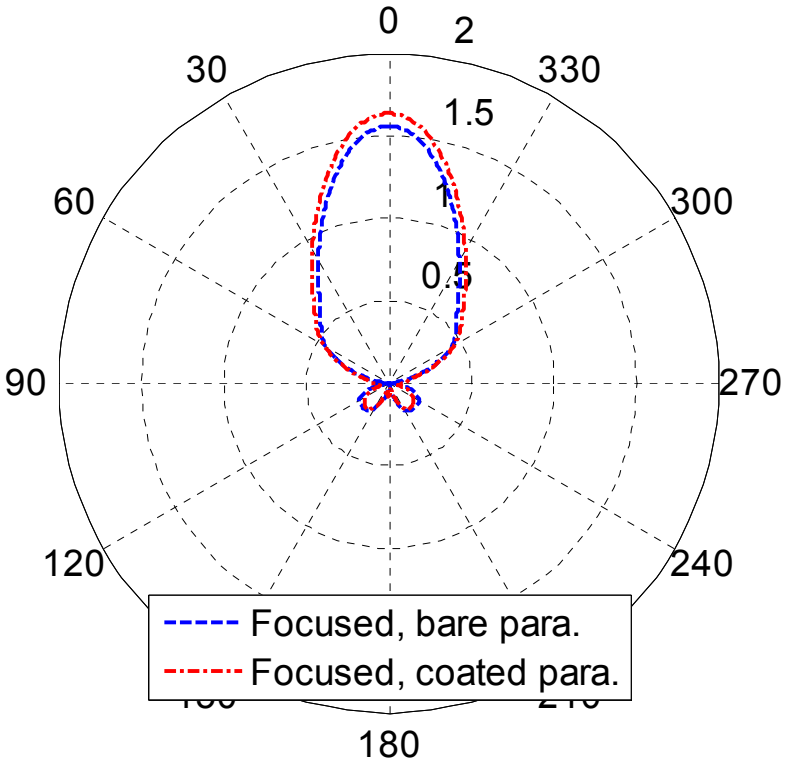

Figure 7-4: Torsional waves T(n,1) focusing in a 4 in. schedule 40 steel pipe coated with 0.4-mm bitumastic 50 at a frequency of 80 kHz. The focal distance is 6.4 ft counting from the location of the transducer array to the saw cut.

The amplitude factors and time delays for focusing at the saw cut in the coated pipe and the corresponding bare pipe are listed in Table 7-1. It can be observed from Table 7-1 that the focusing parameters calculated from the coated pipe and the corresponding bare pipe are close to each other. The difference between the two sets of amplitude factors is small. The two sets of time delays should be compared by taking into account that the period of a tone burst signal at 80 kHz is 12.5μs. Therefore, the difference between the two sets of time delays is approximately 4.7μs for each channel, which means that the two sets of time delays are actually close to each other. The

similarity between the two sets of parameters also reveals that the coating is relatively thin.

Table 7-1: Coated pipe focusing parameters: Torsional waves T(n,1) focusing at 6.4 ft. in a 4 in. schedule 40 steel pipe coated with 0.4 mm. bitumastic 50 at a frequency of 80 kHz. Bare pipe focusing parameters: Torsional waves T(n,1) focusing at 6.4 ft. in a 4 in. schedule 40 steel pipe at a frequency of 80 kHz.

	Bare pipe focusing parameters		Coated pipe focusing parameters	
Channel index	Amplitude factor	Time delay (μs)	Amplitude factor	Time delay (μs)
1	1.000	1.775	1.000	6.405
2	0.655	9.572	0.640	1.782
3	0.748	8.227	0.596	0.474
4	0.655	9.572	0.640	1.782

Before the saw cut is machined, data were taken on the coated pipe with no defect to serve as a reference. The transducer array is placed at 1.4 in to pipe end A as shown in Figure 7-2. The transmitted signal is a 6 cycle hanning windowed tone burst at 80 kHz center frequency. 16 data sets were taken for the 4-channel synthetic focusing. The 4-channel guided wave synthetic focusing was then performed using both the coated pipe parameters and bare pipe parameters listed in Table 7-1. The corresponding focusing results are plotted in Figure 7-5 and Figure 7-6 respectively. The zero distance in each figure denotes pipe end A. In each of the two figures, four waveforms are plotted. Each waveform represents the synthetic focused result at the focal angle written to the upper right hand side of the waveform. The focal zone is indicated by two vertical red lines covering from 6.5 ft. to 7.5 ft on every waveform in Figure 7-5 and Figure 7-6. The focal zone is approximately 1 ft. long. It can be observed from both figures that there is no clear echo within the focal zone in any of the waveforms, which means that there is no

defect detected within the focal region using either set of the focusing parameters in Table 7-1.

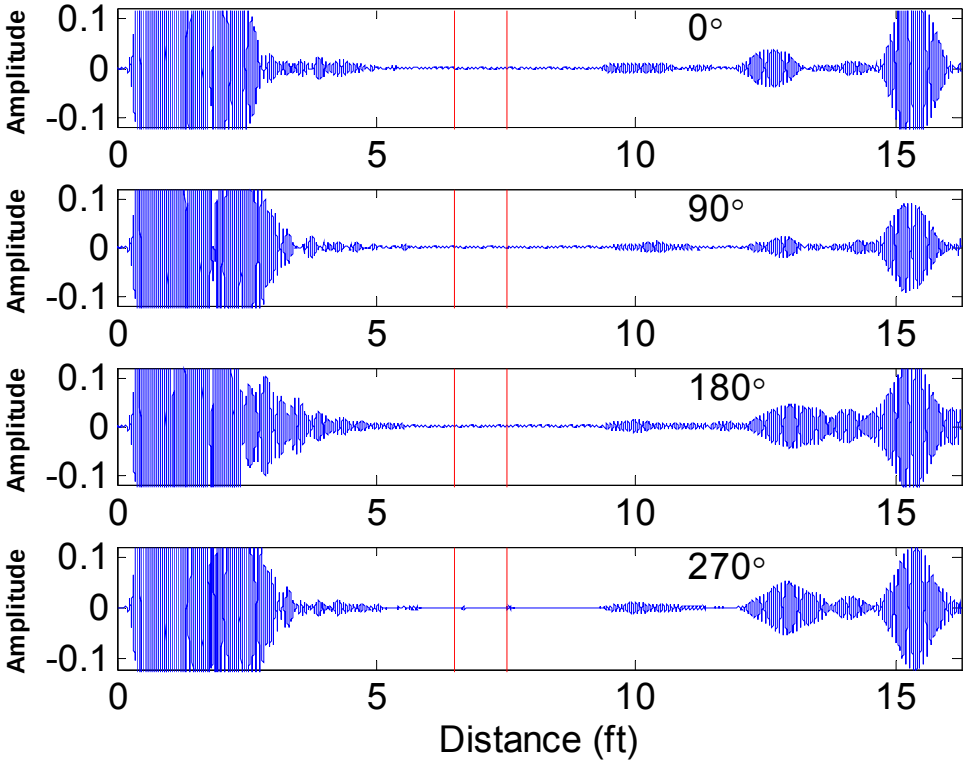

Figure 7-5: Guided wave synthetic focusing results in the coated pipe with no defect. **Coated** pipe focusing parameters in Table 7-1 are used. No defect is found in the focal region.

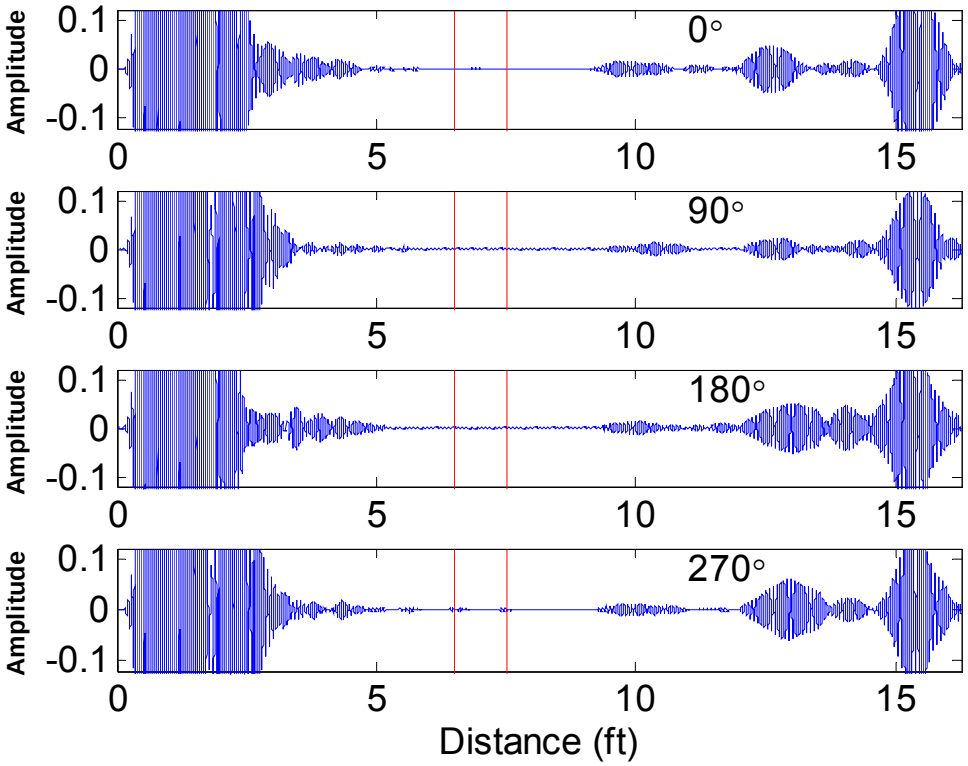

Figure 7-6: Guided wave synthetic focusing results in the coated pipe with no defect. **Bare** pipe focusing parameters in Table 7-1 are used. No defect is found in the focal region.

The above procedure is repeated to collect data after the saw cut is made. The other experiment settings remain to be the same. The saw cut is centered at 0º, which corresponds to the location of channel 1. The synthetic focusing results at the saw cut distance using coated pipe parameters and bare pipe parameters are shown in Figure 7-7 and Figure 7-8 respectively. An echo shows up in the focal zone of the focused waveform at 0º for both Figure 7-7 and Figure 7-8. However, there are no echoes in the focal zones of the focused waveforms at the other focal angles. This means there is only one defect in the focal range and is located at 0º. No significant difference is observed between the focused defect echo amplitudes of the two cases, as have been indicated from the

theoretical calculations in Figure 7-4. The defect axial location is determined to be 6.5 ft. according to the arrival time of the echoes in both figures. These experimental results verify that the coated pipe focusing parameters focus well at the designed location and correctly located the defect both axially and circumferentially. It is also confirmed that the bare pipe parameters work effectively in cases where thin coatings are used.

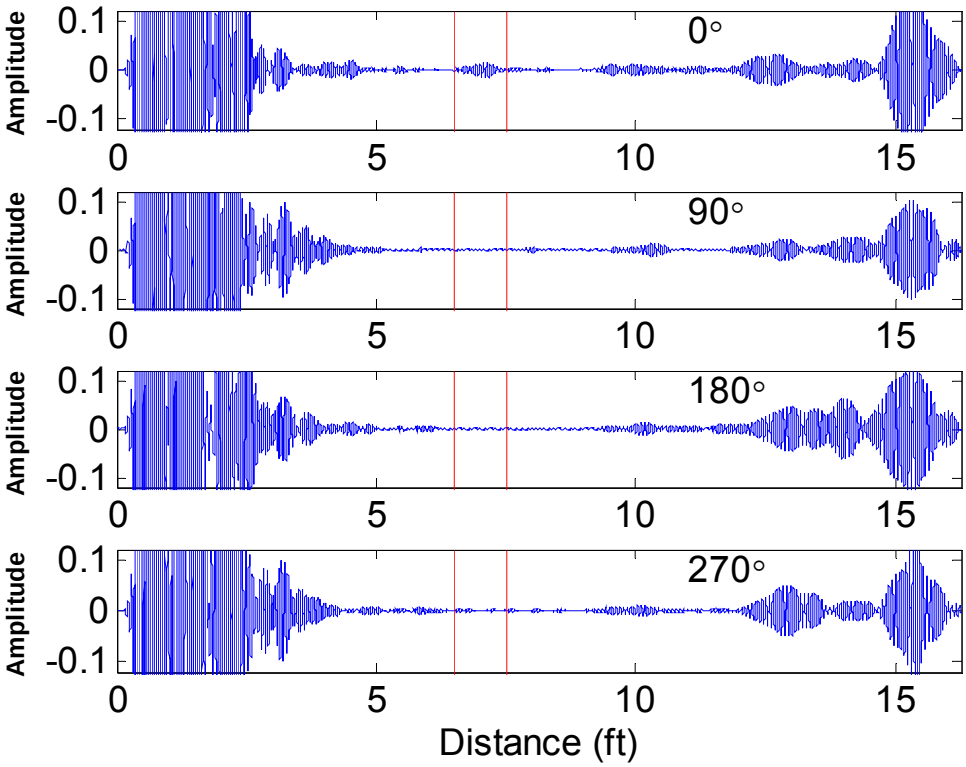

Figure 7-7: Guided wave synthetic focusing results at the saw cut distance in the coated pipe. **Coated** pipe focusing parameters in Table 7-1 are used. A defect is found at 0°.

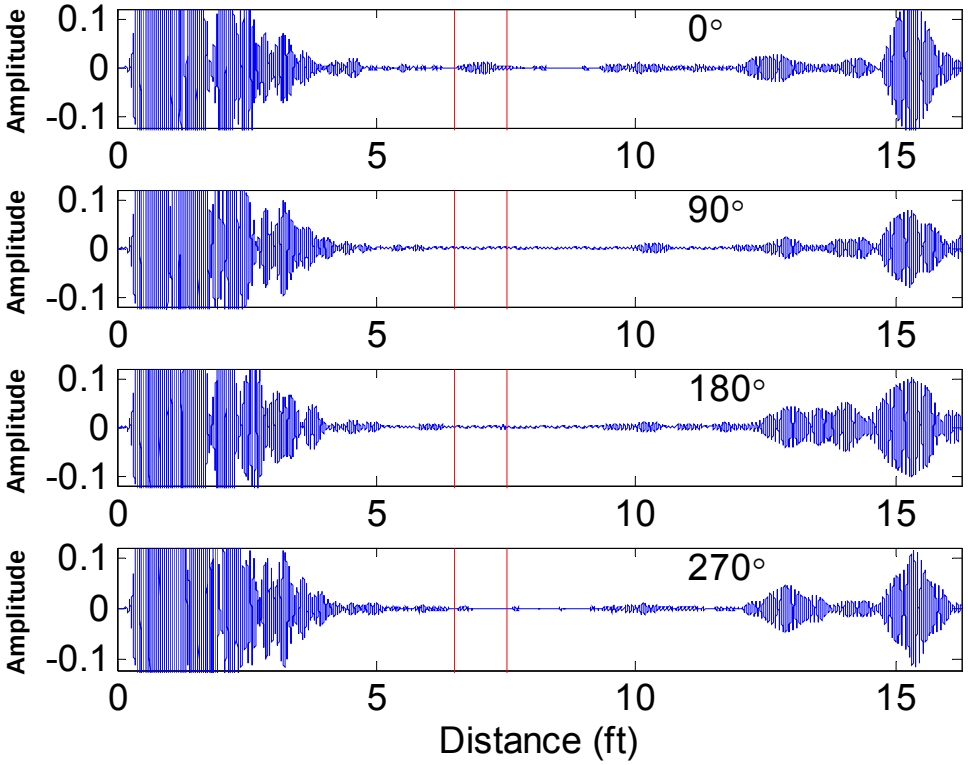

Figure 7-8: Guided wave synthetic focusing results at the saw cut distance in the coated pipe. **Bare** pipe focusing parameters in Table 7-1 are used. A defect is found at 0°.

Other frequencies have also been performed in the experiment. Similar synthetic focusing results are obtained. The experimental results agree well with the theoretical predictions using coated pipe focusing parameters. For brevity, only the synthetic focusing results at 75 kHz using the coated pipe focusing parameters are shown in Figure 7-9. Repeated tests show that the difference between different test results is less than 5%.

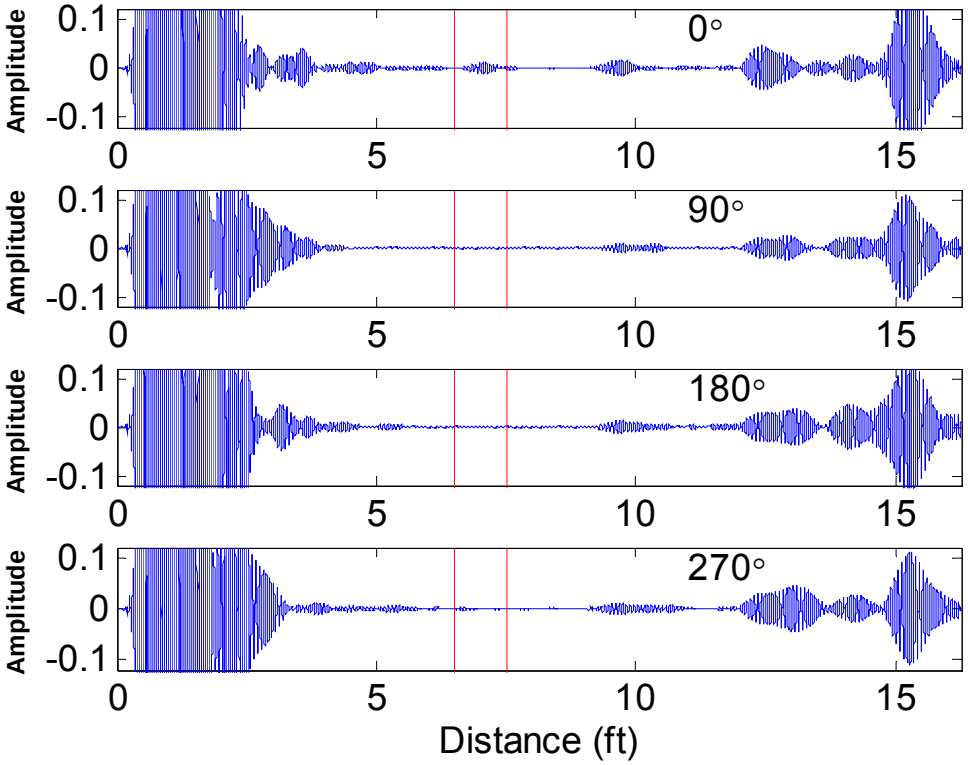

Figure 7-9: Guided wave synthetic focusing results at the saw cut distance in the coated pipe at a frequency of 75 kHz. **Coated** pipe focusing parameters, calculated according to the coated pipe size and properties in the experiment, are used.

7.4 Summary

This chapter discussed the concept and process of guided wave synthetic focusing in pipes. Experiments are performed to validate the theoretical calculation of coated pipe focusing parameters. A saw cut is machined on a 4 in. schedule 40 steel pipe coated with 0.4 mm bitumastic 50. Experiments are conducted and data are taken to synthetically focus at the saw cut location by applying both coated pipe focusing parameters and the bare pipe focusing parameters. The experimental synthetic focusing results show that the

coated pipe parameters work very well and the focused results match that predicted by the theories. Since the focusing parameters are computed on the basis of dispersion curves, wave structures, and source influence calculation, the validation of coated pipe parameters also indirectly verifies the calculation on dispersion curves, wave structures, orthogonality, and source influence. The axial and circumferential locations of the saw cut are accurately determined in the experiment. It is also verified both theoretically and experimentally that the bare pipe focusing parameters also focus effectively for pipes with thin coatings.

Chapter 8

Concluding remarks

8.1 Final Summary

The purpose of the work in this thesis is to seek better understanding and full exploration of all of the possible guided wave modes including axisymmetric and flexural that can propagate in multilayered hollow cylindrical structures with elastic or viscoelastic materials. The work is initially motivated by the need to conduct nondestructive evaluation and testing on pipes with viscoelastic coatings. Viscoelastic coatings are widely used on pipes for various protection purposes. The existence of these viscoelastic coatings changes the guided wave modal behavior in pipes. Due to the fact that mode control is a critical issue in guided wave nondestructive evaluation, the investigation of guided wave propagation characteristics in such viscoelastic multilayered hollow cylindrical structures becomes indispensable and imperative.

The thesis started by an introduction to the previous work on guided wave propagation [Gazis 1959], source influence [Ditri, et al., 1992] and focusing technique [Li, et al., 2002] in elastic bare pipes. Following these theories, the guided wave focusing technique was applied and extended to pipe imaging and circumferential sizing in the thesis. Guided wave long range pipe imaging is realized in the field test by scanning the pipe both circumferentially and axially with a focused guided wave beam. The imaging process was discussed and the final pipe image was displayed. All defects were

successfully found in the field test. After that, guided waves were used to focus at 44 equally spaced locations around the pipe for defect circumferential size determination. The amplitude of the reflected wave from the defect is recorded for each focal angle to form a reflection profile. Based on the focused displacement amplitude profiles, the reflected energy profiles are calculated for defect with different circumferential lengths. These theoretical reflection profiles are then compared with the experimental ones to infer the circumferential length of the defect. The results are encouraging.

The above investigation shows that guided wave focusing not only provides better penetration power than axisymmetric inspection but also produces direct circumferential resolution. However, with the existence of viscoelastic coatings on pipes, the performance of bare pipe focusing technique in coated pipe is uncertain. Therefore, the goal is to analyze the guided wave mode behavior in coated pipes and develop the focusing technique suitable for coated pipes.

To tackle the problem of wave propagation in free viscoelastic multilayered hollow cylinders, the Semi-Analytical Finite Element (SAFE) method is adopted. The multilayered cylindrical waveguide is discretized in the radial direction, while analytical representations are adopted in the circumferential and axial directions. A suitable SAFE formulation is then developed based on the conservation of energy. A complex stiffness matrix is used to describe the viscoelastic behavior of the materials. After mathematical manipulation, a characteristic equation is assembled. The eigenvalues of the characteristic equation are the complex wave numbers for the selected frequency. The phase velocity and attenuation dispersion curves are obtained from the real and imaginary parts of the

complex wave numbers respectively. The eigenvectors of the equation provide the wave structures of the corresponding guided modes.

An important issue regarding the dispersion curves solved by the SAFE method is that the eigenvalue arrangement appears to be different for different frequencies. This makes it difficult to trace modal behavior along the frequency. It also makes it inconvenient to select the most excited guided wave modes under certain source loading. To resolve this problem, an orthogonality relation is developed based on the real reciprocity relation. This orthogonality relation is applicable to both elastic and viscoelastic, single-layered and multilayered hollow cylinders. The orthogonality relation is then implemented to sort the guided modes. The mode sorting enables the dispersion curves to be plotted using different colors and line styles for different modes and makes it clear how the modes evolve with frequency in the dispersion curves. The successful mode sorting also serves as verification to the theoretical derivation and the corresponding numerical computation.

The axisymmetric modes obtained from the SAFE method were compared with that have been developed by Barshinger [2004] using an analytical matrix method. Excellent agreement was obtained between the dispersion curves given by the two different methods. In addition to axisymmetric modes, the SAFE formulation also provides the flexural mode solution. Flexural modes can be generated wherever the feature is non-axisymmetric in a pipe. They play an important role in source influence, focusing, and defect sizing. The wave structures are also calculated and compared to those in bare pipes. The cross sectional deformations of different guided wave modes are also plotted to help understand the guided wave modal behavior.

The source influence in a viscoelastic multilayered hollow cylinder is analyzed in a similar way as that in a single-layered elastic hollow cylinder. The generated guided wave field is composed of multiple guided wave modes. Normal mode expansion (NME) technique is employed to calculate the amplitude factors of the generated normal modes. The difference between the source influences in multilayered viscoelastic and single-layered elastic hollow cylinders is that the derivation of amplitude factor for multilayered viscoelastic hollow cylinders are based on the real reciprocity relation, while the complex reciprocity relation is used for single-layered elastic hollow cylinders. Plus, to develop the orthogonality and source influence in multilayered viscoelastic hollow cylinders, the continuity conditions for displacement and normal stress components must be used in addition to the traction free surface at the inner and outer surfaces of the cylinders.

Finally, the deconvolution algorithm is adopted to calculate the focusing parameters in viscoelastic multilayered hollow cylinders. To validate the algorithm, the whole formulation based on SAFE method is first used to compute the focusing parameters in a bare pipe. The results are compared to the focusing parameters obtained from Jian Li's program, which is written based on the analytical matrix method. The bare pipe focusing parameters calculated from both methods match completely for both longitudinal and torsional mode focusing. Next, displacement amplitude angular profiles of partial source influence on coated and bare pipes are illustrated. Detailed comparisons are given to the focused profiles in coated pipes using coated pipe focusing parameters and bare pipe focusing parameters. It is found that the focusing ability of using bare pipe focusing parameters in coated pipes in general decreases with the increase of frequency and coating thickness. To visualize and verify the difference in focusing using coated

pipe and bare pipe focusing parameters, a finite element model is constructed with Abaqus. The process of modeling pipes with viscoelastic coatings is given in detail. The viscoelastic property definition in Abaqus is used to implement the complex stiffness matrix that has been used in our theoretical calculations. The modeling results clearly demonstrate the case where the focused amplitude of using the coated pipe focusing parameters can be significant higher than using the corresponding bare pipe focusing parameters in the coated pipe. The modeling results also match the theoretical calculations very well.

To further verify the algorithm developed in the thesis, a guided wave synthetic focusing experiment is designed. The concept and process of guided wave synthetic focusing in pipes are introduced. The experiment is then conducted on a steel pipe coated with 0.4 mm. bitumastic 50. A saw cut is machined in the coated pipe at a predetermined distance. The theoretical calculation shows that the focusing effect using both coated pipe focusing parameters and the corresponding bare pipe focusing parameters should be similar in this case. 16 sets of data are taken for the 4-channel synthetic focusing at the machined saw cut in the experiment. The bare pipe focusing parameters and coated pipe focusing parameters are applied to these experimental data in post processing. The experimental synthetic focusing results show that both the coated pipe parameters and the bare pipe parameters focus well in this case. The focused side lobes are small and the focusing amplitudes are similar. The experimental results agree well with the theoretical calculations.

8.2 Contributions

The major contributions of this thesis that go beyond previous work on guided wave propagation in hollow cylinders can be summarized as follows:

1. The establishment of long range guided wave pipe imaging in field tests based on guided wave focusing technique in bare pipes.
2. The development of guided wave circumferential sizing technique in pipes by using guided wave focusing technique in bare pipes.
3. The development of a suitable Semi-Analytical Finite Element (SAFE) theory targeting on solving the guided wave propagation problem including dispersion curves, wave structures, stress distribution, etc. in multilayered hollow cylinders containing viscoelastic materials.
4. The development of an analytical 3-Dimensional orthogonality relation that is generally valid in both elastic and viscoelastic multilayered hollow cylinders.
5. The development of a mode sorting process that successfully separates all the modes in the dispersion curves based on the orthogonality relation developed in hollow cylinders.
6. The development of source influence to calculate the phase velocity spectrum, i.e. the excitation amplitude factors of all guided modes in multilayered viscoelastic hollow cylinders.
7. The implementation of the focusing algorithm into the multilayered viscoelastic hollow cylinders in order to realize guided wave focusing in viscoelastic coated pipes.

8. The design of Finite Element Modeling in Abaqus to visualize the guided wave focusing process in coated pipes and verify the theories.
9. Synthetic focusing experiments are performed to verify the coated pipe focusing parameters and validate the guided wave focusing theories in viscoelastic coated pipes.
10. The full decomposition of the scattered guided wave field from defects in pipes based on the modal orthogonality existing in hollow cylinders (please see Appendix A for detail).

8.3 Future Directions

Based on the understanding of guided wave mode characteristics to a focusing technique in viscoelastic multilayered hollow cylinders, the possible future directions are listed in the following.

1. Defect sizing can be carried out in both bare and coated pipes. The orthogonality relation developed in this thesis can be employed to decompose all the normal modes (Normal Mode Decomposition, NMD) scattered from a defect. The NMD technique reveals the axisymmetric and flexural modes and their corresponding amplitudes scattered from a defect. The theoretical development of the NMD has been accomplished based on Abaqus finite element models (please refer to Appendix 1 for detail).
2. Following the above decomposition of a scattered wave field, a pattern recognition program can be adopted to determine the defect size based on the pattern of the

decomposed normal modes. A large number of finite element models can be built in Abaqus with defects of different sizes and shapes. The NMD results of these models with known defects can be used to train the pattern recognition program. After the pattern recognition program is trained, experiments can be done to verify the results under certain wave incidence.

3. Coating delamination is a common problem in application. Based on the coated pipe dispersion curves, guided wave modes with dominant displacement in the coating layer can be chosen to help detect coating delamination.
4. The bonding can also be modeled by assuming an additional layer between the coating and the pipe. The properties of the bonding layer can be selected to represent the bonding condition between the coating and the pipe. In this way, bonding degradation can be analyzed.
5. Suitable guided wave tools should be designed according to different application goals on the basis of guided wave mode characteristics in pipe NDE.
6. Wave propagation characteristics beyond a pipe bend or elbow can be explored. Based on the wave propagation characteristics, defect size analysis base on normal mode expansion beyond a pipe elbow can be carried out.

References

Abaqus Analysis User's Manual, version 6.5.

Achenbach, J. D., "Mathematical modeling for quantitative ultrasonics," *Nondestr. Test. Eval.*, vol. 9, pp. 363-377, 1992.

Alleyne, D. and Cawley, P., "A two-dimensional Fourier transform method for the measurement of propagating multimode signals", JASA, 89(3), 1991, p.1159.

Alleyne, D. N. and P. Cawley, "Optimization of lamb waves inspection techniques," NDT & E Int., vol. 25, pp. 11-22, 1992.

Alleyne, D. N., Lowe, M. J. S., and Cawley, P., "The reflection of guided waves from circumferential notches in pipes," *ASME J. Appl. Mech.*, vol. 65, pp. 635-641, 1998.

Auld, B. A., "Acoustic Fields and Waves in Solids," Krieger, Malabar, FL, 1990.

Barshinger, J. N. and Rose, J. L. (2004). "Guided wave propagation in an elastic hollow cylinder coated with a viscoelastic material," IEEE Trans. Ultrason. Ferroelectr. Freq. Control 51, 1547-1556.

Bartoli, I., Marzani, A., Lanza di Scalea, F., and Viola, E. (2006). "Modeling wave propagation in damped waveguides of arbitrary cross-section," J. Sound. Vibr. 295, 685-707.

Beard, M. D. and Lowe, M. J. S. (2003)."Non-destructive testing of rock bolts using guided ultrasonic waves," International Journal of Rock Mechanics & Mining Sciences 40, 527-536.

Carriere, R. and Moses, R. L., "High Resolution Radar Target Modeling Using a Modified Prony Estimator," IEEE Trans. Antennas Propogat., vol.40, pp. 13-18, January 1992.

Cawley, P., Lowe, M., Simonetti, F., Chevalier, C., "The variation of reflection coefficient of extensional guided waves in pipes from defects as a function of defect depth, axial extent, circumferential extent and frequency," Journal of Mechanical Engineering Science, vol. 216, pp. 1131-41, 2002.

Chan, C. W. and Cawley, P., "Lamb waves in highly attenuative plastic plates," J. Acoust. Soc. Am., vol.104(2), 1998, pp.874-881.

Cheung, Y.K. *Finite Strip Method in Structural Mechanics*, Pergamon Press, Oxford, 1976.

Cho, Y. and Rose, J. L., "A boundary element solution for a mode conversion study on the edge reflection of lamb waves," *J. Acoust. Soc. Am*., vol. 99, pp. 2097-2109, 1996.

Christensen, R. M., Theoty of Viscoelasticity, second edition, Academic Press, New York, 1982.

Cordell, J. L., "The latest developments in pipeline pigging world-wide," *Pipes and Pipelines International*, vol. 39, pp. 16-21, 1994.

Damljanović, V. and Weaver, R. L. (2004). “Forced response of a cylindrical waveguide with simulation of the wavenumber extraction problem,” J. Acoust. Soc. Am. **115**, 1582-1591.

Davies, J., Simonetti, F., Lowe, M., and Cawley, P. (2005). “Review of synthetically focused guided wave imaging techniques with application to defect sizing,” *Review of Quantitative Nondestructive Evaluation*, Vol. 25, Edited by D. O. Thompson and D. E. Chimenti.

Chiao, Richard Y. and Thomas, Lewis J., “Analytic evaluation of sampled aperture ultrasonic imaging techniques for NDE,” *IEEE Transactions on Ultrasonics, Ferroelectrics, and Frequency Control*, Vol. 41, No. 4, 1994, p. 484.

Demma, A., The interaction of guided waves with discontinuities in structures, Ph.D Thesis, 2003.

Demma, A., Cawley, P., and Lowe, M., “The effect of bends on the propagation of guided waves in pipes,” *Transactions of the ASME*, vol. 127, pp. 328, 2005.

Ditri, J. J. and Rose, J. L., "Excitation of guided elastic wave modes in hollow cylinders by applied surface tractions," *J. Appl. Phys.,* **72**(7), 2589–2597, 1992.

Ditri, J. J., Rose, J. L., and Chen, G., “Mode selection criteria for defect optimization using lamb waves,” In D. O. Thompson and D. E. Chimenti, editors, *Review of Progress in Quantitative NDE*, pp. 2109-2115, Plenum Press, New York, 1992.

Ditri, J. J., Rose, J. L., and Pilarski, A., “Generation of guided waves in hollow cylinders by wedge and comb type transducers,” In D. O. Thompson and D. E. Chimenti, editors, *Review of Progress in Quantitative NDE*, pp. 211-218, Plenum Press, New York, 1993.

Ditri, J. J., “Utilization of Guided Elastic Waves for the Characterization of Circumferential Cracks in Hollow Cylinders,” *J. Acoust. Soc. Am.,* vol. 96, pp. 3769–3775, 1994a.

Ditri, J. J. and Rose, J. L., “Excitation of guided waves in generally anisotropic layers using finite sources,” *J. Appl. Mech.*, vol. 61, pp. 330-338, 1994b.

Dong, S., and Nelson, R. (1972). “On natural vibrations and waves in laminated orthotropic plates,” J. Appl. Mech. 39, 739-745.

Elvira-Segura, L. (2000). “Acoustic wave dispersion in a cylindrical elastic tube filled with a viscous liquid,” Ultrasonics, vol.37, pp.537-547.

Engan, Helge E. (**1998**) “Torsional wave scattering from a diameter step in a rod,” J. Acoust. Soc. Am., **104**(4), 2015-2024.

Eisenhart, L., 1934, “Separable systems in Euclidean 3-space,” *Phys. Rev.*, vol. 45, pp. 427-428.

Fraser, W. B. (**1976**). “Orthogonality relation for the Rayleigh-Lamb modes of vibration of a plate,” J. Acoust. Soc. Am., **59**(1), 215-216.

Gazis, D. C., "Three dimensional investigation of the propagation of waves in hollow circular cylinders. I. Analytical foundation," *J. Acoust. Soc. Am.,* vol. 31, pp. 568–573, 1959.

Gazis, D. C., "Three dimensional investigation of the propagation of waves in hollow circular cylinders. II. Numerical Results," *J. Acoust. Soc. Am.,* vol. 31, pp. 573–578, 1959.

Ghosh, J., "Longitudinal vibrations of a hollow cylinder", *Bulletin of the Calcutta Mathematical Society,* vol. 14, pp. 31-40, 1923.

Ghosh, T., Kundu, T., and Karpur, P., "Efficient use of lamb modes for detecting defects in large plates," *Ultrasonics*, vol. 36, pp. 791-801, 1998.

Giurgiutiu, V.; Bao, J. (2004) "Embedded-Ultrasonics Structural Radar for In-Situ Structural Health Monitoring of Thin-Wall Structures", *Structural Health Monitoring – an International Journal*, Vol. 3, Number 2, 2004, pp. 121-140.

Graff, K.F. *Wave Motion in Elastic Solids*. New York: Dover Publications, 1991.

Hayashi, T. and Rose, J. L., "Guided wave simulation and visualization by a semianalytical finite element method," *Material Evaluation*, vol. 61, pp. 75-79, 2003.

Hayashi, Takahiro, Song, Won-Joon, and Rose, J.L., "Guided wave dispersion curves for a bar with an arbitrary cross-section, a rod and rail example," *Ultrasonics*, vol. 41, pp. 175-183, 2003.

Hayashi, Takahiro and Murase, Morimasa (2005). "Defect imaging with guided waves in a pipe," JASA, vol.117, pp. 2134-2140.

Hayashi, T., Kawashima, K., Sun, Z., and Rose, J. L. (2005). "Guided wave propagation mechaninics across a pipe elbow," Trans. ASME. **127**, 322-327.

Ing, R.K., Fink, M. (1998). "Time-reversed Lamb waves," *IEEE Transactions on Ultrasonics, Ferroelectrics, and Frequency Control*, vol. 45, no. 4, pp.1032-1043.

Kil, H.-G., Jarzynski, J., and Berthelot, Y. H., "Wave decomposition of the vibration of a cylindrical shell with an automated scanning laser vibrometer," J. Acoust. Soc. Am., vol. 104(6), 1998, pp.3161-3168.

Kino, G. S. (**1978**). "The application of reciprocity theory to scattering of acoustic waves by flaws," J. Appl. Phys., **49**(6), 3190-3199.

Knopoff, L. (1964). "A matrix method for elastic wave problems," *Bull. Seism. Soc. Am.* **54**: 431-438.

Kolsky, H., *Stress waves in solids*. New York: Dover, 1963.

Koshiba, M., Hasegawa, H., and Suzuki, M., "Finite-element solution of horizontally polarized shear wave scattering in an elastic plate," *IEEE transactions on ultrasonics, ferro electrics and frequency control*, vol. 34, pp. 461-466, 1987.

Lamb, H. (1917). "On waves in an elastic plate", *Proc. Royal Soc. London*, A**93**: 114-128.

Li, J., and J. L. Rose, "Excitation and Propagation of Non-axisymmetric guided waves in a Hollow Cylinder*", J. Acoust. Soc. Am.***, 109**(2), 457-464, 2001.

Li, J., and J. L. Rose, "Implementing Guided Wave Mode Control by Use of a Phased Transducer Array", *IEEE Trans. Ultrason., Ferroelect., Freq. Contr.*, **49**(12), 1720-1729, 2001.

Li, J., and J. L. Rose, "Angular-profile tuning of guided waves in hollow cylinders using a circumferential phased array", *IEEE Trans. Ultrason., Ferroelect., Freq. Contr.*, **49**(12), 1720-1729, 2002.

Li, J. and Rose, J.L., "Natural beam focusing of non-axisymmetric guided waves in large-diameter pipes," Ultrasonics, vol. 44, pp. 35-45, 2006.

Lowe, M. J. (1995). "Matrix techniques for modeling ultrasonic waves in multilayered media," IEEE Trans. Ultrason. *Ferroelectr*. Freq. Control, 42, 525-542.

Luo, W., *Ultrasonic guided waves and wave scattering in viscoelastic coated hollow cylinders*, Ph.D Thesis, 2005.

Luo, W., Zhao, X., and Rose, J. L. (2005). "A guided wave plate experiment for a pipe", ASME Journal of Pressure Vessel Technology, 127, 345-350.

Luo, W. and Rose, J. L. (2007). "Phased array focusing with guided waves in a viscoelastic coated hollow cylinder," *J. Acoust. Soc. Am.*, vol.121(4), 1945-1955.

Ma, J., Simonetti, F., and Lowe, M. J. S. (2006). "Scattering of the fundamental torsional mode by an axisymmetric layer inside a pipe", J. Acoust. Soc.Am., 120, 1871-1880.

Mal., A., and S.-S. Lih. Characterisation of the elastic properties of composite interfaces by ultrasonic nde. In D. O. Thompson and D. E. Chimenti, editors, *Review of Progress in Quantitative NDE*, Plenum Press, New York, 1992.

Malvern, L. E., *Introduction to the mechanics of a continuous medium*. Englewood Cloffs, NJ: Prentice-Hall, 1969.

Moser, F., Jacobs, L., and Qu, J., "Modeling elastic wave propagation in waveguides with finite element method," *NDT & E Int.*, vol. 33, pp. 225-234, 1999.

Nayfeh, A. H. and Chimenti, D. E., "Propagation of guided waves in fluid-coupled plates of fibre-reinforced composite," *J. Acoust. Soc. Am.*, vol. 83, pp. 1736-1743, 1988.

Nelson, R.B., Dong, S.B., and Kalra, R.D. (1971) "Vibrations and waves in laminated orthotropic circular cylinders," J. Sound. Vibr. 18, 429-444.

Ong, P. S., Anderson, W. L., Cook, B. D., and Subramanyan, R., "A novel x-ray technique for inspection of steel pipes," *J. Nondestruct. Eval*, vol. 13, pp. 165-173, 1994.

Pavlakovic, B. N., Lowe, M. J. S., and Cawley, P. (2001). "High-frequency low-pass ultrasonic modes in embedded bars," Journal of Applied Mechanics, vol.68, pp.67-75.

Plotnikov, A., and Clapham, L., "Stress effects and magnetic nde methods for pipeline inspection: a study of interacting defects," *Insight*, vol. 44, pp. 74-78, 2002.

Pollard, H. F., *Sound waves in solids*, London: Pion Ltd, 1977.

Predoi, M. V., Castaings, M., Hosten, B., and Bacon, C., "Wave propagation along transversely periodic structures," J. Acoust. Soc. Am., vol. 121(4), 2007, pp.1935-1944.

Rayleigh, J. (1945). *The Theory of Sound*, Vol. I and II, Dover Publications, New York.

Rose, J. L. (1999). Ultrasonic Waves in solid Media, Cambridge University Press.

Shkerdin, G., and Glorieux, C. (**2004**). "Lamb mode conversion in a plate with a delamination", J. Acoust. Soc. Am. **116**, 2089-2100.

Shkerdin, G., and Glorieux, C. (**2005**). "Lamb mode conversion in an absorptive bi-layer with a delamination", J. Acoust. Soc. Am. **118**, 2253-2264.

Shorter, P. J. (2004). "Wave propagation and damping in linear viscoelastic laminates," *J. Acoust. Soc. Am.*, vol. 115(5), pp. 1917-1925.

Simonetti, F. (2004). "Lamb wave propagation in elastic plate coated with viscoelastic materials," J. Acoust. Soc. Am. **115**, 2041-2053.

Stoneley, R. (1924). "Elastic waves at the surface of separation of two solids," *Proc. Roy. Soc.* **106**: 416-428.

Sun, Y. S., Qu, M. X., Si, T. J., Lu, C. T., Zhou, X. Y., and Atherton D. L., "Improvement in remote-field eddy current probe structure," *Mater. Eval.*, vol. 50, pp. 237-250, 1992.

Sun, Z., L. Zhang, B.J. Gavigan, T. Hayashi, and J. L. Rose, "Ultrasonic flexural torsional guided wave pipe inspection potential", *ASME Proceedings of Pressure Vessel and Piping Division Conference*, PVP- **456**, 29-34, 2003.

Sun, Z. (2004). Phased array focusing wave mechanics in tubular structures, Ph.D Thesis, The Penn State Univ.

Sun, Z., L. Zhang, and J. L. Rose, "Flexural torsional guided wave mechanics and focusing in pipe", *ASME Journal of Pressure Vessel Technology*, vol.127, pp.471-478, 2005.

Thomson, W. T. (1950). "Transmission of elastic waves through a stratified solid medium." *J. Appl. Phys.* **21**: 89-93.

Viktorov, I. A. (1970) *Rayleigh and lamb waves*, Plenum Press, New York.

Vogt, T. Lowe, M. and Cawley, P. (**2003**) "The scattering of guided waves in partly embedded cylindrical structures", J. Acoust. Soc. Am., **113**(3), 1258-1272.

Wilcox, P. D., Dalton, R. P., Lowe, M. J. S., and Cawley, P., "Mode and transducer selection for long range lamb wave inspection," *Key Eng. Materials, Proc. DAMAS*, vol.34, pp. 152-161, 1999.

Wilcox, Paul D. (2003). "A rapid signal processing technique to remove the effect of dispersion from guided wave signals," *IEEE Transactions on Ultrasonics, Ferroelectrics, and Frequency Control*, Vol. 50, No. 4, p. 419.

Williamson, G. C. and Bohon, W. M., "Evaluation of ultrasonic intelligent pig performance: inherent technical problems as a pipeline inspection tool," *Pipes and Pipelines International*, vol. 39, pp. 29-34, 1994.

Zhang, L., *Guided wave focusing potential in hollow cylinders*, Ph.D Thesis, 2005.

Zhang, L., Rose, J. L., Avioli, M. J. and Mudge, P. J., "A natural focusing low frequency guided wave experiments for the detection of defects beyond elbows," *Transactions of the ASME, Journal of Pressure Vessel Technology*, Vol. 127, pp. 310-316, 2005.

Zhao, X. and Rose J. L., "Boundary element modeling for defect characterization potential in a wave guide," *International Journal of Solids Structures*, **40**, 2645-2658, 2003.

Zhong, W. X. and Williams, F. W. (1995). "On the direct solution of wave propagation for repetitive structures," *Journal of Sound and Vibration*, vol. 181(3), pp.485-501.

Zhu, W., "An FEM simulation for guided elastic wave generation and reflection in hollow cylinders with corrosion deects," Journal of Pressure Vessel Technology, vol. 124, pp. 108-17, 2002.

Zhuang, W., Shah, A. H., and Datta, S. K., "Axisymmetric guided wave scattering by cracks in welded steel pipes," *ASME J. Pressure Vessel Technol.*, vol. 119, pp. 401-406.

Appendix A

Defect wave scattering analysis by Normal Mode Decomposition

A.1 Introduction

Defect sizing has been a critical subject in Nondestructive Evaluation (NDE) for guiding the maintenance and replacement of pipelines. It has also been a challenging research area for the past few decades. Conventional bulk wave ultrasonic inspection of structures is conducted on a point-by-point basis. This makes the inspection time-consuming. Therefore, it is usually used where small areas need to be inspected. For long range and large area inspections, guided wave techniques are potentially more attractive than conventional bulk wave techniques. Guided wave energy is confined in wave guides, so there is less attenuation with guided wave propagation. As a result, guided waves can travel very long distances. Guided wave techniques are increasingly employed in pipe inspections because of reduced cost and efficiency.

Unlike bulk waves that contain only two modes, multiple modes exist at any given frequency for guided waves. The complexity regarding utilizing guided waves in defect sizing is the interpretation of the multiple guided wave modes scattered from the defect. Especially in pipes and cylinders, the existence of double infinite modes [Ditri, et al., 1992] makes the interpretation of the received signal even more difficult. Another issue is that most guided wave modes are dispersive, which means that different frequency components in the waveform travel at different phase and group velocities

along the propagation path. Consequently, the received signal will be distorted due to dispersion, which can make the received signal very different from the transmitted one. The dispersion effect makes signal interpretation become even more difficult.

Some good work has been done towards signal interpretation in defect analysis. Alleyne and Cawley [1991], for example, presented a 2-Dimensional Fourier transform method to separate the multiple guided wave modes propagating in a plate structure. In the 2-D Fourier transform method, a series of equally spaced receivers are located along the wave propagating path on the surface of the plate. The time domain waveforms from all of the receivers are converted into frequency domain by a Fourier transform in the time domain. Followed by the time domain Fourier transform, a second Fourier transform is conducted in the space domain according to the locations of the receivers. The results of the 2-D Fourier transform process are the amplitudes distributed in the wave number (k) and frequency (f) domain, which can be directly matched to the dispersion curve of the plate to measure the generated guided wave modes.

Another excellent effort for defect sizing in pipes is made by Hayashi and Murase [2005]. In this work, they used 8 sensors equally distributed in the circumference around the pipe. Based on the sinusoidal distributions of guided wave modes around the circumference of the pipe, they were able to decompose the guided wave modes with different circumferential orders. Then, they numerically back-propagated the decomposed guided wave modes and obtained the image of the defect. This method works well when there is only one guided wave mode group propagating in the pipe. It does not provide enough information on the existence of multiple propagating mode groups.

This work focuses on the full decomposition of guided wave modes scattered by a defect in a hollow cylinder. As pointed out in the thesis, the orthogonality relation exists in a wide variety of wave guides. Especially, the guided wave modes in single- or multi-layered hollow cylinders share the same orthogonality relation [Eq. 5.32]. Based on this orthogonality relation, a Normal Mode Decomposition (NMD) method will be used here to decompose the signal scattered by a defect into the doubly infinite guided wave modes in a hollow cylinder. FE modeling will be used as a numerical experiment to illustrate the NMD process in wave scattering analysis.

A.2 Normal Mode Decomposition in hollow cylinders

An 8 *in*. schedule 40 steel pipe with a notch defect is built into the FE model for NMD. The pipe schematic is shown in Figure A-1. The notch is 3 mm. wide. The depth of the notch is 50% through-wall thickness. The circumferential length of the notch is 45^{o}. In the FE model, axisymmetric longitudinal wave L(0,2) will be exited from pipe end B by imposing a uniform displacement in the *z* direction around the circumference of the pipe. The wave energy will be partially reflected when the generated wave impinges onto the defect. In order to make used of the orthogonality relations in the circumferential and axial directions, the receivers should be placed in both directions. The locations of the receivers are illustrated by yellow circles. A magnified view of the receiver distributions are shown in Figure A-2. The receiver locations are distributed evenly around the pipe circumference and along the axial direction of the pipe. As shown in

Figure A-2, 64 equally spaced rings of receivers are used in this FE modeling. There are 16 receiving locations equally spaced on each of these rings.

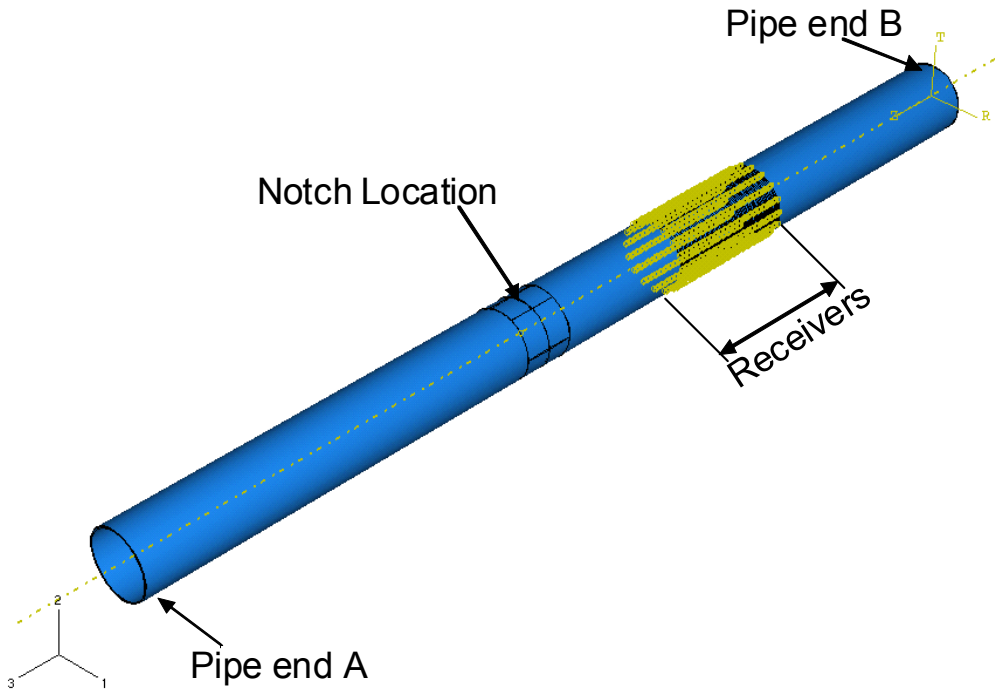

Figure A-1: Pipe schematic showing the distribution of a notch defect and receivers.

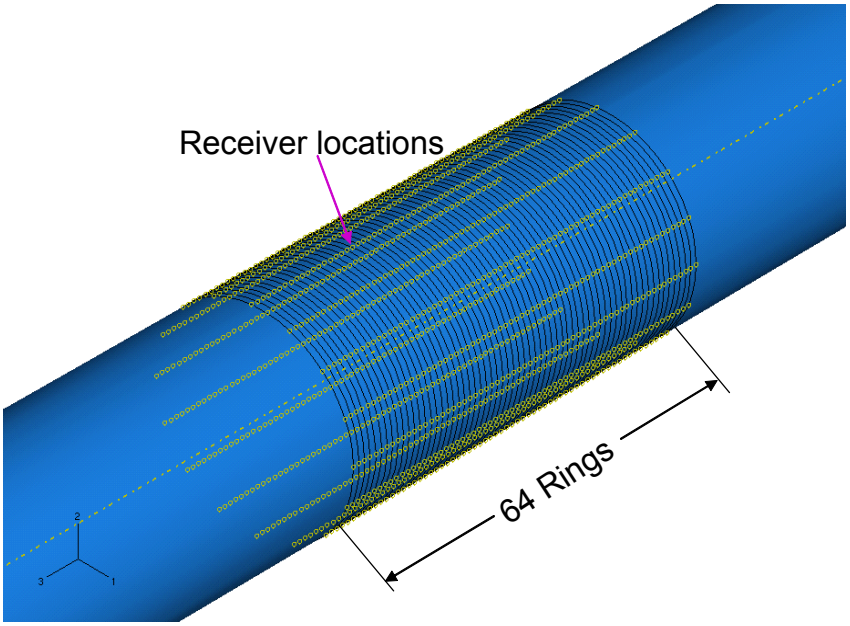

Figure A-2: A magnified view of the receiver distributions on the pipe.

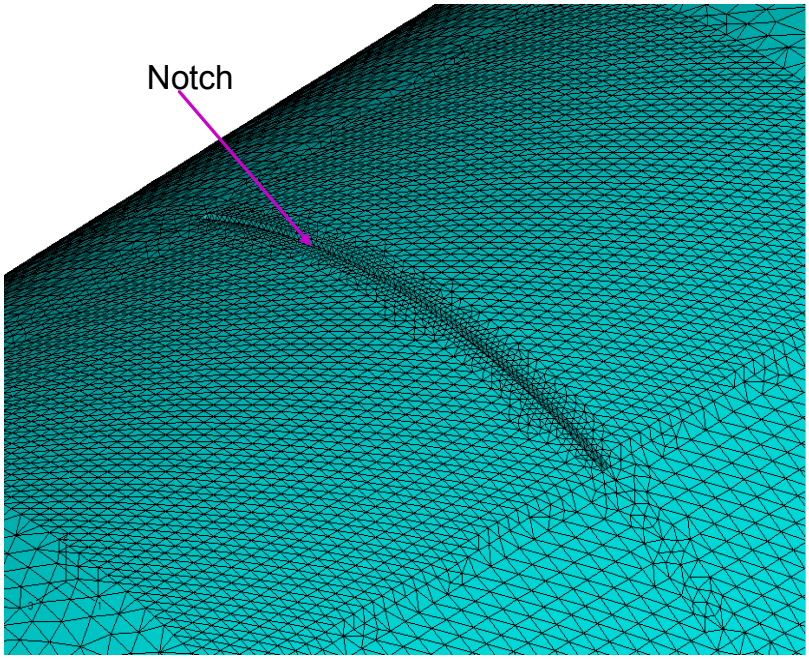

Figure A-3: A magnified view of the notch and the mesh.

A magnified view of the notch and the meshing in the FE model is shown in Figure A-3. The scattered waves from the defect will propagate through the receivers. Each of the receivers will receive a signal in time domain. These received signals are arranged according to their circumferential and axial locations as shown in Figure A-4**,** where θ and z represents the circumferential and axial location of the receivers; t is the time axis of the received signals. In this way, the received signals form a 3-dimensional data matrix. Considering that the normal modes propagating in cylinders have sinusoidal distributions in both circumferential and axial directions (Eq. 5.2**),** as well as in time domain. A 3-dimensional Fourier transform can be performed on the data matrix. By performing the 3-dimensional Fourier transform, the received time domain signals are entirely converted into the frequency domain, the axial location z and the circumferential location θ of the signals are converted into the wave number k and the circumferential order n respectively (Figure A-4**).** For each circumferential order n, the data in k-f domain are the decomposed guided wave modes. They can be compared to theoretical dispersion curves in measuring the scattered wave modes and their corresponding amplitudes.

Kil et al. [1998] employed a similar method for wave field decomposition in shells. They developed a laser vibrometer to scan axially and circumferentially around the pipe surface. A Fourier transform is then conducted on the received signals in the circumferential direction and time domain, while an extended Prony method is used to predict the wave numbers in the axial direction. The advantage of using the Prony method is that the imaginary part of wave number can be predicted also. This makes it suitable for analyzing the wave field in coated pipes. Another advantage of using the

extended Prony method is that the number of receiver points in the axial direction can be reduced. However, the wave number prediction results depends on the number of terms used in the Prony series and the number of rings used for receiving. The prediction results may be indefinite and deviate from the actual wave numbers in the existence of noise or given inappropriate number of terms in the Prony series [Carriere, et al., 1992]. In addition, the wave number prediction needs to be conducted for each frequency, which can be computationally costly if the excitation signal is wide band in frequency domain. Compared to the Prony method, the Fourier transform provides definite results and the computational cost is the same for signals with different frequency bandwidths. Kil et al. investigated the wave field exited by a piezoelectric shaker on a shell. In this study, we analyze the wave field scattered by a defect. In order to obtain more information on the dispersion curve, we would like the driven signal to cover a relatively wide frequency range. In the modeling, a 2-cycled tone burst is used as our driven signal to excite the axisymmetric wave mode L(0,2). Therefore, we use the 3-D Fourier transform to decompose the normal modes in the scattered wave field.

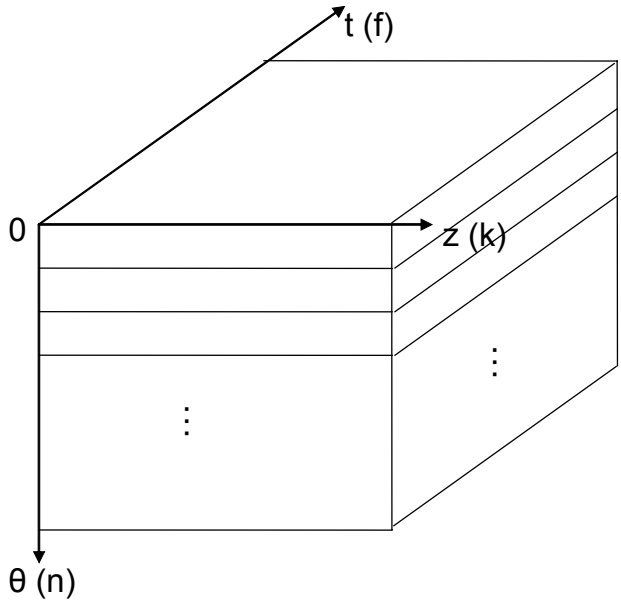

Figure A-4: The 3-dimensional data matrix of the received signal.

A.3 Results and discussions

A 2 cycle tone burst at a center frequency of 35 kHz is used as the driving signal in the FE modeling. The normal mode decomposition results from the scattered wave field generated by the notch are shown in Figures A-5 to A-13 for wave modes with different circumferential orders. The phase velocities of the decomposed normal modes are shown with their amplitudes in color scale in these figures. For comparison purpose, the theoretical phase velocity dispersion curves are superimposed in these figures as well. The theoretical phase velocity dispersion curves are calculated for the wave modes with circumferential orders from 0 to 16. The mode name is labeled accordingly for each theoretical phase velocity dispersion curve.

As can be noticed in Figures A-5 to A-12, the guided wave modes of two different circumferential orders are plotted in each figure. This is because signals are received from 16 locations around the circumference, which means that the maximum circumferential order that can be resolved after the mode decomposition is 8. However, guided wave circumferential orders can go from 0 to infinity. If the flexural modes with circumferential orders higher than 8 are generated by the defect, they will be superimposed to the lower order guided wave modes by aliasing. Therefore, the scattered wave modes with circumferential order 16 will be superimposed to those with circumferential order 0, modes with circumferential order 15 will then be superimposed to those with circumferential order 1, and so on. This aliasing effect can be clearly identified in Figures A-5 to A-13. It can also be observed that some flexural modes with circumferential orders higher than 16 have also been generated, especially for the L(n,2) mode group (for example, Figures A-6 to A-9**).**

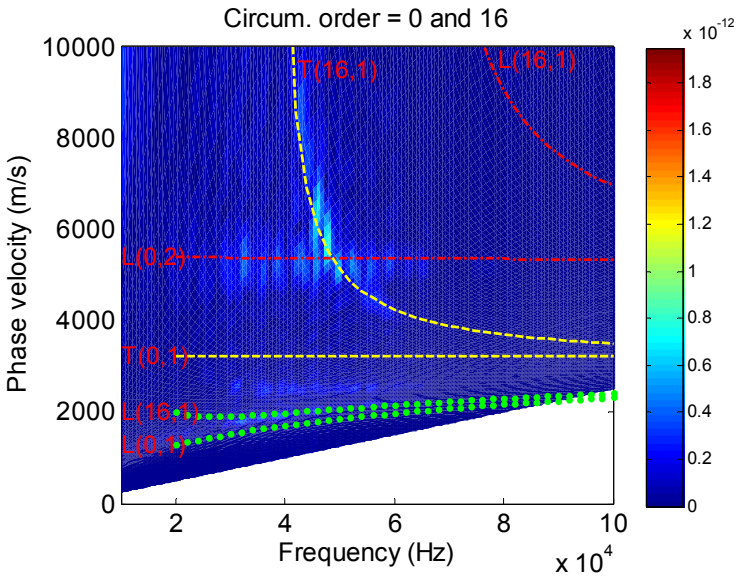

Figure A-5: Decomposed wave modes and the theoretical dispersion curves for circumferential orders 0 and 16.

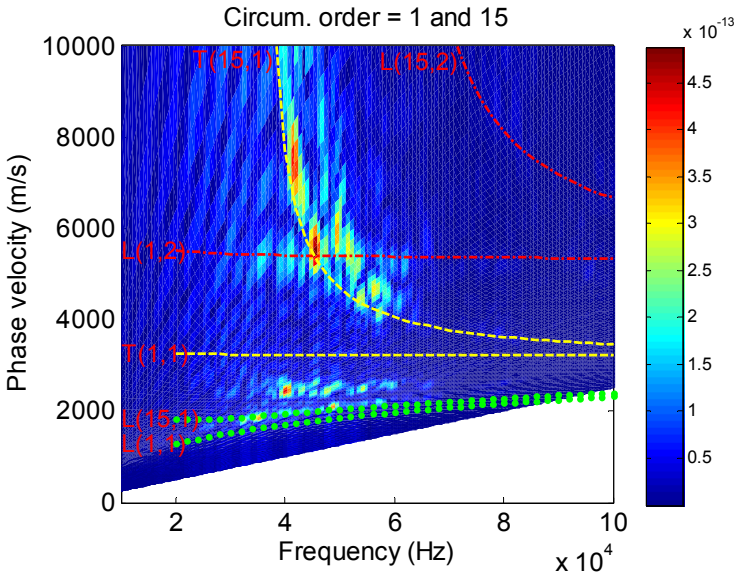

Figure A-6: Decomposed wave modes and the theoretical dispersion curves for circumferential orders 1 and 15.

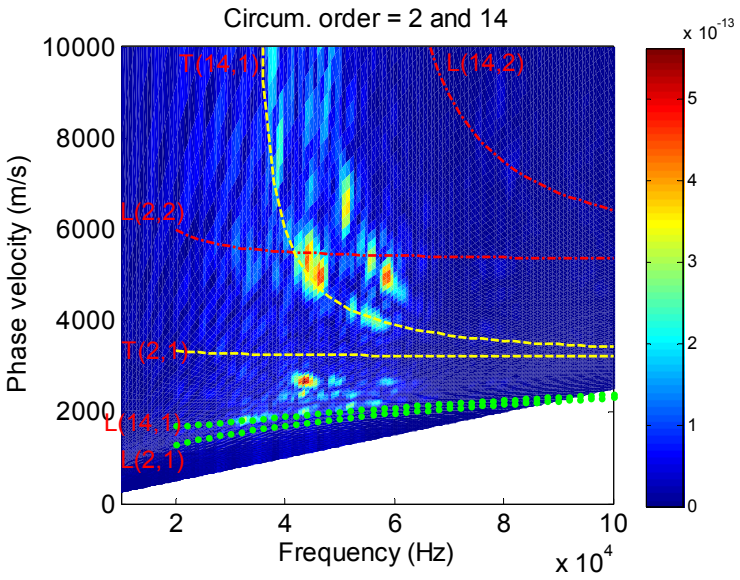

Figure A-7: Decomposed wave modes and the theoretical dispersion curves for circumferential orders 2 and 14.

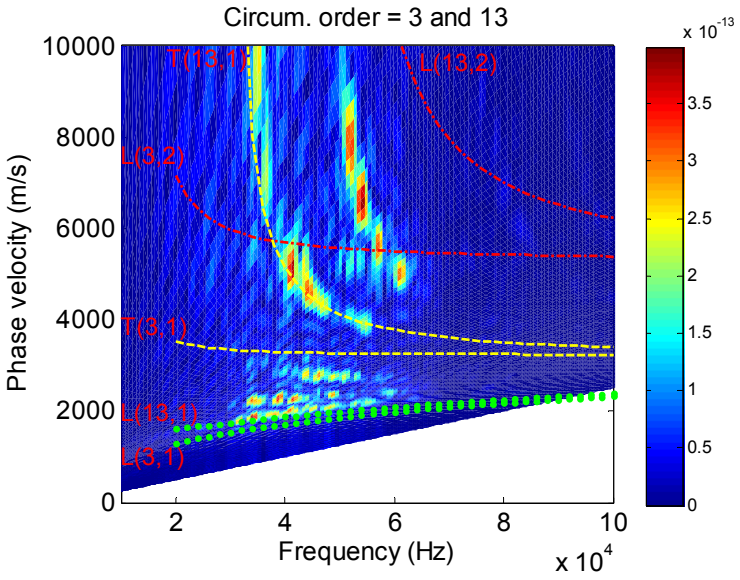

Figure A-8: Decomposed wave modes and the theoretical dispersion curves for circumferential orders 3 and 13.

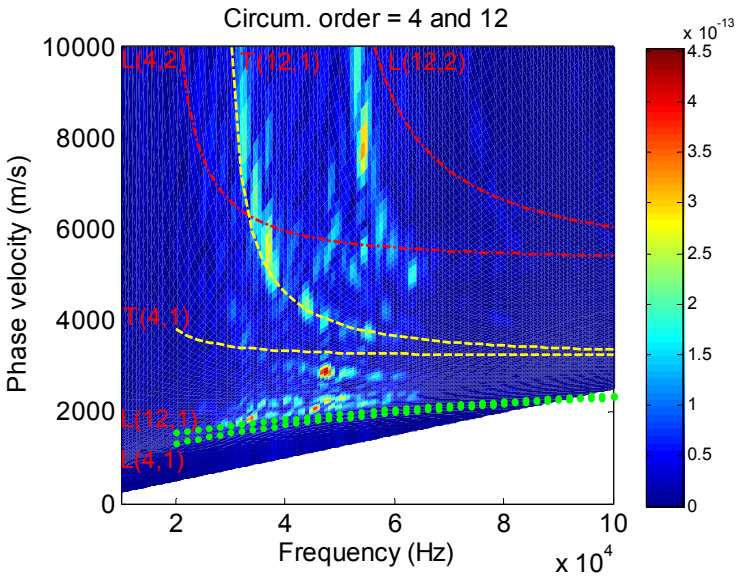

Figure A-9: Decomposed wave modes and the theoretical dispersion curves for circumferential orders 4 and 12.

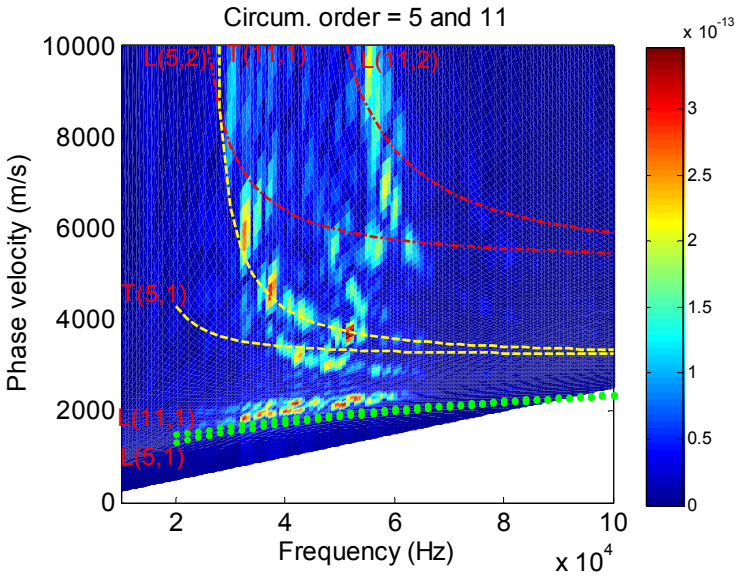

Figure A-10: Decomposed wave modes and the theoretical dispersion curves for circumferential orders 5 and 11.

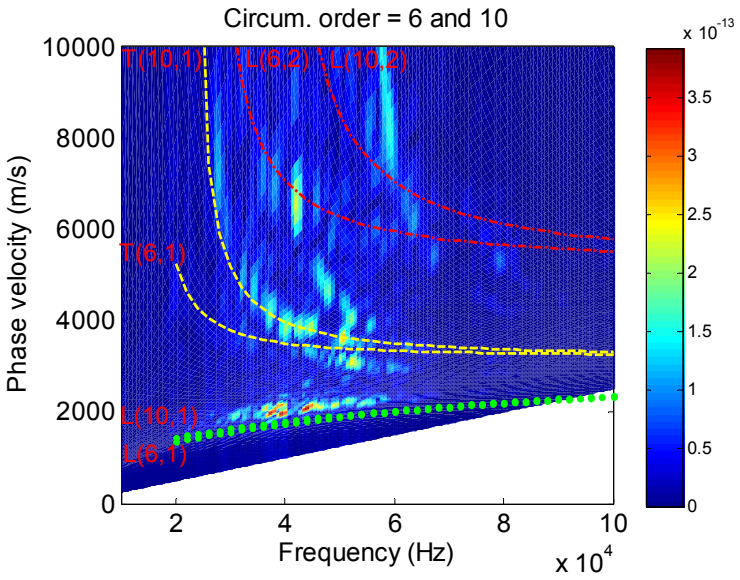

Figure A-11: Decomposed wave modes and the theoretical dispersion curves for circumferential orders 6 and 10.

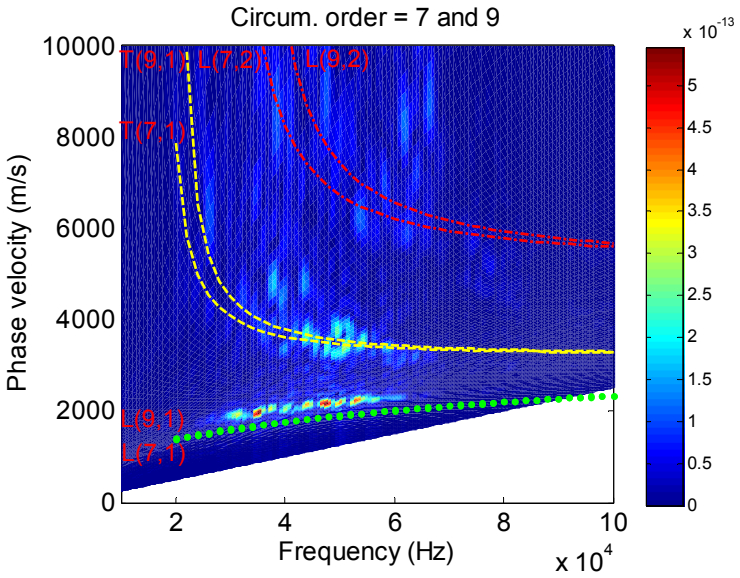

Figure A-12: Decomposed wave modes and the theoretical dispersion curves for circumferential orders 7 and 9.

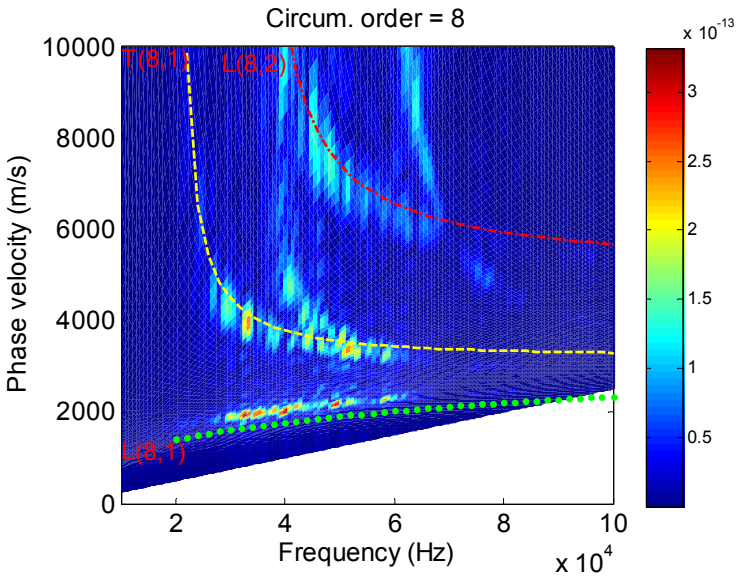

Figure A-13: Decomposed wave modes and the theoretical dispersion curves for circumferential orders 8.

A.4 Summary and future work

The scattered wave field from a defect is now fully decomposed into guided wave normal modes by a 3-D Fourier transform. The phase velocities of the scattered wave modes and their corresponding amplitudes are obtained. The NMD results agree quite well with the phase velocity dispersion curves calculated theoretically. The patterns of the NMD results are highly related to defect shape and size. Future work on defect sizing can utilize the NMD method on the scattered wave fields of defects with different lengths, depths, and shapes in FE modeling. These NMD results with known defect sizes

and shapes can be used to train a pattern recognition program. The pattern recognition program should be validated by experiments.

Considering the fact that receiving from a large number of locations, as used in our FE model, may be very costly and difficult to apply in practice, a short time Fourier transform (STFT) or wavelet transform may be used to substitute the Fourier transform in the axial direction of the pipe. In this way, only one ring of receivers is needed instead of the multiple rings for the Fourier transform. The group velocity dispersion curves will be obtained from the STFT instead of the phase velocity dispersion curves produced by the Fourier transform. Nevertheless, the group velocity dispersion curves can still be used to train the pattern recognition program in realizing defect sizing as well.

Appendix B

Nontechnical abstract

Pipes are widely distributed around us. They go across mountains, underneath highways and buildings for the transportation of gas, oil, etc. The pipelines age after long time services. Catastrophic failures can be caused by corrosion developed in aged pipelines. Regular monitoring of these pipelines is indispensable for ensuring the safety of our everyday life.

Ultrasonic waves can be used to inspect the integrity of pipelines. Wave propagation is a common phenomenon in nature. People may hear thunderstorms a few seconds after they see lightning, which is caused by the slower speed of sound in air compared to that of light. A spreading ripple is wave propagation in water. The difference of using ultrasonic waves to inspect pipes is that we are actively developing ways of sending ultrasonic waves in pipes and expecting waves bouncing back from defects.

Unlike air and water, pipes have boundaries. Only those ultrasonic waves that satisfy the pipe boundary conditions are able to propagate in pipes. They are called ultrasonic guided waves, a term used for ultrasonic waves traveling in bounded structures, such as pipes, rails, plates, etc. Guided waves have the ability of propagating very long distances because their energy is confined in the structure. This makes guided wave a suitable choice for nondestructive evaluation of pipelines.

The work in this thesis briefly introduces previous theories on guided wave propagation in elastic bare pipes and applies the theories to long range pipe imaging and

defect circumferential sizing. Taking into account the fact that many pipelines are covered with attenuative coatings for protection purposes, the thesis work mostly focuses on the full exploration of guided wave propagation characteristics in viscoelastic coated pipes. The guided wave modes that can propagate in a free viscoelastic coated pipe are solved by a special numerical method (semi-analytical finite element method), where finite element representation is used in the radial direction and analytical solutions are used in the circumferentially and axial directions of the coated pipe. The guided wave modes in coated pipes are proved to be orthogonal to each other, a nice mathematical condition simplifying studies of the many guided wave modes propagating in a structure. The guided wave field in a viscoelastic coate pipe created by a finite source loading (the geometrical loading position on the pipe) is obtained by expanding the wave field into the generated wave modes. With the complete understanding of the guided wave field generated by a source loading, guided waves are controlled and tuned to focus, where waves come together in phase to produce high energy, at any designed location in a viscoelastic coated pipe using a circumferentially distributed phase array. The focusing technique enhances guided wave penetration power, which is related to the distance a wave can travel, in coated pipe. Guided wave focusing effect in viscoelastic coated pipes and in elastic bare pipes are compared and discussed. Finite element modeling in ABAQUS, a commercially available computational program, is employed to visualize the focused energy enhancement in a viscoelastic coated pipe. Experiments are designed and conducted to verify the coated pipe focusing theories. Wave scattering from a defect is also analyzed by a new technique that decomposes the wave field into different guided wave modes. Future work on pipe inspection and defect sizing is discussed.

VITA

Jing Mu

EDUCATION

Ph.D., Engineering Science and Mechanics, August 2008
The Pennsylvania State University, University Park, PA, USA

M.S., Acoustics, Department of Electronic Science and Engineering, June 2004
Nanjing University, Nanjing, China

B.S., Acoustics, Department of Electronic Science and Engineering, June 2001
Nanjing University, Nanjing, China

AWARDS

- ESM Today Poster Competition, the Penn State University , **Second price,** 2006.
- Student paper competition in ASME Pressure Vessels & Piping Division Conference at Vancouver, Canada, **Second prize**, 2006

RECENT PUBLICATIONS

1. **Jing Mu** and J. L. Rose, "Guided wave propagation and mode differentiation in hollow cylinders with viscoelastic coatings," J. Acoust. Soc. Am., to appear.
2. **Jing Mu** and J. L. Rose, "Long range pipe imaging with a guided wave focal scan," Materials Evaluation, vol. 66(6), pp. 663-666, 2008.
3. **Jing Mu**, L. Zhang, and J. L. Rose, "Defect circumferential sizing by using long range ultrasonic guided wave focusing techniques in pipe," Nondestructive Testing and Evaluation, Volume 22, Issue 4, 2007, pages 239 - 253.
4. **Jing Mu** and J. L. Rose, "Guided wave normal modes in hollow cylinders with viscoelastic coatings," Review of Progress in Quantitative Nondestructive Evaluation, ed. by D.O. Thompson and D.E. Chimenti, vol. 27, 2007, pp. 86-91.
5. **Jing Mu** and Joseph L. Rose, "Long Range Ultrasonic Guided Wave Focusing in Pipe using a Phased-Array System," Review of Progress in Quantitative Nondestructive Evaluation, ed. by D.O. Thompson and D.E. Chimenti, vol. 26, p158, 2006.
6. **Jing Mu**, Li Zhang, Joseph L. Rose, Jack Spanner, "Long Range Ultrasonic Guided Wave Focusing in Pipe for Small Defect Detection, Location and Circumferential Length Analysis," Proceedings of PVP2006-ICPVT-11, ASME Pressure Vessels and Piping Division Conference, July 23-27, 2006, Vancouver, BC, Canada, pp. 399-404.
7. J. L. Rose, **J. Mu**, J.K. Van Velsor, "New Directions in Guided Wave Pipe Testing", Material Evaluation, 2007, vol.65(4), pp.375-378.
8. J. L. Rose, **Jing Mu**, Li Zhang, Cliff J. Lissenden, "Long Range Focused Ultrasonic Guided Waves for Corrosion Detection in Tubular Structures," Corrosion, 2006, paper06263.